

Diss.-No. ETH 27614

Farrokh Tarpoudi Baheri

On the Behaviour of Bituminous Surfaces at Subzero Temperatures: Condensation-Frosting and Icing

2021

Diss.-No. ETH 27614

ON THE BEHAVIOUR OF BITUMINOUS SURFACES AT SUBZERO
TEMPERATURES: CONDENSATION-FROSTING AND ICING

A thesis submitted to attain the degree of Doctor of Sciences of ETH Zurich
(Dr. Sc. ETH Zurich)

by

Farrokh Tarpoudi Baheri

M.Sc. in Mechanical Engineering, University of Tehran, Iran

Born on 11th May 1992

Citizen of Iran

Accepted on the recommendation of:

Prof. Dr. Dimos Poulidakos, ETH Zurich

Dr. Lily D. Poulidakos, Empa

Prof. Dr. Thomas M. Schutzius, ETH Zurich

Prof. Dr. Nicole Kringos, KTH Royal Institute of Technology

2021

This thesis is dedicated to my family.

عالم این خاک و هوا کو هر کفر است و فنا
در دل کفر آمده ام تا که به ایمان برسم

مولانا

غزل ۱۴۰۰، دیوان شمس تبریزی

This world of soil and air is the essence of disbelief and annihilation
I have entered the heart of disbelief in order to reach faith

Verse 1400

Divan-e Shams-e Tabrizi by Rumi

ABSTRACT

One of the most widely used construction materials worldwide is bitumen. It is used both directly and as a part of composite materials with other compounds in different applications ranging from road construction, paving, and roofing to sealing and gluing. One of the most common composite materials containing bitumen is asphalt concrete. Bitumen serves as a binder material of asphalt concrete and has to withstand mechanical and thermal loads due to harsh environmental conditions under heavy traffic loads and temperature cycles during its service life, which can last up to 20 years or even more. Hence, the development of durable asphalt materials is an essential part of sustainability in the road and in general, the construction sectors.

Bituminous surfaces develop temperature-dependent microstructures having domains with different mechanical, chemical, and selective wetting properties. Despite the importance of good bitumen performance in environments at subzero temperatures, the behavior of bitumen surface composition at cold temperatures and its interaction with water and ice has not been thoroughly investigated. This dissertation performs a fundamental study of bituminous materials at subzero temperatures, corresponding to typical winter and cold region environments conducive to icy roads. With the aid of advanced atomic force microscopy combined with infrared spectroscopy (AFM-IR) in an environmental chamber, we demonstrated the chemistry and mechanical properties of bitumen surface with nanoscale precision for a broad temperature range. Cooling bitumen to subzero temperatures can have several interesting effects on its surface texture and composition, especially on its three surface domains, catana, peri, and para. The findings of this work show that the para domain coarsens with cooling. An

interfacial transition domain is formed between the para and peri domains. It was also shown that the three main surface domains have different wettability with higher selective condensation on the para domain.

Condensation and freezing of atmospheric water on bituminous surfaces, commonly occurring in a broad range of construction and road surfaces, and freezing of atmospheric water on bituminous construction and road surfaces is a recurring event. However, droplet freezing on bitumen and passive inhibition methods are poorly understood. In the second part of this work, we investigate relative humidity and substrate cooling effects on condensation freezing on subzero temperature bituminous surfaces and find that droplet freezing is explosive with rapid local heating. We explain the related physics and find that relative humidity and cooling rate can affect droplet sizes and freezing temperatures. We then rationally embed phase change material (PCM) microcapsules in bitumen, harnessing their latent heat to significantly delay freezing, demonstrating a viable option for frost mitigation.

Driven by recently developed superhydrophobicity and icephobicity knowledge, we attempted to advance fundamental knowledge of road deicing beyond the traditional periodic application of using salt and mechanical ice removal. The ice adhesion phenomenon mainly has been studied intensively with respect to its manifestation on rigid, homogeneous surfaces, with soft materials being the topic of few recent investigations. Icing and ice adhesion can also often occur on largely heterogeneous surfaces regarding their chemical composition and, in particular, the resulting mechanical behavior. However, ice adhesion on heterogeneous substrates (for example, the widely used asphalt concrete, which consists of rigid aggregates embedded in soft bitumen) is hardly understood. In the third part of this work, we investigate ice adhesion on such heterogeneous materials,

juxtaposing the behavior of their two main constituents, the rigid glass-ceramic aggregates modeled by Macor® and bitumen, to the behavior of a bitumen-Macor® composite, with respect to applied normal tension, shear, and composite stresses. The results show that the ice adhesion shear stress on Macor® is almost twice as large as that on bitumen with a brittle failure mode, whereas the normal components of these ice adhesion stresses are in a similar range. Coating of the most ice-adhesive component (Macor®) with a thin superhydrophobic coating shows lower ice adhesion stress on the heterogeneous surface. We also find a strong dependence of the ice adhesion stress on the order of appearance of the two surface materials in composite surfaces. If the rigid material is placed before the bitumen section in the direction of applied force, a lower shear ice adhesion stress is observed.

The fundamental findings of this work improve our understanding of the behavior of bitumen in subzero environments, the freezing delay through PCM additives, and the ice adhesion reduction through aggregate coatings, aiding us in our quest towards attaining better sealant and road performance. However, for the practical application of these solutions, further dedicated research is needed.

ZUSAMMENFASSUNG

Eines der weltweit am häufigsten verwendeten Baumaterialien ist Bitumen. Es wird sowohl direkt als auch als Teil von Verbundwerkstoffen in Verbindung mit anderen Materialien und für verschiedene Anwendungen verwendet, die vom Straßenbau über Pflasterung und Überdachung bis hin zur Abdichtung und Verklebung reichen. Einer der häufigsten bitumenhaltigen Verbundwerkstoffe ist Asphaltbeton. Bitumen dient als Bindemittel für Asphaltbeton und muss während seiner Lebensdauer, die bis zu 20 Jahre oder sogar länger dauern kann, mechanischen und thermischen Belastungen aufgrund rauer Umgebungsbedingungen unter starken Verkehrsbelastungen und Temperaturzyklen standhalten. Daher ist die Entwicklung langlebiger Asphaltmaterialien ein wesentlicher Bestandteil der Nachhaltigkeit im Strassensektor als auch generell im Baugewerbe.

Bitumenoberflächen entwickeln temperaturabhängige Mikrostrukturen mit Domänen mit unterschiedlichen mechanischen, chemischen und selektiven Benetzungseigenschaften. Trotz der Bedeutung einer guten Bitumenleistung in Umgebungen bei Temperaturen unter Null wurde das Verhalten der Bitumenoberflächenzusammensetzung bei kalten Temperaturen und ihre Wechselwirkung mit Wasser und Eis nicht gründlich untersucht. Diese Dissertation führt eine grundlegende Untersuchung von bituminösen Materialien bei Temperaturen unter Null durch, die typischen Umgebungen im Winter und in kalten Regionen entsprechen, und zu vereisten Straßen führen können. Mit Hilfe von fortschrittlicher Rasterkraftmikroskopie und in Kombination mit Infrarotspektroskopie (AFM-IR) in einer Umgebungskammer konnten wir die chemischen und mechanischen Eigenschaften der Bitumenoberfläche mit

Nanometer Präzision für einen breiten Temperaturbereich demonstrieren. Das Abkühlen von Bitumen auf Temperaturen unter Null kann verschiedene interessante Auswirkungen auf seine Oberflächentextur und -zusammensetzung haben, insbesondere auf seine drei Oberflächendomänen Catana, Peri und Para. Die Ergebnisse dieser Arbeit zeigen, dass die Para-Domäne durch das Abkühlen vergrößert wird. Eine Grenzflächenübergangsdomäne wird zwischen den Para- und Peri-Domänen gebildet. Es wurde auch gezeigt, dass die drei Hauptoberflächendomänen eine unterschiedliche Benetzbarkeit mit höherer selektiver Kondensation auf der Para-Domäne aufweisen.

Das Kondensieren und Einfrieren von atmosphärischem Wasser auf bituminösen Oberflächen, das üblicherweise in einem breiten Spektrum von Bau- und Straßenoberflächen auftritt, und das Einfrieren von atmosphärischem Wasser auf bituminösen Bau- und Straßenoberflächen ist ein wiederkehrendes Ereignis. Das Einfrieren von Tröpfchen auf Bitumen und passive Inhibitionsmethoden sind jedoch kaum bekannt. Im zweiten Teil dieser Arbeit untersuchen wir die Auswirkungen der relativen Luftfeuchtigkeit und der Substratkühlung auf das Einfrieren von Kondenswasser auf bituminösen Oberflächen mit Temperaturen unter Null und stellen fest, dass das Einfrieren von Tröpfchen unter schneller lokaler und explosiver Erwärmung stattfindet. Wir erklären die damit verbundene Physik und stellen fest, dass die relative Luftfeuchtigkeit und Abkühlrate die Tröpfchengröße und die Gefriertemperaturen beeinflussen können. Anschließend binden wir PCM-Mikrokapseln (Phase Change Material) rational in Bitumen ein und nutzen deren latente Wärme, um das Einfrieren erheblich zu verzögern. Dies zeigt eine praktikable Option zur Frostminderung.

Basierend auf diesem entwickelten Wissen über Superhydrophobie und Eisphebie haben wir versucht, das grundlegende Wissen über das Enteisen von Straßen über die traditionelle periodische Anwendung der Verwendung von Salz und mechanischer Eisentfernung hinaus zu erweitern. Das Phänomen der Eisadhäsion wurde hauptsächlich im Hinblick auf sein Erscheinen auf starren, homogenen Oberflächen intensiv untersucht, wobei weiche Materialien Gegenstand weniger neuerer Untersuchungen sind. Vereisung und Eishaftung können auch häufig auf weitgehend heterogenen Oberflächen hinsichtlich ihrer chemischen Zusammensetzung und insbesondere des daraus resultierenden mechanischen Verhaltens auftreten. Die Eishaftung auf heterogenen Substraten (z. B. dem weit verbreiteten Asphaltbeton, der aus in weiches Bitumen eingebetteten starren Zuschlagstoffen besteht) ist jedoch kaum verstanden. Im dritten Teil dieser Arbeit untersuchen wir die Eisadhäsion an solchen heterogenen Materialien, indem wir das Verhalten ihrer beiden Hauptbestandteile, der von Macor® und Bitumen modellierten starren Glaskeramikaggregate, dem Verhalten eines Bitumen-Macor®-Verbundwerkstoffs in Bezug auf angelegte Normalspannungs-, Scher- und Verbundspannungen gegenüberstellen. Die Ergebnisse zeigen, dass die Scherspannung der Eisadhäsion auf Macor® fast doppelt so groß ist wie die auf Bitumen mit einem Sprödbbruchmodus, während die normalen Komponenten dieser Eisadhäsionsspannungen in einem ähnlichen Bereich liegen. Die Beschichtung der eisklebendsten Komponente (Macor®) mit einer dünnen superhydrophoben Beschichtung zeigt eine geringere Eisadhäsionsspannung auf der heterogenen Oberfläche. Wir finden auch eine starke Abhängigkeit der Eisadhäsionsspannung von der Reihenfolge des Auftretens der beiden Oberflächenmaterialien in Verbundoberflächen. Wenn das starre Material in

Richtung der ausgeübten Kraft vor dem Bitumenabschnitt platziert wird, wird eine geringere Schereisadhäsionsspannung beobachtet.

Die grundlegenden Ergebnisse dieser Arbeit verbessern unser Verständnis des Verhaltens von Bitumen in Umgebungen unter Null, der Gefrierverzögerung durch PCM-Additive und der Verringerung der Eishaftung durch Aggregatbeschichtungen und unterstützen uns bei unserem Streben nach einer besseren Dichtungs- und Straßeneigenschaften. Für die praktische Anwendung dieser Lösungen sind jedoch weitere Forschungsarbeiten erforderlich.

ACKNOWLEDGMENT

This journey would not have been possible without the support of my family, professors, mentors, and friends. I would like to express my deepest gratitude to Prof. Dr. Dimos Poulikakos for granting me the opportunity to perform my doctoral research in his Laboratory of Thermodynamics in Emerging Technologies (LTNT) ETH Zurich and do research on different interesting phenomena over the past four fantastic years. Beyond his undisputed scientific and academic expertise, his openness for discussion, vision, and leadership had many lessons for my life.

Next, I highly appreciate the persistent and continuous scientific, practical, and financial support of Dr. Lily D. Poulikakos from the concrete and asphalt lab at Empa. Our regular meetings and discussions were key to organize my work and ideas successfully. In addition, she provided opportunities for me to collaborate with colleagues on different projects at Empa which, I practiced teamwork soft skills. These academic research collaborations eventually lead to several additional publications.

My special thanks go to Prof. Dr. Thomas M. Schutzius. His motivation, challenging questions, and well thought advice, with demanding but reasonable requests, helped me progress in my career and develop rational and critical thinking skills required for high-quality research.

Furthermore, I would like to thank Prof. Dr. Nicole Kringos from KTH Royal Institute of Technology, who, as my external co-examiners, had the patience to read and critically examine my thesis.

I would like to thank the B.Sc. and M.Sc. students that I worked with during my doctoral studies. Thanks to Miguel Rico Luengo, Jasmin Stoff, and Pavel Malach. All of you did a great job, and it was much fun to work with you.

It would also not be fair not to thank all my colleagues, members of the LTNT group at ETH, and former Abt. 301 members at Empa, but I have to only highlight few names due to the page limit concerns. I would like to thank technicians and my colleagues at ETH: Jovo Vidic, Peter Feusi, Efstratios Mitridis, Kartik Regulagadda, Julia Gerber, Christopher Walker, and my colleagues from Empa: Maria Chiara Cavalli, Muhammad Rafiq Khan Kakar, Hans Kienast, Ronald Takacs, Christian Meierhofer, Robin Pauer and Beatrice Fischer. Technical support from Bruker, specifically from Anirban Roy, Igor Arkov, and Miriam Unger, is gratefully acknowledged.

In closing to my family, thank you for supporting and encouraging me in every step of my life and inspiring me to pursue my dreams. All of this would have been just a dream without the continuous emotional and the initial financial supports that I received from my parents during my education. I am especially grateful to my mother, who provided me with unwavering emotional support throughout this journey; without her, I would have never been able to make it this far.

Zurich, May 2021

Farrokh Tarpoudi Baheri

TABLE OF CONTENT

ABSTRACT	i
ZUSAMMENFASSUNG	iv
ACKNOWLEDGMENT	viii
TABLE OF CONTENT	x
LIST OF FIGURES.....	xiv
1 INTRODUCTION	1
2 FUNDAMENTALS.....	4
2.1 Bituminous mixtures	4
2.2 Aggregates	4
2.2.1 Macor®.....	5
2.3 Bitumen	5
2.3.1 Bitumen Fractions (SARA).....	6
2.3.2 Bitumen Molecular structure	6
2.3.3 Thermal Properties of Bitumen	7
2.3.4 Rheology of Bitumen	7
2.4 Bitumen Surface Microstructure.....	8
2.5 Surface Energy and Wettability.....	9
2.6 Water Phase Change Phenomena.....	12
2.6.1 Water Phase Diagram	12
2.6.2 Classical nucleation theory	13
2.6.3 Condensation.....	16
2.6.4 Freezing	17
2.6.5 Frosting.....	17
2.7 Ice and Substrate Interaction.....	18

2.7.1	Consequences of icing and its prevention	18
3	BITUMEN SURFACE MICROSTRUCTURE EVOLUTION IN SUBZERO ENVIRONMENTS	20
3.1	Abstract	21
3.2	Introduction.....	22
3.3	Materials and Methods	26
3.3.1	Materials.....	26
3.3.2	Bulk chemistry characterization.....	27
3.3.3	AFM-IR Characterization	27
3.3.4	Image analysis: area fraction calculation.....	32
3.3.5	IR spectra analysis.....	36
3.4	Results and discussion	36
3.5	Conclusion	50
3.6	Acknowledgments	52
4	DROPWISE CONDENSATION FREEZING AND FROSTING ON BITUMINOUS SURFACES AT SUBZERO TEMPERATURES.....	53
4.1	Abstract	54
4.2	Introduction.....	54
4.3	Materials and methods.....	56
4.3.1	Materials.....	56
4.3.2	Solution preparation and coating.....	58
4.3.3	Experimental setup: Constant cooling rate.....	60
4.3.4	Experiment setup: Constant cooling flux	62
4.3.5	Differential scanning calorimetry (DSC).....	63
4.4	Results and discussion	64
4.5	Conclusion	76

4.6	Acknowledgments	77
5	ICE ADHESION BEHAVIOR OF HETEROGENEOUS BITUMINOUS SURFACES	78
5.1	Abstract	79
5.2	Introduction.....	80
5.3	Methods and Material Studied	83
5.3.1	Materials.....	83
5.3.2	Substrates and coatings.....	Error! Bookmark not defined.
5.3.3	Characterization	88
5.4	Results and Analysis.....	90
5.5	Discussion and conclusions.....	99
5.6	Acknowledgments	100
6	CONCLUSIONS & OUTLOOK.....	101
6.1	Conclusions.....	101
6.2	Outlook	102
	Appendix A.....	104
	Specimen properties	104
	AFM-IR and experimental setup	104
	Cantilever resonance properties.....	108
	Post-processed and original AFM images at various temperature steps	109
	DSC analysis	116
	Chemistry analysis by IR methods	117
	Appendix B.....	121
	The radius of curvature of bitumen surface domains.....	122
	Wettability of bitumen surface domains.....	124

Appendix C	127
PCM microcapsule resistance examination.....	127
Bitumen sample preparation and examination.....	128
Experimental setups	129
DSC analysis	130
DSC baseline calibration	130
DSC analysis of materials	131
Water condensation freezing.....	133
Cascade freezing of supercooled droplets.....	133
Cooling rate effect on condensation freezing	133
Supporting Videos	135
Appendix D.....	136
7 BIBLIOGRAPHY	143
LIST OF PUBLICATIONS.....	175
CURRICULUM VITAE.....	Error! Bookmark not defined.

LIST OF FIGURES

- Figure 2.1 Liquid droplet on a solid surface in equilibrium condition.** Arrows indicate surface tensions for each interface.10
- Figure 2.2 Sliding droplet down on a tilted solid substrate.** Apparent contact angle in the front and receding contact angle in the rear.11
- Figure 2.3 Wetting status on surface roughness.** a) Cassie-Baxter state, b) Wenzel state.11
- Figure 2.4 Conventional pressure versus temperature of the water phase diagram.** The triple contact point (TP), where three water phases meet and the critical point (CP) in thermodynamics, is the liquid-vapor phase's endpoint (adapted from ⁶⁹).....13
- Figure 2.5 The difference in Gibbs free energy, as a function of ice embryo radius and liquid water temperature.** a) Balance between driving volumetric G_{volume} with opposing $G_{surface}$ Gibbs free energies, b) Gibbs free energy associated with nucleation at three different temperatures.....15
- Figure 3.1 Principles and findings of the AFM-IR technique.** a) Artificially colored phase image at $T_1 = -20$ °C of a stepwise cooling sequence defined later. The highlighted regions with yellow stripes are the catana domains, and their surrounding area is the peri domain, false-colored green is the transition domain, blue is the para domain, and red denotes the sal sub-domain islands. White scale bar: 1 μm . b) Schematic of bitumen sample on a glass substrate in the enclosed humidity and temperate chamber. We used copper and aluminum disks (each 1 mm thickness) to elevate the sample. Color dots show the location of three thermocouples, red dot: stage

temperature thermocouple (T1), green dot: thermocouple for surface temperature (T2), blue dot: thermocouple as environmental temperature sensor (T3). c) Drawing shows tapping cantilever following the surface profile to create the tapping AFM topography scan in first mechanical resonance mode (T1=25 °C). d) AFM phase image (phase map) detects surface properties such as mechanical compliance. Softer substrate shifts oscillating cantilever phase and causes phase lag, which corresponds to the darker phase contrast in the AFM phase scan (T1=25 °C). e) Schematic drawing of an AFM-IR scan. The pulse IR laser shifts the cantilever to its second mechanical resonance by thermal expansion of the excited substrate with the IR laser at a favorable wavenumber. Example of IR map at the same location scanned at 1456 cm⁻¹ wavenumber (T1=25 °C).....28

Figure 3.2 Effect of cold temperatures on the surface properties of bitumen.

AFM tapping surface topography scans on bitumen at temperature steps of a) T1=25°C, and b) T1=-20°C during the stepwise cooling sequence, and their magnified areas are shown in (c) and (d), respectively. (e)-(f) Corresponding AFM phase images of the same locations as in (a) and (b), respectively. g) The enlarged area of e showing three domains: catana, peri, and para. h) Magnified view of (f), showing five domains at low-temperature in addition to the other three domains in (g).....35

Figure 3.3 Effect of temperature on surface roughness in specific domains.

AFM topography images at steps, a) T1=25 °C, and b) T1=-20 °C of the stepwise cooling sequence. c) Lines indicate topographies of bitumen at T1=25 °C (red) and T1=-20 °C (blue) in approximately the same location. The green asterisk is the zero point of the line profile (Distance = 0 μm). Marked points by circles are the valleys of the catana structures in the

vicinity through which the line passes, to show that microstructures shift their position relative to each other as a consequence of the cooling.39

Figure 3.4 Effect of temperature on bitumen surface domains. Example of AFM phase image at the same location, during the stepwise cooling cycle. a) $T_1=25\text{ }^\circ\text{C}$, b) $T_1=-35\text{ }^\circ\text{C}$, and c) $T_1=25\text{ }^\circ\text{C}$ (reheated to the initial condition). d) Area fractions of the sal sub-domain (red), para domain (blue), and transition domain (green) vs. time at different stepwise cooling temperatures of the stage temperature T_1 (---) and surface temperature T_2 (—), read temperatures from the right Y axis in panel (d). Symbols ■, ▲, and ● each show an independent AFM scan sequence on a fresh sample at the same location in dry conditions, showing qualitatively similar behavior.41

Figure 3.5 Effect of the slow cooling rate on the faded boundaries of the bitumen surface microstructure and determination of the chemistry of the transition domain. AFM-IR (a) topography, (b) phase, and (c) IR spectroscopy images for wavenumber 1456 cm^{-1} at $T_1=25\text{ }^\circ\text{C}$. (d) topography, (e) phase, and (f) IR spectroscopy images for wavenumber 1456 cm^{-1} of bitumen at $T_1=-20\text{ }^\circ\text{C}$ (directly cooled from $T_1=25\text{ }^\circ\text{C}$ to $T_1=-20\text{ }^\circ\text{C}$ at a slow constant cooling rate of $\sim -1.5\text{ }^\circ\text{C}/\text{min}$). (g) AFM-IR spectra smoothed by Savitzky-Golay function using a polynomial order of five fittings on six neighboring points. Spectra of bitumen at $T_1=25\text{ }^\circ\text{C}$ (para: orange line, peri: red line; see (b) for locations) and $T_1=-20\text{ }^\circ\text{C}$ (para: cyan line, peri: blue line, transition domain: green line; see (e) for locations) and the original bulk FTIR spectra at $23\text{ }^\circ\text{C}$, black line. The straight vertical line shows the location of 1456 cm^{-1} wavenumber.43

Figure 3.6 IR indexes of FTIR spectra and AFM-IR local IR spectra of the bitumen surface domains show the concentration distribution of the chemical functional groups in bulk and nanoscale, respectively, as a function of temperature. Functional groups are present around wavenumbers corresponding IR peak values, sulfoxide: 1030 cm^{-1} , aliphatic: 1376 cm^{-1} & 1456 cm^{-1} , aromatic: 1600 cm^{-1} and carbonyl: 1700 cm^{-1} . Each column bar shows average value with min and max values for at least three experiments. In cases of peri $25\text{ }^{\circ}\text{C}$, and para $-20\text{ }^{\circ}\text{C}$, the bar represents 4 and 5 data points, respectively. FTIR column bar is an average of 32 measurements with a negligible error.....47

Figure 3.7 Coarsening of the para domain and plentiful appearance of the sal sub-domain with a narrow transition domain from very high cooling rates. AFM-IR results showing (a) topography, (b) Phase map (AFM phase), (c) Magnified phase map view of the marked area by the white square (see b), and (d) IR spectroscopy images for wavenumber 1456 cm^{-1} of bitumen at $T_1=25\text{ }^{\circ}\text{C}$. AFM-IR (e) topography, (f) phase map (AFM phase), (g) Magnified phase map view of the marked area by white square (see f) and (h) IR spectroscopy images for wavenumber 1456 cm^{-1} of bitumen at $T_1=-20\text{ }^{\circ}\text{C}$ (directly cooled from $T_1=25\text{ }^{\circ}\text{C}$ to $T_1=-20\text{ }^{\circ}\text{C}$ at an extreme cooling rate of $\sim -90\text{ }^{\circ}\text{C}/\text{min}$). Densely emerged sal sub-domain (see g) with limited transition domain, because of the fast cooling rate....49

Figure 4.1 Experimental setup for constant cooling rate. a) Condensation freezing setup. Schematic of the inlet nitrogen gas supply system in the dashed line box (not to scale). The location of the thermocouple in the copper stage, T_1 , and the cryogenic stage feedback cryogenic stage, T_2 , temperature sensors are shown as green and red dots, respectively. The

environmental sensor records chamber environment temperature T_{env} and relative humidity percentage RH . The location of the optical microscope objective or IR camera lens is shown as “objective”. b) Copper pin under the optical microscope at 5X magnification (without sample) and c) the same copper pin shown as seen from the IR camera (without sample)....61

Figure 4.2 Condensation freezing on the bitumen surface. a) optical image of the supercooled water droplets during freezing. The droplet in the white dotted circle is an example of a freezing water droplet. b) Infrared image of a freezing droplet. Due to the released latent heat of fusion at the moment of freezing, the temperature of a supercooled droplet jumps to the equilibrium water freezing temperature of 0 °C.....65

Figure 4.3 Condensation and freezing on the surface of virgin bitumen under different environmental relative humidity (RH) conditions. Five temperature steps of 5 °C , -10 °C , -25 °C , -35 °C , -50 °C (synchronized time steps) at -10 °C/min constant cooling rate under three different environmental RH conditions ($T_{env} = 21.5 \pm 0.5$ °C) are shown. a) $RH = 20\%$ b) $RH = 50\%$ c) $RH = 80\%$. Dotted regions at -35 °C panels show the extent of the frozen areas with different degrees of surface frosting: **a**, initiation ($RH 20\%$), **b**, partially frozen ($RH 50\%$), **c**, mostly frozen ($RH 80\%$).....66

Figure 4.4 Condensation and freezing on the surface of virgin bitumen under different conditions. Initial condensation temperature a) under three RH conditions of 20%, 50%, and 80% at -10 °C/min cooling rate. b) at three cooling rates -1 °C/min, -10 °C/min, and -20 °C/min at $RH = 50\%$. Initial freezing temperature c) a) under three RH conditions of 20%, 50%, and 80% at -10 °C/min cooling rate. d) at three cooling rates -1 °C/min, -10

°C/min, and -20 °C/min at $RH = 50\%$. (For all cases, $T_{env} = 21.5 \pm 0.5$ °C).

.....68

Figure 4.5 Microscopic ice bridging and freezing propagation on bitumen.

a) Three supercooled liquid droplets. b) Freezing of the large droplet forms condensation deposits. c) An ice bridge grows while the condensation deposit and the smallest liquid droplet evaporate. d) The ice bridge reaches the medium size drop and freezes it..... 69

Figure 4.6 Thermal imaging of recalescence and cascade freezing. a)

Condensed supercooled water droplets on bitumen. The white dotted line shows the location of the cooling pin below the bituminous layer. b) Rapid release of latent heat of fusion during supercooled droplet freezing causes the droplet temperature to increase to the equilibrium value. c-d) Ice bridging or freezing of the condensate deposit, as discussed in Figure 4.5, results in neighboring droplet freezing and “cascade freezing”. Arrows show the direction of a cascading freezing event.71

Figure 4.7 DSC analysis of the virgin and modified bitumen when in contact with a 1 μ l water droplet (positive heat flow indicates an endothermic process). a) Virgin bitumen at 10 °C/min rate, b) virgin bitumen at 20

°C/min rate, c) 25 wt.% PCM modified bitumen at 10 °C/min rate, and d) 25 wt.% PCM modified bitumen at 20 °C/min rate. Each plot has three heating and cooling cycles..... 72

Figure 4.8 PCM can delay freezing on bitumen. Bitumen surfaces after 3

minutes cooling at the same constant cooling flux condition from 25 °C for two material states of a) Virgin. b) 25 wt.% PCM-modified bitumen. c) Freezing initiation time on a bitumen surface plotted for virgin and 25 wt.% PCM-modified bitumen in black and red colors, respectively. d) Bitumen

surface temperature measured by IR camera plotted for virgin and 25 wt.% PCM-modified bitumen in black and red colors, respectively. PCM activation occurs gradually as the cooling is done from the bottom of the bitumen. This manifests itself into a kink in the temperature profile of the surface temperature once the PCM effect reaches the surface. Initial freezing nucleation temperatures are marked with blue circle symbols. ...74

Figure 5.1 Ice adhesion on road-like materials at subzero temperatures. a) General schematic of ice formation on heterogeneous road-like surfaces. b) Complex modulus of bitumen at 20 °C and -10 °C at 0.1 Hz versus reported complex modulus of Macor® material at 25 °C ¹⁸². c) Receding contact angle of a water droplet on bitumen surface and Macor® at two sample temperatures of 25 °C and -10 °C and environmental condition of $RH < 1\%$ at 24 ± 1 °C.85

Figure 5.2 Ice adhesion modes on heterogeneous bitumen. Schematic drawing of experimental modes to measure a) pure shear stress b) combined stress, and c) normal-tension stress. Examples of experimentally measured force curves vs. time for d) pure shear stress, e) combined stress, and f) normal-tension stress ice adhesion modes. Calculated stresses based on absolute peak force F^* defined in (d) (e) or (f) are plotted in the box plot (left) and data points (right) for three modes of g) pure shear (τ_{shear}^*), h) combined stresses (σ_{CS}^* and τ_{CS}^*), and i) normal-tension (σ_{normal}^*) plotted for the absolute tensile force value. Each data point represents an experiment of ice adhesion stress measurement.92

Figure 5.3 Impact of substrate heterogeneity and anisotropy on ice adhesion.

Results are shown for four bitumen-ice area fractions of $\phi = 0\%$ (i.e., pure

Macor®), 35%, 67%, and 100%. Samples were installed in two selective stripe directions—defined as the direction along the long length of the stripe—namely, perpendicular and parallel to the applied force. Plots of τ_{shear}^* vs. ϕ for a) perpendicular and b) parallel applied force directions; results of probability associated with a Student's paired T-test, with a two-tailed distribution, are shown by red lines only for each pair of samples only when the difference between two groups is significant (i.e. $P < 0.05$). Plots of σ_{CS}^* and τ_{CS}^* vs. ϕ for c) perpendicular and d) parallel applied force directions. e) Plot of σ_{normal}^* vs. ϕ , and such measurements are neutral to the direction of the stripe with respect to the applied force direction; but samples were installed in similar perpendicular directions as panels (a) and (c).94

Figure 5.4 Reducing ice adhesion to Macor®. Micrographs of a) a pure Macor® surface and b) a Macor® substrate with a superhydrophobic coating (SHM). c) Receding contact angles of a water droplet on Macor® and SHM at two sample temperatures of 25 °C and -10 °C and environmental condition of $RH < 1\%$ at 24 ± 1 °C. Plots of ice adhesion stress on Macor and SHM: d) τ_{shear}^* , e), σ_{CS}^* and τ_{CS}^* , and f) σ_{normal}^* . Scale bars: (a)-(b) 1 mm.96

Figure 5.5 The role of material order on ice adhesion to heterogeneous bituminous surfaces. Ice adhesion on the boundary of compliant-rigid

materials and impact of the material order for ice adhesion mode of a) τ_{shear} * and b) σ_{CS} * and τ_{CS} *. The color code and abbreviations are black for bitumen (B), red for Macor® (M), and green for chemically coated superhydrophobic Macor® (SHM).98

1 INTRODUCTION

Bituminous roads are exposed to water and harsh cold environmental conditions. The icing on asphalt concrete (AC) can cause accidents and slowing down traffic. Alleviating ice formation on roads requires time, energy, and equipment to ensure safe driving and reduce the risk of winter accidents due to icing¹⁻³. The removal of snow and winter maintenance is an important hazard in Switzerland and considerable costs are associated with winter maintenance. One day of the national roads winter maintenance costs in average one million Swiss francs (MCHF)⁴. Yearly expenses add up to ca. 20 MCHF for light winter maintenance, whereas in the case of heavy maintenance of roads, costs can reach 50 MCHF or more⁴. To address this problem, deicing techniques are employed but mostly limited to the mechanical removal, chemical deicers, and salt usages (predominantly sodium chloride)⁵⁻⁷. Eventually, drained salt can be harmful to the environment and cause salty underground and surface water resources⁸⁻¹⁰. Moreover, salt and brine can interact with bituminous mixtures commonly manifested as either the loss of cohesive strength within the mastic or the loss of adhesion between the binder and the aggregate that is resulting in bitumen-aggregate stripping, pavement degradation, and shortens pavements' service life¹¹⁻¹³.

Current approaches have caused an overreliance on environmentally threatening and pavement damaging techniques. Thus, novel technologies, including microwave and conductive heating methods, are developed to remove ice¹⁴⁻¹⁷, but mostly are energy and time-consuming with limited performance. Early mentioned active deicing methods are demanding an on-site operation while

passive deicing modification can keep road surfaces ice-free without requiring real-time maintenance such as asphalt mixtures with embedded salt or modified with recycled crumb rubber^{18–22}. Moving toward sustainable and robust solutions for deicing bituminous surfaces, complementary advanced passive deicing or anti-icing approaches are needed. These desired modifications could rely on the use of rationally engineering of icephobic materials—especially those that can leverage renewable available energy resources such as solar—which can perform well even under harsh environmental conditions. Phase change materials (PCM) can perform as a heat reservoir over the period that extra energy is available and release the heat when is needed. This function is critical for asphalt mixtures and can protect bitumen against warm sunlight overheating and high-temperature rutting, while over cold nights, the stored heat can be released and postpone icing and cold temperature cracking of asphalt surfaces^{23–28}. In cases icing happens, the low ice adhesion stresses of the icephobic treated surface make it possible to remove ice over many freeze/thaw cycles^{29–32}.

In this thesis, the primary aim was set to perform fundamental research toward understanding the properties of bituminous surfaces at subzero temperatures and their interaction with water and ice. This manuscript first introduces the theoretical background, followed by three studies focused on the behavior of bituminous surfaces at subzero temperatures, bitumen in contact with water over condensation freezing phenomena, and ice adhesion measurement on bitumen and model aggregates. This work presents two modifications for each of the asphalt concrete components toward achieving intrinsic icephobic properties on bituminous surfaces. It is shown that embedded PCM microcapsules can delay condensation freezing on the bitumen surface. Indeed, surface treatment of the

model aggregates (as the most ice adhesive component of the asphalt composite) can reduce ice adhesion stresses to half. Outcomes of the thesis can pave a roadmap for future projects in designing intrinsic icephobic bituminous materials.

2 FUNDAMENTALS

This chapter summarizes the theoretical and experimental knowledge needed to understand the behavior of bitumen at cold temperatures. Sections 2.1 introduces different bitumen applications. Section 2.2 summarizes the properties of commonly used aggregates in asphalt concrete and introduces a model material. Sections 2.3 and 2.4 focus on the chemical and mechanical properties of the bitumen binder. In section 2.5, the principles of surface science are explained. Section 2.6 provides fundamental knowledge of water phase changes and ice interaction with substrate described in section 2.7.

2.1 Bituminous mixtures

Bitumen is used in more than 250 modern applications such as waterproofing, binding of composite materials, roofing, paving surfaces, and pipe wrapping³³. The most considerable portion (ca. 75%) of bitumen production is consumed in airports, waterways, road constructions, and ca. 20% is dedicated to roofing applications³⁴. Asphalt concrete is a composite mixture of aggregates glued together with a bitumen binder. Our findings in this thesis focus on understanding the fundamentals of icing on the bituminous road surface, but the outcomes are not limited to only this bitumen application.

2.2 Aggregates

Aggregates are the backbone of asphalt concrete and principal load-supporting components of the roads. Aggregates (or mineral aggregates) are hard materials such as crushed stone, rock dust, slag, sand, or gravel. Selected and sieved

aggregates are mixed with the bitumen binder to form asphalt concrete. Surface roughness, porosity, and chemistry of aggregates can affect the asphalt mixture's performance and water susceptibility^{35,36}. Changes can take place in the binder's properties as a function of the chemistry of aggregates in the mixture³⁷. Oxides in rocks such as Al_2O_3 , Fe_2O_3 , MnO , and MgO can protect the asphalt mixture from moisture damages, whereas this phenomenon is promoted by oxides such as SiO_2 in the rocks³⁷.

2.2.1 MACOR®

In this study, the average properties of commonly used mineral aggregates were modeled by a commercial machinable glass-ceramic named Macor®. It is a white, rigid, and porcelain-like material composed of 55 wt.% fluorophlogopite mica in a 45 wt.% borosilicate glass matrix³⁸. The approximate composition compounds of Macor® are: 46 wt.% SiO_2 , 17 wt.% MgO , 16 wt.% Al_2O_3 , 10 wt.% K_2O , 7 wt.% B_2O_3 , and 4 wt.% F (fluorine)³⁸.

2.3 Bitumen

Bitumen is a black, sticky, viscoelastic material and primarily originated from the crude oil refinery. For over 5000 years, bitumen has been used as waterproofing and binding material³³. The bitumen composition varies according to the crude oil source³³ and contains a complex composition of hydrocarbons (carbon 80–88 wt.%, hydrogen: 8–12 wt.%) and elements such as oxygen (0–2 wt.%), sulfur (0–9 wt.%), nitrogen (0–2 wt.%), and heavy metals such as vanadium (< 2000 part per million (ppm)) and nickel (< 200 ppm). In the following sections, we will discuss the properties of bitumen in detail. Parts of the discussions are based on "The Shell bitumen handbook" by Reed and Whiteoak³³ and a review paper from Lesueur³⁹.

2.3.1 BITUMEN FRACTIONS (SARA)

Bitumen can be separated into four characteristic finite fractions: saturates, aromatics, resins, and asphaltenes (initiated as SARA fractions) based on the molecules' solubility, polarity, molar mass, and aromatic content⁴⁰. The molecular weight of bitumen typically is in the range of 600–1500 g/mol³⁹. Bitumen, on average, contains saturates at (5–15 wt.%), which are non-polar long saturated hydrocarbons chains (C_nH_{2n+2}) containing (C20–C50) kinds of paraffin. This colorless or light color fraction has a low glass transition ca. -70 °C. Aromatics have a share of (30–45 wt.%) in the bitumen with yellowish or reddish color at room temperatures. Aromatic fraction has a higher viscosity than the saturates with a glass transition temperature close to that of the bulk bitumen at ca. -20 °C. Resins (30–45 wt.%) are polar aromatics. Unlike saturates and aromatics which are oily and liquidy at room condition, resins are black and solid without showing a distinct glass transition point. Resins and aromatics form the most considerable portion of the bitumen. These three fractions (saturates, aromatics, and resins) together are called maltenes. Asphaltenes are present in lower concentrations (5–20 wt.%), causing bitumen viscosity. Asphaltenes are in the form of black powder in room condition and form micelles while diluting in toluene solvent.

2.3.2 BITUMEN MOLECULAR STRUCTURE

Direct investigation of bitumen structure under X-ray or neutron scattering confirms the heterogeneous nature of bitumen. Early developed models such as sol-gel and dispersed polar fluid have a limited validity on describing bitumen behavior in different conditions, while colloidal structure can interpret many experimental results of bitumen. Resins as polar components of the maltenes have

critically contributed to bitumen stability, acting as a stabilizer for the asphaltenes in the colloidal bitumen structure. The colloidal model predictions are consistent with the collected results on the bitumen glass transition by thermal analysis³⁹. Giving weight to other hypotheses, it can be interpreted that solubility and wax content can control the bitumen morphology⁴¹⁻⁴³. It can be concluded that the bitumen molecular structure is very complex, and possibly co-crystallization over heterogeneous nucleation and interaction regarding the ratio of different components such as wax and polar molecular can alter the bitumen molecular structure⁴⁴⁻⁴⁸.

2.3.3 THERMAL PROPERTIES OF BITUMEN

Bitumen exhibits glass transition at ca. -20 °C, but depending on the bitumen source and its chemistry, the transition can happen in a broader range from 5 °C to -40 °C. Bitumen has low thermal conductivity, and due to its black color, most of the heat is stored in it and causes rutting in the long term. On the other hand, bitumen loses its viscoelastic properties in cold temperatures and causes cold temperature cracks. Phase change materials (PCMs) as heat capacitors can be tuned to absorb the excess heat at high temperatures and release the heat at required cold temperatures. In Chapter 4 of this work, the potential application of PCM modified bitumen in delaying condensation of moisture and its solidification as well as keeping bitumen ice-free at subzero temperatures is reported.

2.3.4 RHEOLOGY OF BITUMEN

In addition to the commonly used experimental analysis used for the other viscoelastic materials, several exclusively empirical tests such as needle penetration

and ring and ball test are designed for bitumen, based on the requirements and standards of different countries/regions. In this study, we followed EN 1426 standard for needle penetration, and the softening temperature was measured by using a ring and ball test based on the EN 1427 procedure. To analyze bitumen's low-temperature mechanical properties, we used a dynamic shear rheometer (DSR) at different temperatures and frequencies based on EN 14770 protocol. In the case of the viscoelastic material such as bitumen, several spring-dashpot configuration models attempted to explain the non-linear dependency of stress and strain versus time. Bitumen at cold temperatures exhibits more elastic properties. By lowering the bitumen temperature, the complex shear modulus reaches a plateau around a value of 1 GPa independent of the shear frequency and temperature ^{39,49}.

2.4 Bitumen Surface Microstructure

It is shown that the bitumen surface develops surface microstructures, namely, catana (bee structure), peri, and para domain ^{50,51}. Contradictory information exists on the origin and mechanism of the formation of these microstructures ^{41,44,51-53}. The catana domain morphology is dependent on the thermal history and the bitumen chemical composition. The surface buckling model can explain the surface wrinkling and formation of the catana domain due to the surface waxy layer mechanical mismatching stress with the substrate bulk bitumen ⁵². Mechanically scratching the catana domain on a micrometer scale using an atomic microscope (AFM) probe confirms that bitumen surface microstructures are a surface phenomenon ⁵⁴. Chapter 3 of this thesis will discuss the effect of cold temperatures on the bitumen surface microstructures in detail. Bituminous surfaces are exposed to condensation and freezing at cold temperatures. The principles of wetting and phase change are explained in the following sections.

2.5 Surface Energy and Wettability

The topic of wetting describes how a liquid medium can maintain interaction with a solid when they are brought into contact. This contact zone between two separate materials is called a liquid-solid interface. Similarly, each of the liquid and solid mediums can form interfaces with surrounding vapor/air, namely liquid-gas and solid-gas interfaces, respectively. While molecules in the bulk liquid are experiencing net zero force by the same neighboring molecules, attractive forces from all directions. In contrast, the molecules at the interfaces are exposed to foreign molecules. Molecules in the interface prefer to remain in bulk due to this energetically unfavorable condition at the interface. The energy associated with creating each specific surface at the interface of two materials (i and j) is known as surface energy (γ^{ij}). Surface energy is the work required to increase the interfacial area by a certain amount. The unit is surface energy per area, or in other words, surface tension J/m², or N/m⁵⁵. On smooth solid substrates, the equilibrium contact angle (θ) is related to the balance between the horizontal component of the interfacial tension of liquid-gas (γ^{LG} , liquid surface tension), solid surface-gas (γ^{SG}), and liquid-solid (γ^{LS}) at the three-phase contact line. When placing a droplet on a surface, depending on the balance of surface tensions, the so-called spreading parameter (S), the droplet either spreads on the surface in a wetting state ($S > 0$) or will stay non-wetting ($S < 0$) with a spherical cap shape and minimized contact interface area.

$$S = \gamma^{SG} - (\gamma^{SL} + \gamma^{LG}) \quad (2-1)$$

The relation of surface tensions is defined by the Young equation ⁵⁶ on ideal flat, rigid, and chemically homogeneous solid surfaces as follows:

$$\cos \theta = \frac{\gamma^{SG} - \gamma^{SL}}{\gamma^{LG}} \quad (2-2)$$

However, due to surface roughness, impurities, and heterogeneous chemistry, ideal surface conditions are not always valid. Therefore, usually, the wettability of surfaces is examined by measuring the apparent contact angle θ^* of a liquid droplet on a surface (Figure 2.1).

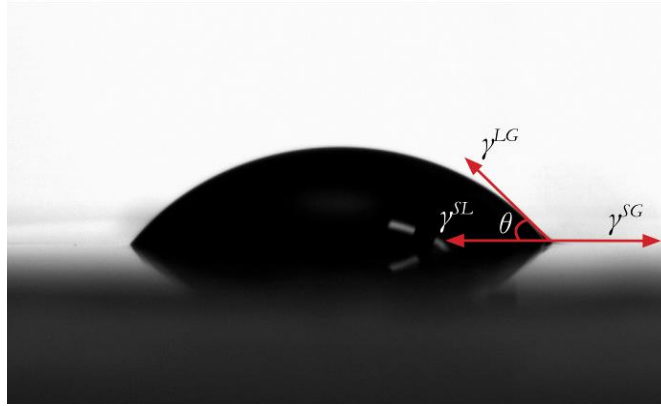


Figure 2.1 Liquid droplet on a solid surface in equilibrium condition. Arrows indicate surface tensions for each interface.

When the fluid is water, small contact angles ($< 90^\circ$) define the surface property of hydrophilicity. While, hydrophobicity is characterized by high contact angles ($> 90^\circ$), where θ is the equilibrium contact angle. Extraordinary non-wetting properties initially inspired by naturally water-repellent surfaces, such as lotus leaves ⁵⁷ and butterfly wings ⁵⁸. Micro- and nanostructured surface roughness impact combined with a low energy surface coating present named superhydrophobicity with $\theta^* > 150^\circ$ and low contact angle hysteresis ⁵⁹⁻⁶³. Contact angle hysteresis indicated droplet mobility by the difference between advancing and receding

contact angle. While the advancing contact angle, $\theta_{\text{advancing}}^*$ is the largest contact angle during a droplet wetting or moving forward and the receding contact angle, $\theta_{\text{receding}}^*$ is the smallest contact angle while reducing volume or dewetting. Figure 2.2 shows a sliding droplet down on a tilted solid substrate.

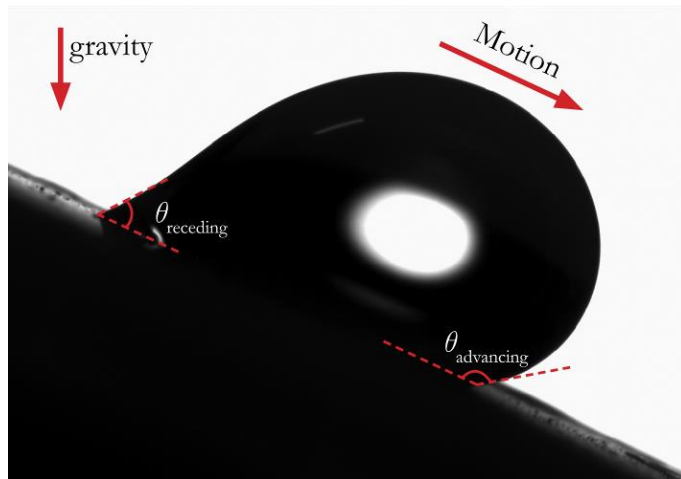


Figure 2.2 Sliding droplet down on a tilted solid substrate. Apparent contact angle in the front and receding contact angle in the rear.

If a drop sits on a surface combination of the surface roughness and trapped air between remains under the droplet, this state is called composite or Cassie-Baxter state with low CAH and easy to roll ⁶⁴. Otherwise, drop penetrates between pillars and liquid completely wets inside of the pillars, and this state is called Wenzel state ⁶⁵ (Figure 2.3).

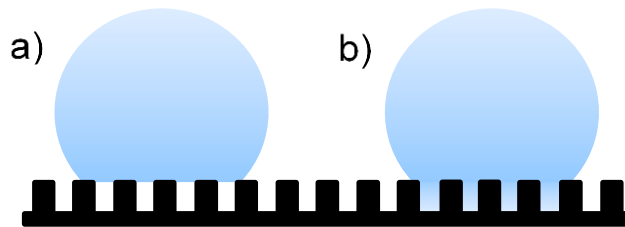


Figure 2.3 Wetting status on surface roughness. a) Cassie-Baxter state, b) Wenzel state.

Fabrication limits and fragility of most of such nano-engineered textures make them inappropriate for road materials. While using spraying processes can modify aggregates' surfaces to obtain the desired surface structures for superhydrophobicity ⁶⁶.

2.6 Water Phase Change Phenomena

After introducing the fundamentals of water wetting, the topic of water phase change related to the condensation and freezing phenomena will be addressed. Part of the discussion is based on the "Ice Physics" book by Hobbs ⁶⁷ and "Fundamentals of Engineering Thermodynamics" book by Moran *et al.* ⁶⁸. Water can exist in three states, gas (vapor), liquid, and solid (ice). Possible phase changes between every two of these phases are: condensation (and evaporation), which express the transition from vapor to the liquid state (and contrariwise); freezing (and melting), which respectively represent the change from liquid to solid-state (and vice versa); and desublimation (and sublimation), that describe the direct transition from vapors to ice (and inversed). In the following sub-sections, the topic of water phases on the water phase diagram will be continued and, then the mechanism of supercooling will be described by classical nucleation. Later, it will be explained in detail each of the related water phase change phenomena for this work such as, water condensation, freezing, and frosting.

2.6.1 WATER PHASE DIAGRAM

Figure 2.4 shows the conventional water phase diagram. The solid black line divides the pressure versus temperature diagram into three vapor, liquid, and solid phases. The triple point (TP), where three water phases meet and the critical point (CP) in thermodynamics, is the endpoint of the liquid-vapor phase. It can be noted

both pressure and temperature can contribute to water phase change. In the following lines, more details will be provided on condensation, freezing, and frosting. This study aims to understand the fundamentals of icing on road materials, therefore melting, evaporation of water are not further discussed according to their lower priority in this study.

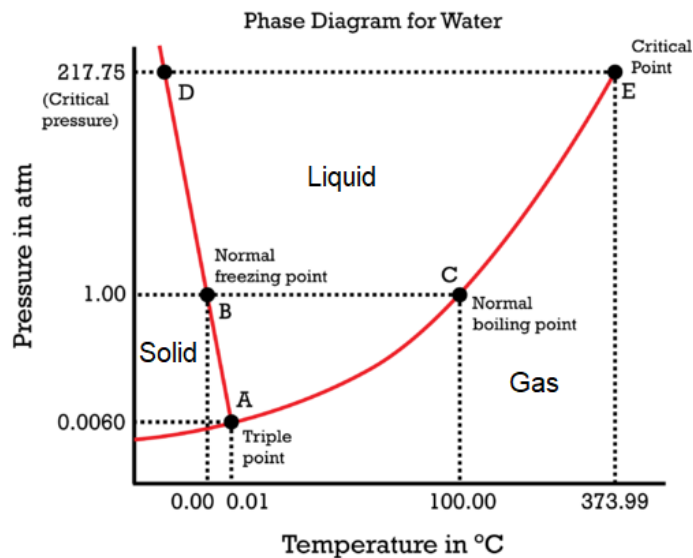


Figure 2.4 Conventional pressure versus temperature of the water phase diagram. The triple contact point (TP), where three water phases meet and the critical point (CP) in thermodynamics, is the liquid-vapor phase's endpoint (adapted from ⁶⁹).

2.6.2 CLASSICAL NUCLEATION THEORY

Nucleation theory provides the fundamental understanding of how phase change initiates. Here the case of freezing nucleation is described while changing a few notations can generalize the theory of freezing nucleation to the condensation and desublimation applications. Usually, water freezes from a supercooled liquid state. Over this thermodynamically unstable condition, nanoscopic molecular

assembly in the host phase, namely ice embryo ice embryos, are born and destroyed continuously unless they pass a critical size and continue growing. Homogeneous nucleation happens when only water molecules involve and initiates freezing nucleation. The critical size is defined according to an energy barrier derived by Gibbs free energy:

$$\Delta G = G_{surface} - G_{volume} \quad (2-3)$$

Taking notation of L for liquid and S for solid, the energy associated with the creation of an embryo can be formulated as:

$$\Delta G_{LS} = \gamma^{LS}A + n_s(\mu_s - \mu_L)V \quad (2-4)$$

Where γ^{LV} is the interfacial energy between the liquid and the ice phase and A is the surface and V is the volume of the nascent embryo; n_s is the number of molecules per unit volume of the ice phase, μ_s and μ_L are the chemical potentials of the solid and liquid phases, respectively. Furthermore, we can define the difference in chemical potentials as a function of measurable variables of temperature T and pressure P :

$$\mu_s - \mu_L = -k_B T \ln \frac{P_L}{P_S} \quad (2-5)$$

Where k_B is the Boltzmann's constant and P_L and P_S are the saturated vapor pressures over plane surfaces of water and ice at temperature T , respectively. By taking assumption of $V = \frac{4}{3}\pi r^3 \alpha$ and $A = 4\pi r^2 \beta$, where r is the embryo radius, which α and β both are numerical factors larger than unity and are used to adjust for non-spherical embryo shapes. Finally, it yields to:

$$\Delta G_{LS} = 4\pi r^2 \beta \gamma^{LS} - \frac{4}{3}\pi r^3 \alpha n_s k_B T \ln \frac{P_L}{P_S} \quad (2-6)$$

The Gibbs free energy plotted in Figure 2.5a shows the balance between driving volumetric released energy G_{volume} with opposing $G_{surface}$, the energy which has to be provided to create the new forming interface between the new frozen phase with the surrounding initial liquid phase.

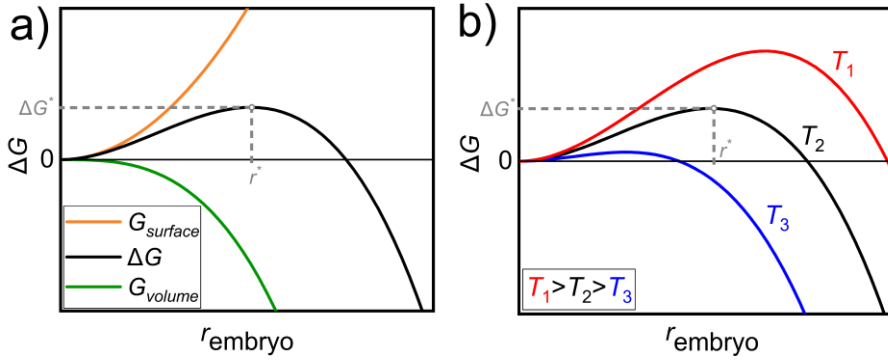


Figure 2.5 The difference in Gibbs free energy, as a function of ice embryo radius and liquid water temperature. a) Balance between driving volumetric G_{volume} with opposing G_{surface} Gibbs free energies, b) Gibbs free energy associated with nucleation at three different temperatures.

Therefore after a critical radius, the favorable volumetric energy increases faster and overcomes the opposing surface energy. At lower temperatures, supercooling requires a lower energy barrier and minor associated critical energy barrier to form a stable embryo Figure 2.5b. The value of the critical radius (r^*) can be calculated by setting $\partial \Delta G_{LS} / \partial r = 0$, we get:

$$r_{LS}^* = \frac{2\beta\gamma^{LS}}{\alpha n_s k_B T \ln \frac{P_L}{P_S}} \quad (2-7)$$

Given critical radius and substitution of r_{LS}^* , to equation (2-6), yields to corresponding critical Gibbs free energy barrier (ΔG^*):

$$\Delta G_{LS}^* = 16\pi\gamma^{LS^3}\zeta / \left(3 \left[n_S k_B T \ln \frac{P_L}{P_S} \right]^2 \right) \quad (2-8)$$

Where $\zeta = \beta^3 / \alpha^2$. If the homogeneous nucleation was the only possible mechanism of freezing, it could take an infinite time to initiate freezing a droplet. While in reality, during the heterogeneous nucleation, some other materials such as a solid surface, impurity in water, or a speck of foreign dust can contribute. In the case of heterogeneous nucleation numerical factor, $0 < f < 1$ as a function of the foreign particle size, surface, and substrate topography modifies Gibbs free energy barrier associated with homogeneous nucleation:

$$\Delta G_{LS,het}^* = f \cdot \Delta G_{LS}^* \quad (2-9)$$

2.6.3 CONDENSATION

Condensation is the change of water vapor into a liquid state. Condensation commonly happens when either a vapor in a gas state is cooled or compressed to its saturation condition. The available vapor pressure ratio to the maximum possible saturation pressure is shown as relative humidity percentage ($RH\%$). The temperature associated with the saturation condition is the dew point. Condensation can occur from vapor in contact with surfaces colder than the vapor dew point. In this case, the vapor in the vicinity of the surface cools, and the vapor pressure in the gas phase reaches a maximal threshold. Substrate wettability can significantly alter vapor condensation initiation and the condensed droplets' mobility. The effect of vapor RH and substrate cooling rate on the condensation and freezing on bitumen surface are discussed in Chapter 4.

2.6.4 FREEZING

As soon as an ice embryo size in a supercooled liquid exceeds the critical radius, the liquid water turns into ice. The water molecules inevitably do a transition from the liquid to a solid-state. Once the stable ice nucleation initiates, the supercooled droplet starts to freeze in a two-step process. The liquid state has higher energy when molecules can randomly make a free motion, while the solid-state has limited motion. Therefore, as a result of freezing, water molecules undergo a phase change. Over the so-called recalescent freezing, an explosive and fast latent heat volumetrically releases, the supercooled water turns opaque due to a slushy mixture of water and ice. The latent heat of phase change releases in a fraction of a second in a practically adiabatic condition and consequently self-heating the droplet temperature up to the equilibrium freezing temperature of ~ 0 °C. Over the second step of freezing, the remaining liquid isothermally freezes during a considerable several order of magnitude slower process compared to the initial step.

2.6.5 FROSTING

One of the prevalent examples of surface icing is ice nucleation from the vapor state, which is better known as frosting. Frosting happens when a surface at temperatures below the water freezing point is exposed to a sufficient amount of water vapor in the air; after that, frost formation and densification continue to cover the surface with ice crystals and dendrites. Although this process takes place on roads and is named black ice (thin transparent ice) in this study, we observed frosting after condensation freezing on the frozen droplets without having a detailed study on frost formation and densification patterns.

2.7 Ice and Substrate Interaction

Assuming the earlier mentioned liquid droplet on a solid surface undergoes the freezing process. The newly formed ice-solid interface replaces the initial liquid-solid interface. This work of adhesion per unit area W_a can thermodynamically describe the energy required to break the interface of the new-formed ice (I) with the solid substrate as:

$$W_a = \gamma^{SG} + \gamma^{IG} - \gamma^{SI} \quad (2-10)$$

Inserting γ^{SG} from equation (2-2) into equation (2-10) shows that:

$$W_a = \gamma^{LG} \cos \theta + \gamma^{IG} + (\gamma^{SL} - \gamma^{SI}) \quad (2-11)$$

The ice work of adhesion is scaled with the receding contact angle. Considering that the surface energies of ice and water are approximately equal ⁷⁰ and assuming that the interfacial energies are also similar, we can obtain ^{71,72}:

$$W_a \approx \gamma^{LG} (1 + \cos \theta_{receding}^*) \quad (2-12)$$

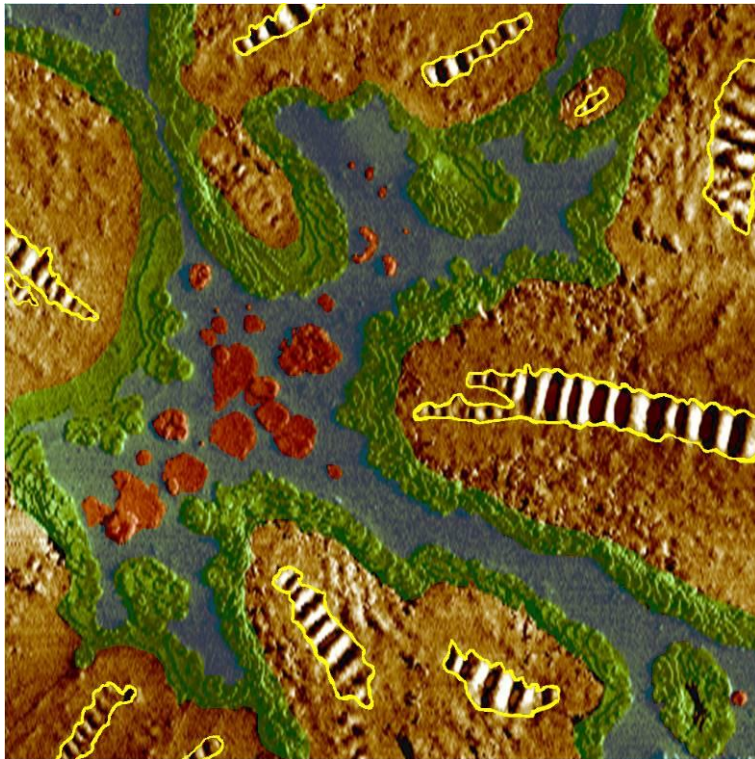
The receding contact angle is the smallest contact angle on the surface that results in the maximum work of ice adhesion ⁷³.

2.7.1 CONSEQUENCES OF ICING AND ITS PREVENTION

Having mentioned the general implications of the water phase change phenomena, the icing on surfaces leads to negative consequences in many applications such as roads. In this study, we aim to understand the fundamentals of the icephobic bituminous materials and introducing passive approaches, meaning one does not need the energy to induce de-icing or prevent ice formation. Needless to say, the drawbacks of the traditional ice removal approaches such as salt, heating, and mechanical removal. It has been shown that some hydrophobic surfaces could

potentially be of use for icing prevention, but superhydrophobic surfaces have not shown icephobic properties in all conditions ^{74,75}. The term "icephobic" refers to material properties under three main circumstances ^{74,76}: First, icephobic materials can remain ice-free longer than other materials at subzero temperature conditions ⁷⁷⁻⁷⁹; Second, surfaces with a low ice adhesion (shear strength) in the range of 500 kPa (and even lower, most favorably less than 150 kPa) can also be called icephobic ^{74,80-82}; and third, water-repellent surfaces and surfaces from which droplets self-dislodge are also categorized as SHS and icephobic materials ^{83,84}. Several parameters, such as surface chemistry ⁸⁵⁻⁸⁸, surface geometry and roughness ⁸⁹⁻⁹², thermal conductivity ⁹³, and substrate compliance ^{94,95}, can alter surface water affinity and later, ice nucleation and adhesion.

3 BITUMEN SURFACE MICROSTRUCTURE EVOLUTION IN SUBZERO ENVIRONMENTS



This chapter is published as:

Tarpoudi Baheri, F.; Schutzius, T. M.; Poulikakos, D.; Poulikakos, L. D. Bitumen Surface Microstructure Evolution in Subzero Environments. *Journal of microscopy*, 279, 3–15, (2020). <https://doi.org/10.1111/jmi.12890>.

3.1 Abstract

Bitumen is a widely used material employed as a binder in pavement engineering and as a surface sealant in construction. Its surface microstructure and microscale properties have been shown to be temperature-dependent, with effects manifesting themselves on surface composition and texture, including the formation of the visually striking catana “bee”-like structures. Despite the importance of a good performance of bitumen in subzero environments ($< 0\text{ }^{\circ}\text{C}$), the behavior of bitumen surface texture and composition at cold temperatures, affecting cracking, degradation, and road icing, has received practically no attention. In particular, such knowledge is relevant to world regions experiencing long periods of subzero temperatures during the year. Employing advanced atomic force microscopy combined with infrared spectroscopy (AFM-IR) and an environmental chamber, we demonstrate the ability to characterize surface structure and composition with nanoscale precision for a broad range of temperatures. We show that cooling bitumen to subzero temperatures can have several interesting effects on its surface micro-texture, nano-texture, and composition, especially on its three surface domains, catana, peri, and para. We found that the para domain coarsens and extends to form an interfacial transition domain (characterized by increasing surface roughness with peri domain composition) between the para and peri domains. We show that the catana and peri domains have a similar composition, but have different mechanical and chemical properties compared to the para domain. The essential findings of this work improve our understanding of the behavior of bitumen in subzero environments, aiding us in our quest towards attaining better road and sealant performance.

3.2 Introduction

Asphalt concrete is a composite material containing conventionally ca. 5% bituminous binder and ca. 95% mineral aggregates by weight³³. Even though only a small percentage of the asphalt concrete weight fraction is bitumen, due to its binding role, bitumen is indispensable and is mainly responsible for the mechanical and viscoelastic properties of the asphalt concrete mixture³³. Bitumen, a bi-product of crude oil, has a complex chemical makeup and should maintain its desirable properties over a range of temperatures and environmental conditions; this is an important aspect of pavement and sealant design⁹⁶. Previous work has shown that the bitumen surface develops three distinct microstructural domains after annealing: The “bee” structure or catana domain is wrinkled, with hills and valleys, and owes its name to the Greek words: cato (low) and ano (high). The catana domain is surrounded by the waxy peri (Greek meaning “around”) domain. The final domain is named para (Greek meaning neighboring) and is softer relative to the other domains⁵⁰. The peri domain consists mostly of lightweight saturates (waxy, thin film in nm scale)⁵². Crystallization of lightweight waxy saturates (n-heptane insoluble components⁹⁷) on the surface during cooling creates a thin film⁴³. Previous work showed that during cooling, the material surrounding and underlying the wax shrinks, compressing the film, and beyond a critical strain, forces it to buckle and to form wrinkles^{52,98,99}. After exposure to high temperatures, the surface composition of bitumen can change^{100–103}. The so-called “surface microstructures”^{41,44,52,104–107} and the properties of bitumen are also affected by temperature. Bitumen behaves like a Newtonian fluid above its melting point and as a viscoelastic material below it^{39,108}. It consists of four main hydrocarbon

fractions, saturates, aromatics, resins, and asphaltenes, each having different physiochemical and thermal properties¹⁰⁹. These are termed SARA fractions, based on increasing molecular weight and molecular polarity^{109–115}. Aromatics play an essential role in microstructure formation¹¹⁶. To date, the distribution of SARA fractions in the different surface domains of bitumen remains unclear.

Developing higher resolution microscopy techniques—especially chemical imaging—enable us to understand the complex surface chemistry and the rich surface microstructure of bitumen better. Previous works have used TOF-SIMS (time of flight secondary ion mass spectroscopy) to perform chemical characterization of bitumen based on molecular mass. While TOF-SIMS has excellent depth resolution (nanoscale)¹¹⁷, the main drawback of TOF-SIMS for imaging of bitumen is that it operates under vacuum, so to assure stability of a volatile sample like bitumen the sample is normally cooled to -80 °C, which is far from the conditions of interest for many applications^{118,119}. In comparison to AFM, it also has a lower resolution of 1 μm, which is not sufficient to capture all the chemical details of bitumen surface submicron-structures.

Other works on chemical imaging of bitumen used the s-SNOM (scattering-type scanning near-field optical microscopy) technique, which has a lateral resolution of 10 nm and a depth resolution of ~1-10 nm^{118,119}. Previous reports that used s-SNOM to characterize bitumen found a distinguishable chemical difference between the para and peri domains and showed that concentrations of sulfoxide and carbonyl groups are different in the peri and para domains¹²⁰; however, the IR spectra of these domains are not reported. The s-SNOM technique depends on the complex optical properties of the sample, tip, and underlying substrate of the sample to measure the amount of the scattered light from sample

¹²¹. Therefore s-SNOM performs best on rigid materials that also efficiently scatter light. However, it is more challenging to characterize, soft and high coefficient light-absorber materials such as bitumen, with s-SNOM ¹²¹, while materials with significant thermal expansion coefficient (α_{exp}) and small thermal conductivity are generally easy to measure with AFM-IR ¹²².

The AFM-IR technique uses the quick and short local thermal expansion of the under investigation material recognized as a force impulse for the cantilever and drives the cantilever into simultaneous multiple oscillatory modes (i.e., Eigenmodes). The cantilever oscillation amplitude is directly proportional to the absorbed IR light amount and absorption coefficient ^{121,123–125}. The deflection of the cantilever in the AFM-IR technique provides a direct measurement of the absorbed light, and it provides some advantages in comparison to other techniques, as discussed in the sequel. AFM-IR is a model-free IR absorption spectroscopy without band distortions and peak shifts, and the results of this technique are suitable for the analytical characterizing of the chemical composition of organic and polymeric materials such as bitumen with an excellent correlation to conventional FTIR (Fourier-transform infrared spectroscopy) results ¹²¹. A recently published study ¹²⁶ on bitumen using a similar AFM-IR device and sample preparation method reports on the chemical composition of the surface of bitumen at the nanoscale. Specifically, the authors report on topography maps, phase maps, functional group distribution maps, and infrared spectra of base bitumen samples before and after aging. The results strongly suggest that the chemical fractions of each phase on the bitumen surface are quite similar and have a higher polarity than that of the bulk material.

The main advantage of the AFM-IR technique in comparison to the ones mentioned above is that it allows investigating the chemical composition of the surface of bitumen with nanoscale resolution independent of surface complex optical properties and under environmental conditions that were more relevant for bitumen applications. Therefore, we chose the AFM-IR technique to perform cold temperature studies on bitumen samples in simulated winter conditions. The method has the potential to give insight into the mechanisms responsible for morphological and compositional changes of bitumen with temperature. Only a few works have investigated the relationship between surface topography and composition as a function of temperature. In addition, those that did, focus on high temperatures^{40,44,45,47,127–130} with limited knowledge existing for colder temperatures.

Here we show how the surface texture and composition of bitumen at the micro/nanoscale can undergo significant changes when cooled to subzero temperatures (< 0 °C). Employing AFM-IR, we observe a change in surface roughness at the para-peri interface during cooling, which we term the interfacial “transition” domain. We show that, chemically, the transition domain is similar to the para domain. We also show that within the para domain, certain island-like rougher features appear during cooling, which is termed “sal” sub-domain¹⁰⁴. At high cooling rates, the para domain is rich in sal sub-domains, but at slow cooling rates, the transition domain is dominant. The para domain was found to be chemically and mechanically distinct compared to the other surface domains. These findings advance our understanding of bitumen surface behavior, in particular as it relates to its use at cold climates.

3.3 Materials and Methods

3.3.1 MATERIALS

We used bitumen of medium softness (penetration grade 70/100, EN 1426, from the Middle East origin). This bitumen contains natural wax, with a needle penetration of 82 (0.1 mm), a softening point of 45.8°C, and dynamic viscosity of 163 Pa-s at 60 °C. Inter-laboratory studies on this bitumen using differential scanning calorimetry (DSC) at heating/cooling rate of 10°C/min have shown a glass transition temperature T_g of ca -20 °C and a melting peak of ca 28 °C. The SARA fractions reported are 3.8, 59.6, 22.2, and 14.6 respectively¹³⁰. The DSC results depend on the cooling rate as reported and discussed in the Appendix A.

The usual sample preparation methods for AFM studies of bitumen include heat⁵¹ and solvent casting¹³¹. The heat-casting method has less of an effect on bitumen's initial properties as it uses no solvent; therefore, we used it for sample preparation in this study⁴⁰. To avoid a thin oxidized top layer, we always extracted bitumen samples (1.5±0.5 mg) with a laboratory spatula at room temperature from a few centimeters below the surface of a bitumen bucket and spread it on a microscope coverslip. This created a thin bitumen film that covers an area of ~4 mm² with 500 µm thickness (see Figure A.1a and related supplementary information in Appendix A for calculation details). We then covered the bitumen samples with a Petri dish and annealed them on a hot plate (110 °C) for five minutes. Then, we transferred the samples to a refrigerator (3 ± 2 °C) for 5 min to quench them to room temperature. We chose this time and temperature to minimize high-temperature aging and to ensure a sufficiently smooth sample surface for

subsequent AFM scans^{40,53,130}. Thermal history plays a significant role in the molecular reorganization of bitumen components²⁵; therefore, following the above protocol was important in order to obtain consistent results. AFM scans were conducted on the prepared samples a few hours after preparation.

3.3.2 BULK CHEMISTRY CHARACTERIZATION

We characterized the chemistry of bitumen with the ATR-FTIR (Attenuated Total Reflectance Fourier Transform Infrared Spectroscopy) method using a Bruker Tensor 27 system (wavenumber range: 600 cm^{-1} to 3600 cm^{-1} ; resolution: 4 cm^{-1}). Each final spectrum represents an accumulation of 32 individual spectra of the bulk material. First, the diamond detector surface of the FTIR device was cleaned with acetone. Then, a small quantity of bitumen was applied on the detector crystal at room temperature covering an area of $\sim 2 \text{ mm}^2$. Before running the measurement, the lid of the FTIR device was closed, squeezing the bitumen on the diamond detector to create a thin uniform film.

3.3.3 AFM-IR CHARACTERIZATION

The AFM-IR technique can measure absorption spectra locally and can be used to chemically characterize a material with nanometer resolution in addition to the standard capabilities of an AFM. Both IR mapping and nanoscale IR spectra were carried out with a nanoIR2 device from Anasys Inc./Bruker at a suitable IR range of 892 cm^{-1} to 1958 cm^{-1} wavenumbers for characterizing organic materials such as bitumen.

Figure 3.1 presents an overview of the AFM-IR technique used in this study. It demonstrates chemical characterization measurements of the bitumen surface

microstructures. Figure 3.1a shows an example of an AFM phase scan of bitumen at $-20\text{ }^{\circ}\text{C}$ (false-colored), revealing several microstructural domains. The bee-like striped area (yellow line indicates its boundary in Figure 3.1a) is the catana (wrinkled) domain, surrounded by the peri domain. The false-colored green area is the transition domain, and the blue area is the para domain. The red highlighted areas within the para domain are the sal sub-domains. The sal sub-domain and transition domain emerge exclusively as a result of cooling to cold temperatures.

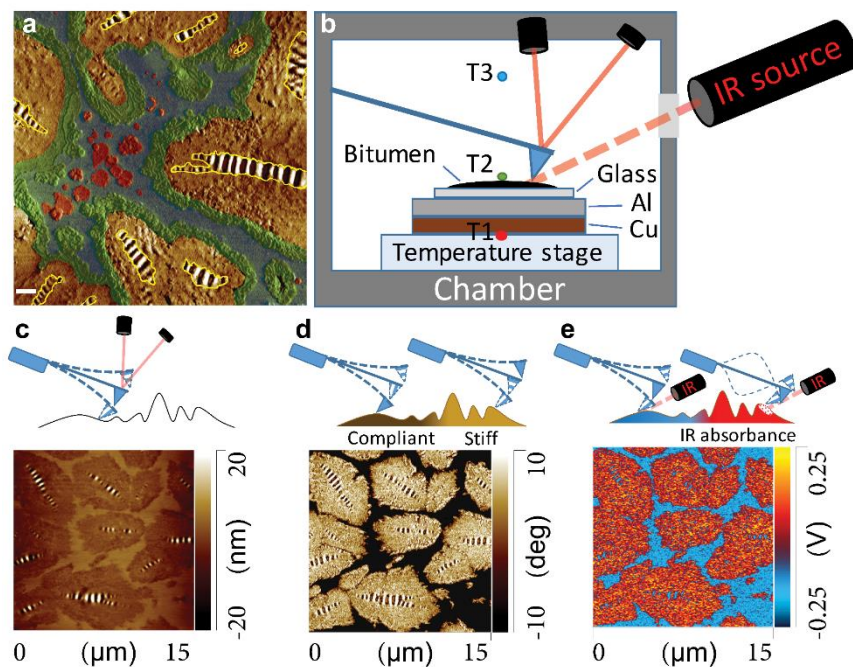


Figure 3.1 Principles and findings of the AFM-IR technique. a) Artificially colored phase image at $T1 = -20\text{ }^{\circ}\text{C}$ of a stepwise cooling sequence defined later. The highlighted regions with yellow stripes are the catana domains, and their surrounding area is the peri domain, false-colored green is the transition domain, blue is the para domain, and red denotes the sal sub-domain islands. White scale bar: $1\text{ }\mu\text{m}$. b) Schematic of bitumen sample on a glass substrate in the enclosed humidity and temperate chamber. We used copper and aluminum disks (each 1 mm thickness) to elevate the sample. Color dots show the location of three thermocouples, red dot: stage temperature thermocouple ($T1$), green dot: thermocouple for surface

temperature (T_2), blue dot: thermocouple as environmental temperature sensor (T_3). c) Drawing shows tapping cantilever following the surface profile to create the tapping AFM topography scan in first mechanical resonance mode ($T_1=25\text{ }^\circ\text{C}$). d) AFM phase image (phase map) detects surface properties such as mechanical compliance. Softer substrate shifts oscillating cantilever phase and causes phase lag, which corresponds to the darker phase contrast in the AFM phase scan ($T_1=25\text{ }^\circ\text{C}$). e) Schematic drawing of an AFM-IR scan. The pulse IR laser shifts the cantilever to its second mechanical resonance by thermal expansion of the excited substrate with the IR laser at a favorable wavenumber. Example of IR map at the same location scanned at 1456 cm^{-1} wavenumber ($T_1=25\text{ }^\circ\text{C}$).

Figure 3.1b shows a schematic indicating the position of the bitumen sample in the enclosed chamber while performing AFM-IR scans under controlled humidity and temperature conditions. We used aluminum and copper disks to elevate the sample position for the AFM-IR measurements. The environmental chamber position is under the AFM head to make an enclosed space for the cantilever probe and sample to run AFM-IR scans in controlled conditions. A thermoelectric, water-cooled device under the sample holder controls the sample stage temperature. The circulating water temperature never goes below its freezing temperature, and to prevent condensation and frost on the sample surface, all AFM scans were performed under continuous Nitrogen flow resulting in a dry environment ($\text{RH} < 3\%$, $T_3=20 \pm 3\text{ }^\circ\text{C}$). Since we cannot monitor the surface temperature (T_2) during scanning, we calibrated the sample surface temperature (T_2) versus the stage temperature (T_1) using a T-type thermocouple for similar conditions. Stage temperature T_1 goes to $-35\text{ }^\circ\text{C}$, T_3 (which measures the Nitrogen gas temperature) remains close to room temperature since we are continuously flooding the chamber with N_2 at room temperature. Moreover, the AFM tip is oscillated at a resonance frequency, in tapping mode, and intermittently contacts the surface. Therefore we do not expect cantilever properties to change due to temperature.

The sample was cooled stepwise from room temperature (T1: 25 °C, 15 °C, 0 °C, -10 °C, -20 °C, -25 °C, -30 °C, and -35 °C). We cooled the stage with a high cooling rate (~ -90 °C/min), to reach the next temperature of the stepwise cooling cascade and then held that temperature constant for a minimum of 15 minutes (extra time might be needed for cantilever tuning) before performing the scan. After scanning at T1=-35 °C, we heated the sample in two stage temperature (T1) steps: 0 °C and 25 °C, to complete the temperature cycle and recover the samples to the initial conditions. For further investigating the cooling rate effect, we examined slow (~ -1.5 °C/min) and fast (~ -90 °C/min) cooling rates for continuous cooling within a large temperature range, from T1=25 °C to T1=-20 °C. We first scanned samples at T1=25 °C, and then in a single step, the sample was cooled to T1=-20 °C. For AFM-IR scans conducted at T1=-20 °C, we waited a minimum of an hour to ensure that the observed effect is only due to cooling.

Bitumen is a soft, sticky material; therefore, to prevent cantilever tip contamination, we used AFM-IR in tapping mode as is commonly done for bitumen¹³⁰. The tapping cantilever (Figure 3.1c) follows the surface and generates the topography scan. The AFM phase scan contrast is generated by the differences between the oscillation phase of the driving signal sent to the AFM cantilever in tapping mode and its measured real mechanical oscillation response from the reflected laser^{50,132} (Figure 3.1d). It contains information on varying elasticity, friction, adhesion, viscosity, surface electrical charges, or chemical polarity. This measurement can provide qualitative information about how such properties vary over a surface. In particular, this is very relevant for bitumen imaged at different temperatures as its behavior can vary between elastic and viscous depending on the temperature. If more than one of these properties varies over a surface, then the

phase image will measure the combination of the different contributions. Due to the fact that there is a combination of effects that give rise to the contrast in a phase image, it is not easy to attribute the contrast to one material property. Therefore, we alternatively use terms of “stiff” and “compliant” to represent any of these material properties, and we refer to the AFM phase image, "phase map" such as Figure 3.1d.

We conducted all scans in an enclosed environmental chamber at the scan rate of 0.7 Hz for a scan area of 15 μm by 15 μm with the resolution of 500 scan points and 250 scan lines. During the conditioning time before each scan, the AFM cantilever was set back to its free oscillation distance (100 μm) to prevent tip contamination as bitumen has high volumetric variation during cooling and heating. Each AFM scan takes ~ 5 min. For each of the reheating steps, we quickly raised the sample temperature to reach the target temperature, and then, after about 30 min of the conditioning time, we performed an AFM scan with the same scan setting.

The schematic drawing in Figure 3.1e shows that the absorbed IR pulse by the sample during the AFM-IR scan causes a photothermal expansion. This results in an external impulse force, which causes an increase in amplitude at an alternate second oscillation mode of the cantilever. These two mechanical resonance modes occur simultaneously when the pulse frequency rate of the blinking IR laser, at a favorable IR absorption wavenumber for the sample material, is approximately equal to the frequency difference of the cantilever second and first mechanical resonances.

These data are used to map the surface chemistry (IR mapping and local IR spectra). IR maps are generated by the response intensity of each scan point of the

material to the absorbed IR wavenumber. The absorption units, in volts, show the amplitude deflection of the cantilever in its second mechanical resonance mode, due to the local thermal expansion of the substrate material after reacting to the blinking IR laser beam. The absorption units are not quantitatively calibrated according to the concentration of each chemical functional group. Qualitatively, the more responding materials to the selected absorbed IR wavenumber show relatively higher absorption units in volts ¹²¹. In order to highlight the inhomogeneity of the material and domains, we plotted the offset value of the IR map contrast. The offset function sets the average IR absorption units equal to zero, and therefore, the initial intensities below average become negative.

The acquired AFM-IR spectra have high spatial resolution due to the fact that the cantilever probe has a sharp tip (~10 nm diameter) and high spectral resolution because of the sensitive laser feedback loop, which is able to detect fine cantilever deflections. When the bitumen surface absorbs a laser pulse, it expands deflecting the cantilever tip. The cantilever oscillation amplitude is proportional to the absorbed energy in sample ¹²³. The cantilever oscillation peaks are collected for different IR laser wavelengths, Fourier-transformed, and plotted as amplitude versus wavenumber. Nanoscale IR spectra show characteristic peaks at specific wavenumbers, which are used to define chemical functional groups.

3.3.4 IMAGE ANALYSIS: AREA FRACTION CALCULATION

Traditionally, the contrast in the AFM phase images is used to define qualitatively the borders separating the para and peri domains. Several device and set up specific effective parameters can be identified for the thresholding value defining the border, such as a difference in mechanical properties of each cantilever,

energy, and force (set point) of the tapping cantilever; and substrate surface mechanical compliance as a function of temperature effects. As these parameters are setup-specific, it is not possible to report a single value for the phase scan to threshold the boundary of domains. Moreover, the existence of a high phase contrast in the catana (bee) domains disturbs the automatic thresholding procedure of the other domains. Therefore, the values reported here are selected to be specific to the experiments performed.

The phase contrast fades, and its sensitivity decreases at the colder temperatures because the stiffness of the tip-sample contact gets closer to the cantilever's stiffness. Darker colors in the phase map indicate phase lag between the driving and response frequencies. This occurs mainly in the relatively compliant parts of the sample. However, it is not feasible to convert phase map information to quantitate mechanical properties. For qualitative purposes, approximately the boundary of peri and para domains shows values in the range of zero to 0.5 degrees, which is the boundary of the relative stiff peri domain and compliant para domain while phase degrees of 0.5 deg or larger indicating a substantial change in stiffness.

Based on the AFM phase map analysis, we measured the surface area fraction for each of the domains. Even though half a degree of contrast in the phase image is sufficient to define peri and para domain boundaries, we measured the maximum contrast between these two peri and para domains to be 30-40° degrees. However, from the AFM phase contrast (an example shown in Figure 3.2e and Figure 3.2g), the para domain always has negative values (phase lag), but peri domain has heterogeneous phase value (shown as a non-uniform color contrast in visualized image). Sal sub-domain and transition domain also have heterogeneous phase makeup but close to para domain phase contrast. We recorded AFM in trace

(forward) scans. These are left to right scans in the standard AFM scan configuration. Therefore, the narrow shadow at the boundary of transition and para domains, as well as the sal sub-domain and para domain, is darker than both domains at the left-hand side and brighter at the right-hand side (Figure 3.2f and h). This narrow shadow between domains helps to define the boundaries of transition domain and sal sub-domain from the para and peri domains. The darker boundary around the para domain that emerges at cold temperatures we term as the transition domain (Figure 3.2f and h), and we identified the round dark islands in the para domain as the sal sub-domain. False colored para, peri, and transition domains and calculated the area fraction of each domain (A sequence of results for domain identification is shown in Figure A.3). Sources of error include AFM scan resolution, tip sharpness, and operator error during post-processing that are inevitable. To determine the error of the area fraction measurements, we ran 6 trials to calculate the area fraction for each domain for one randomly selected case (see example in Figure 3.4d, sample shown with the filled square symbol (■) at stage temperature $T_1 = -20$ °C). For small area fractions, such as those found for the sal-sub domain, the area fraction errors can be as high as 27%, but this value is less than 10% and 3% for the transition and para domains, respectively.

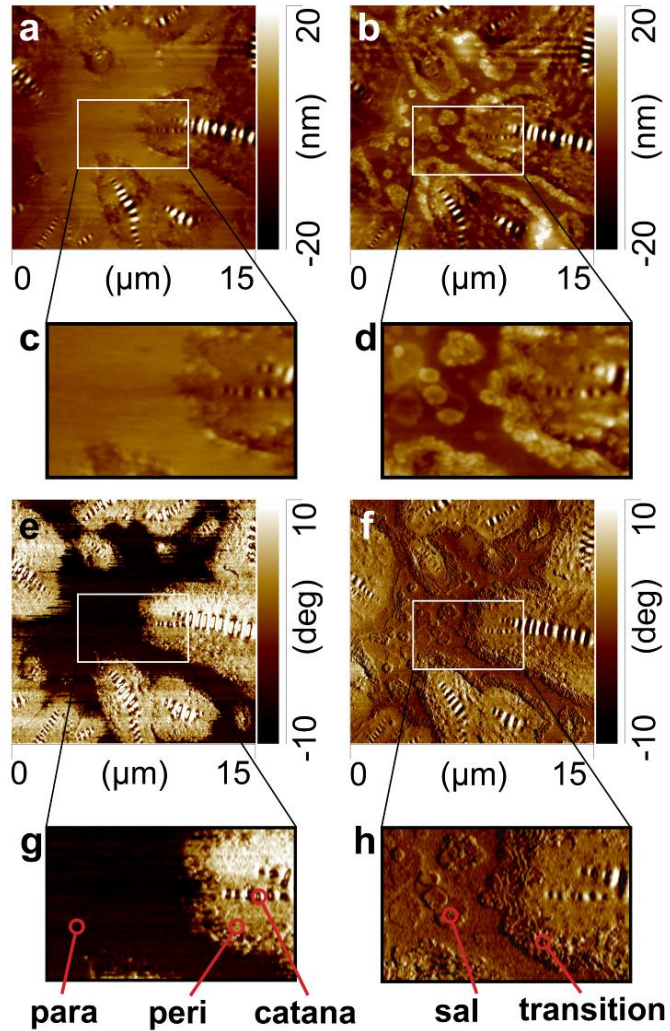


Figure 3.2 Effect of cold temperatures on the surface properties of bitumen. AFM tapping surface topography scans on bitumen at temperature steps of a) $T_1 = 25^\circ\text{C}$, and b) $T_1 = -20^\circ\text{C}$ during the stepwise cooling sequence, and their magnified areas are shown in (c) and (d), respectively. (e)-(f) Corresponding AFM phase images of the same locations as in (a) and (b), respectively. (g) The enlarged area of e showing three domains: catana, peri, and para. (h) Magnified view of (f), showing five domains at low-temperature in addition to the other three domains in (g).

3.3.5 IR SPECTRA ANALYSIS

Bitumen is a chemically complex mixture that has more than a thousand different types of molecule³⁹. Its IR spectra have peaks corresponding to certain chemical functional groups. To determine IR indexes for such chemical groups around IR peaks. We chose a straight baseline for each peak passing through the intersection of each spectrum limited with the vertical lines around each peak. The selected range around each peak and the availability of the chemical functional groups for the bitumen SARA fractions are reported in Table 3.1.

Table 3.1 **IR index and wavenumber range of the bitumen chemical functional groups based on FTIR and AFM-IR spectra.** The availability of chemical functional groups is defined for each fraction of SARA.

Functional groups	sulfoxide	aliphatic	aromatic	carbonyl
Wavenumber limit	958-1049	1353-1394 1408-1500	1546-1626	1690-1710
Index	$\frac{A_{1030}}{\sum A}$	$\frac{A_{1376} + A_{1456}}{\sum A}$	$\frac{A_{1600}}{\sum A}$	$\frac{A_{1700}}{\sum A}$
SARA fraction (availability of the functional groups)	----	Saturates Aromatic	---- Aromatic	----
References: ^{109,133}	Resin Asphaltene	Resin Asphaltene	Resin Asphaltene	Resin ----

3.4 Results and discussion

The wax content of bitumen plays a pivotal role in its low-temperature properties¹³⁴. The investigated bitumen has a natural wax content of 1%, as mentioned above. When bitumen is cooled from an annealing temperature, in this

case, 110°C, certain nano and micro-structures, and domains emerge on the surface of heat casted samples in most bitumen types. The catana (bee) structures mentioned earlier, for example, are attributed to a waxy surface film⁵² as they disappear when the sample is heated above the melting point of waxes at ca 60°C¹³⁰, (Figure 3.2a). Furthermore, they are indicators of the surface waxy layer mechanical mismatching with the bulk bitumen⁵².

The glass transition of the material reflects its bulk properties when the material undergoes during cooling a change from a viscous fluid to a glassy state¹³⁵. In the case of bitumen, once the sample is further cooled to the region of its glass transition temperature (in this case ca -20°C¹³⁰), there is a further evolution of these micro and nanostructures. As bitumen is a composite material, different components tend to phase-change at different temperatures. This is reflected in Figure 3.2a and Figure 3.2b that show AFM topography images of bitumen for the same location at T1=25 °C and T1=-20 °C, respectively, selected as an example from the sequential stepwise stage temperature cooling. Figure 3.2c and Figure 3.2d show magnified regions of Figure 3.2a and b, respectively. Figure 3.2e and Figure 3.2f are AFM phase images (phase map) for the same location at T1=25 °C and T1=-20 °C, respectively, where positive and negative values indicate relative higher and lower material stiffness, respectively. Figure 3.2g and Figure 3.2h are magnified regions of Figure 3.2e and Figure 3.2f, respectively.

The phase images, reflecting the sample interaction with the tip of AFM, corroborate what has been reported in literature⁵⁰ and shows at both temperatures there is a distinct difference between para and peri domains indicating the relative stiffness and adhesion of the domains increasing from para to peri. The softer part of the material has a more substantial interaction with the AFM tip resulting in the

darker image. The peri domain is hard and rough, and its surface coarsens at colder temperatures (see Appendix B, Figure B.1). In contrast, the para domain is relatively soft and based on the corresponding topography scan, it is also smooth. Figure 3.2h shows that with cooling, there is less contrast between the domains as they reach their glassy state, and furthermore, two main evolutions of the surface microstructure take place. The first in the para domain, where we see the appearance of protruding islands, the so-called sal sub-domains¹⁰⁴ and second in the peri domain the formation of an interfacial “transition” region at colder temperatures.

Previous studies have shown that different SARA fractions of bitumen have different glass transition temperatures (T_g) that are affected by their composition, ranging from -88 °C to 60 °C, increasing from low molecular weight saturates to high molecular weight asphaltenes¹⁰⁴. This has the consequence that different microstructures appear at different temperatures. In addition, similar studies have shown that the sal sub-domain contains the lowest molecular weight amorphous alkane of the para domain and remains amorphous, not crystallizing at deeply subfreezing temperatures¹⁰⁴. We also see that with cooling, the para domain stiffens relative to the peri and catana domains, but the transition domain and sal sub-domain remain noticeably soft relative to the peri and catana domains (see Appendix A, Figure A.3, and Figure A.4). During stepwise cooling, the sal sub-domain can grow to about 1 μm diameter. The transition domain has $0.5 \pm 0.1 \mu\text{m}$ rather uniform width with some locations, such as sharp corners featuring a higher width of 1-2 μm . For a high cooling rate of $\sim -90 \text{ }^\circ\text{C}/\text{min}$, an individual sal sub-domain equivalent diameter is limited to $\sim 100 \text{ nm}$ beads, while the transition domain is narrower and has a width of a couple of hundred nanometers. In the case

of a slow cooling rate, ~ -1.5 °C/min, it is difficult to detect the sal sub-domain, and the boundary of the para and peri domains features a diffuse transition domain.

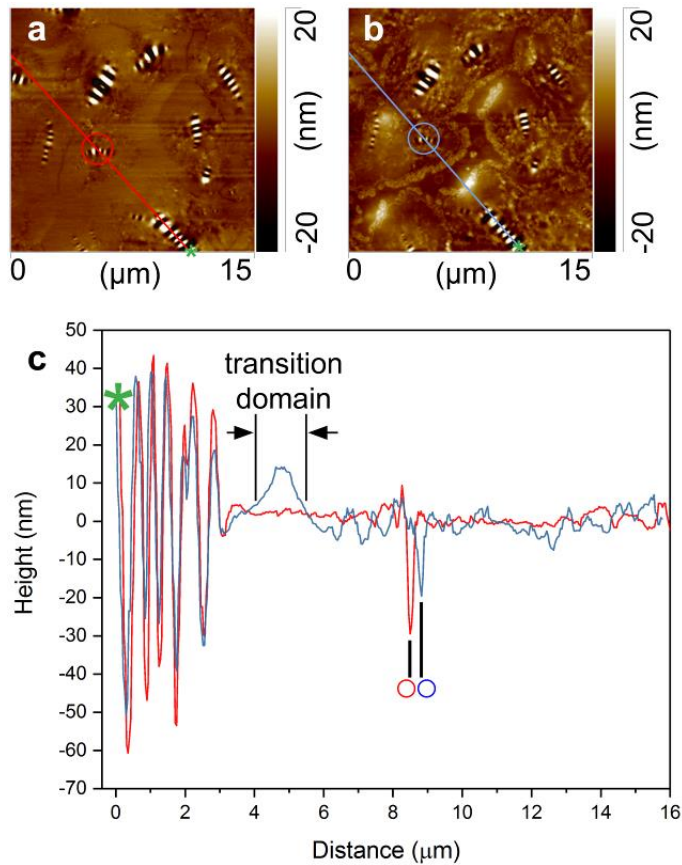


Figure 3.3 Effect of temperature on surface roughness in specific domains. AFM topography images at steps, a) $T_1=25$ °C, and b) $T_1=-20$ °C of the stepwise cooling sequence. c) Lines indicate topographies of bitumen at $T_1=25$ °C (red) and $T_1=-20$ °C (blue) in approximately the same location. The green asterisk is the zero point of the line profile (Distance = 0 μm). Marked points by circles are the valleys of the catana structures in the vicinity through which the line passes, to show that microstructures shift their position relative to each other as a consequence of the cooling.

Figure 3.3a, and b show representative bitumen AFM topography scans at two different temperatures, $T_1=25$ °C and $T_1=-20$ °C, respectively. Also shown are

the paths traveled by the AFM tip along the surface, crossing a catana structure, and the emerging transition domain defined earlier. These paths are chosen at practically the same location of the same sample and produce the topography landscapes of Figure 3.3c, showing the effect of reducing the temperature from $T_1=25\text{ }^\circ\text{C}$ to $T_1=-20\text{ }^\circ\text{C}$ on the microstructural. It can be seen that a typical catana domain has a length of $4\pm 3\text{ }\mu\text{m}$ and a maximum amplitude of $100\pm 50\text{ nm}$. Cooling causes the material to shrink, and therefore the distance between surface microstructures changes and the bee structures to shift (marked with a circle) at cold temperatures in comparison to their original location at room temperature. It is clear that cooling affects the surface texture of bitumen in all areas and in particular, the emerging sal sub-domains and transition domains (see Figure A.5 where domains are defined on the topography plot based on the corresponding phase scans). After cooling, the amplitude and length of the bee structure decreased by 10-20% while the wavelength varied around its initial value, Figure 3.3c. (For more details see Figure A.7 in the Appendix A). The profile also shows the drift of the microstructures as a result of the cooling. One possible explanation for the appearance of the sal domains was discussed by Masson et al.¹⁰⁴ is that the sal sub-domain and the transition domain have less volumetric changes than that of their surroundings, due to the fact that they have a different composition and as a result different glass transition temperatures (T_g).

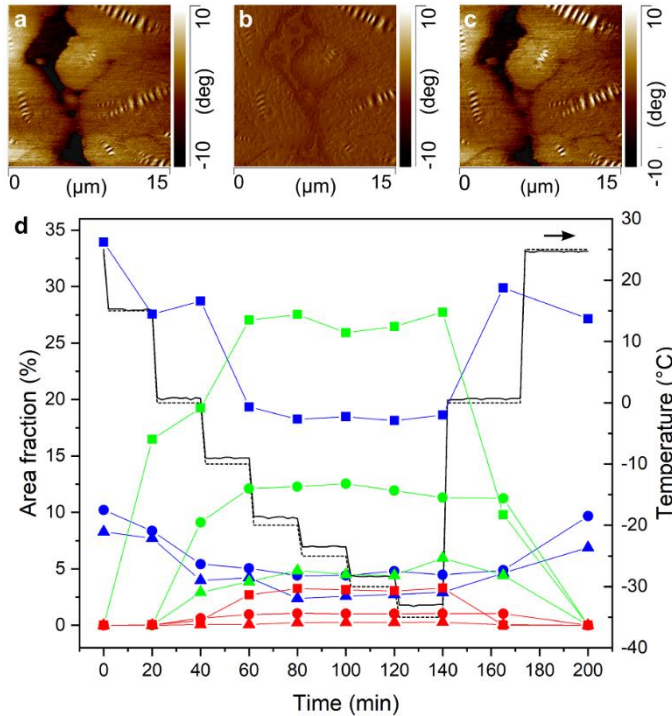


Figure 3.4 Effect of temperature on bitumen surface domains. Example of AFM phase image at the same location, during the stepwise cooling cycle. a) T1=25 °C, b) T1=-35 °C, and c) T1=25 °C (reheated to the initial condition). d) Area fractions of the sal sub-domain (red), para domain (blue), and transition domain (green) vs. time at different stepwise cooling temperatures of the stage temperature T1 (---) and surface temperature T2 (—), read temperatures from the right Y axis in panel (d). Symbols ■, ▲, and ● each show an independent AFM scan sequence on a fresh sample at the same location in dry conditions, showing qualitatively similar behavior.

Bitumen is highly temperature-sensitive, the evolution of the microstructures is further demonstrated in Figure 3.4a, b and c, which are examples of AFM phase images of the stepwise temperature cycles starting at T1=25 °C, cooling down to T1=-35 °C and reheating to T1=25 °C. We conducted each sequence of scans at practically the same location and repeated the scans at the same conditions on three fresh samples. Considering the formation of new domains at colder temperatures,

the impact of the cooling on the area fraction of these domains was further studied. Figure 3.4d shows the area fractions of the sal sub-domain (red), transition domain (green), and para (blue) domain, at the bitumen surface and T1 and T2 vs. time. In addition to T1, the temperature cycles were measured at the surface of the bitumen (T2) and shown (recall the locations of the thermocouples for T1 and T2 in Figure 3.1b). The temperature history for T1 and T2 measurements are depicted by dashed and straight black lines, respectively. A comparison of the surface temperature T2 with the stage temperature T1 indicates that thermal lag within the sample is negligible, and the selected conditioning time for each step is sufficient to reach thermal equilibrium (see Figure A.1 in SI for thermal resistance calculation).

We see that the para area fraction decreases with decreasing temperature while the transition and sal area fractions increase with decreasing temperature. Initially, the para domain area fraction decreases while, simultaneously, the new transition domain and sal sub-domain emerge. Accordingly, the area fractions of the sal sub-domain and transition domain increase and eventually plateau (see a sequence of the image analysis, Figure A.3). As mentioned earlier, the sal sub-domains contain the lowest molecular weight amorphous alkanes within the para domain, which precipitate and protrude from the surface between -10 °C and -19 °C¹⁰⁴. The width of the affected area around the protruded zone is about 2-4 μm and the height of about 20 nm.

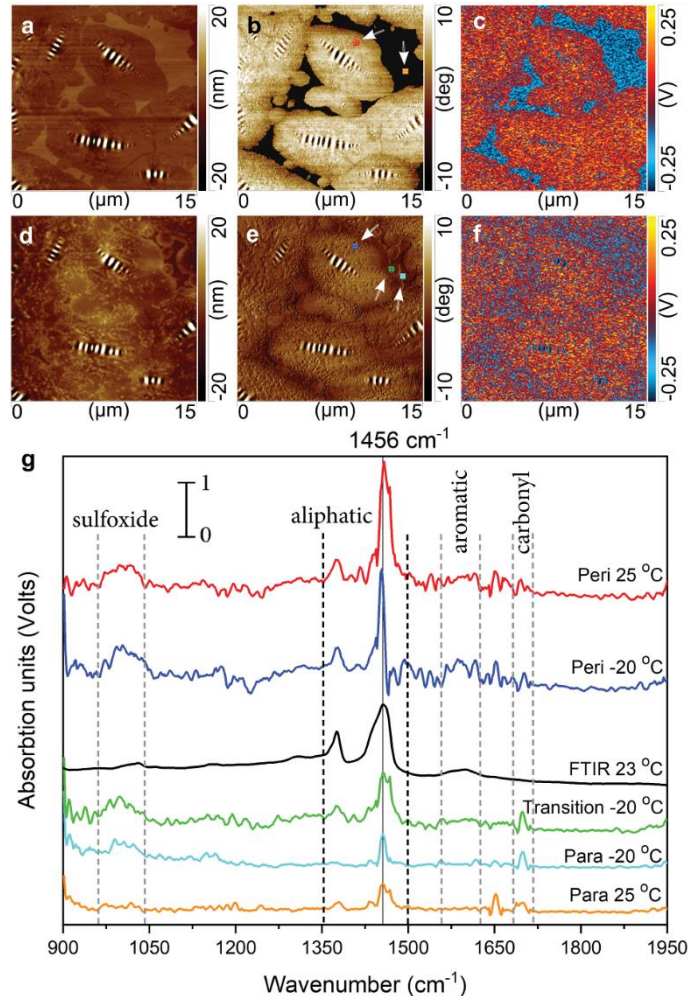


Figure 3.5 Effect of the slow cooling rate on the faded boundaries of the bitumen surface microstructure and determination of the chemistry of the transition domain. AFM-IR (a) topography, (b) phase, and (c) IR spectroscopy images for wavenumber 1456 cm^{-1} at $T_1=25\text{ }^\circ\text{C}$. (d) topography, (e) phase, and (f) IR spectroscopy images for wavenumber 1456 cm^{-1} of bitumen at $T_1=-20\text{ }^\circ\text{C}$ (directly cooled from $T_1=25\text{ }^\circ\text{C}$ to $T_1=-20\text{ }^\circ\text{C}$ at a slow constant cooling rate of $\sim -1.5\text{ }^\circ\text{C}/\text{min}$). (g) AFM-IR spectra smoothed by Savitzky-Golay function using a polynomial order of five fittings on six neighboring points. Spectra of bitumen at $T_1=25\text{ }^\circ\text{C}$ (para: orange line, peri: red line; see (b) for locations) and $T_1=-20\text{ }^\circ\text{C}$ (para: cyan line, peri: blue line, transition domain: green line; see (e) for locations) and the original bulk FTIR spectra at $23\text{ }^\circ\text{C}$, black line. The straight vertical line shows the location of 1456 cm^{-1} wavenumber.

Figure 3.5a, b, and c show topography, phase, and chemical IR mapping (at wavenumber 1456 cm^{-1} ; main H-C peak of bitumen) of the sample at $T_1=25\text{ }^\circ\text{C}$, respectively. Figure 3.5d, e, and f show the same information at practically the same location, but for $T_1=-20\text{ }^\circ\text{C}$, after cooling at a relatively slow cooling rate ($\sim -1.5\text{ }^\circ\text{C}/\text{min}$) directly from $T_1=25\text{ }^\circ\text{C}$ to $T_1=-20\text{ }^\circ\text{C}$). Figure 3.5g shows the absorbance spectrum vs. wave number for bulk FTIR ($\sim 23\text{ }^\circ\text{C}$); local nanoscale IR spectra of the peri and para domains at $T_1=25\text{ }^\circ\text{C}$; and the peri, para, and transition domains at $T_1=-20\text{ }^\circ\text{C}$. The locations where local nanoscale IR spectroscopies were performed are shown with squares in Figure 3.5b and e.

Previous studies showed that the IR spectra of the SARA fractions have high similarity¹⁰⁹, but their concentrations are different at the bitumen surface microstructures¹⁰⁴. The straight vertical line (Figure 3.5g) shows the location of the 1456 cm^{-1} wavenumber on the IR spectra. The peri domain is already a crystallized domain at $25\text{ }^\circ\text{C}$, as it has a higher percentage of paraffinic and saturated compounds¹²⁰. The peri domain shows a clear contrast with the para domain at $25\text{ }^\circ\text{C}$. On the other hand, at colder temperatures, the para domain becomes as stiffer as the peri domain and sal sub-domains, which consist of the light molecules of the para domain¹⁰⁴. Stiffer para with the denser molecular arrangement at $-20\text{ }^\circ\text{C}$ and sal-sub domain makeup result in an increase of the IR signal intensity and noisier IR map of the surface domains at $-20\text{ }^\circ\text{C}$ (Figure 3.5e) compared to $25\text{ }^\circ\text{C}$ (Figure 3.5b). The IR peak is broader around 1456 cm^{-1} wavenumber for the IR spectra of peri and para domains at $25\text{ }^\circ\text{C}$ and the transition domain at $-20\text{ }^\circ\text{C}$ compared to peri and para domains at $-20\text{ }^\circ\text{C}$.

AFM-IR is a mechanical technique; thus, the tapping IR spectra have inherent noise signals. To facilitate the distinction of the trends, we smoothed

the AFM-IR spectra by the Savitzky-Golay function using a polynomial order of five, fitting six neighboring points (original spectra is reported in Figure A.9). Bitumen has reference characteristic IR absorption spectra peaks (1376 and 1456 cm^{-1}) corresponding to the bending vibration of CH_2 and CH_3 aliphatic hydrocarbons^{136,137}. Owing to the bitumen composition as a mixture of various hydrocarbons, these are present in all types of bitumen¹³⁷. These peaks are also strongly present in both the bulk bitumen FTIR signal (black line at Figure 3.5g), and the local nanoscale IR spectra from the different domains probed. Therefore, the wave number 1456 cm^{-1} was selected for the IR mapping. The results show that the peri domain has a distinct chemical signature compared to the para domain (Figure 3.5c). In cold bitumen, however (Figure 3.5e, and f, at $T_1 = -20\text{ }^\circ\text{C}$) the boundary of the peri domain is chemically and mechanically practically indistinguishable from the para domain. At $T_1 = 25\text{ }^\circ\text{C}$, although the nanoscale IR spectra of para and peri domains follow the bulk FTIR signal, there are also significant deviations around wavenumbers 958-1049 cm^{-1} and 1353-1394 cm^{-1} and later from 1546 to 1626 cm^{-1} and 1690 to 1710 cm^{-1} (Figure 3.5g). As a consequence of cooling, the nanoscale IR spectra intensity of the para domain at $T_1 = -20\text{ }^\circ\text{C}$ shifts upward around wavenumbers 958-1049 cm^{-1} (Figure 3.5g). IR peak values of 1030 cm^{-1} are attributed to the sulfoxide functional group¹¹⁶ which are present in resins and asphaltene fractions¹⁰⁹.

In order to quantify the intensity of the major peaks in Figure 3.5g, we integrated the different areas, \mathcal{A} , under the curve around a band maximum (A_{peak} shows area under each band maximum and above straight baseline crossing spectra at limiting wavenumbers). Based on previous studies^{116,138,139} We defined the FTIR indexes and the limits of integration as follows: sulfoxide (A_{1030} : 958-1049 cm^{-1}),

aliphatic (A_{1376} : 1353-1394 cm^{-1} and A_{1456} : 1407-1500 cm^{-1}), aromatic (A_{1600} : 1546-1626 cm^{-1}), and carbonyl (A_{1700} : 1690-1710 cm^{-1}) groups. The total area is defined as $\sum A = A_{1030} + A_{1376} + A_{1456} + A_{1600} + A_{1700}$ for each spectra. By dividing the areas under the peaks by the total area $\sum A$, we define an index for each absorbance band, in order to make comparisons possible. Indexes show the relative distribution of chemical functional groups for each spectrum. For some specific cases, the difference of various domains is within the error bars and, therefore, not significant. These results, as well as the availability of the chemical functional groups for each fraction of the SARA fractions^{109,133} are shown in Table 3.1 and Figure 3.6, respectively. As indicated, previous reports that used s-SNOM to characterize bitumen found a distinguishable chemical difference between the para and peri domains (potentially causing different water wettability properties on these domains, see Appendix B, Figure B.2) and showed that concentrations of sulfoxide and carbonyl groups are different in the peri and para domains¹²⁰; however, the IR spectra of these domains are not reported. On the other hand, a recent study¹²⁶ on bitumen using a similar AFM-IR device and sample preparation method show that the peri domain also contains sulfoxide groups.

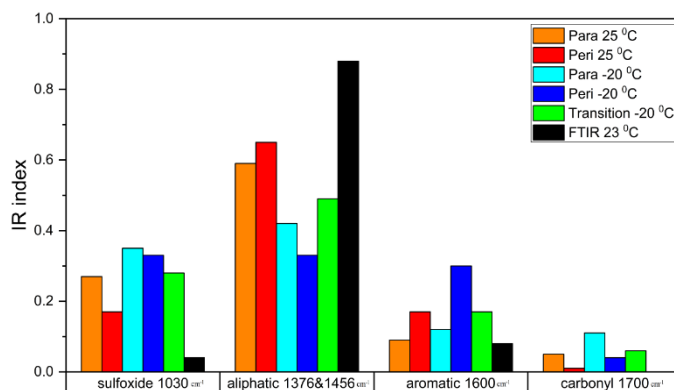


Figure 3.6 IR indexes of FTIR spectra and AFM-IR local IR spectra of the bitumen surface domains show the concentration distribution of the chemical functional groups in bulk and nanoscale, respectively, as a function of temperature. Functional groups are present around wavenumbers corresponding IR peak values, sulfoxide: 1030 cm⁻¹, aliphatic: 1376 cm⁻¹ & 1456 cm⁻¹, aromatic: 1600 cm⁻¹ and carbonyl: 1700 cm⁻¹. Each column bar shows average value with min and max values for at least three experiments. In cases of peri 25 °C, and para -20 °C, the bar represents 4 and 5 data points, respectively. FTIR column bar is an average of 32 measurements with a negligible error.

In contrast to the bulk FTIR, Figure 3.6 shows that all the major bitumen bulk functional groups are present in the para, peri, and transition domains. However, the relative amount varies with domain and with temperature. Comparing the para and peri at 25 °C, it is apparent that the carbonyl functional groups are considerably lower at the peri domain. At -20 °C, there is a shift in the functional groups with the branched alkanes (1376 cm⁻¹) relatively lower value in para and higher in the peri domain. In addition, there is a considerable increase in the aromatics in the peri at -20 °C. The transition appears at colder temperatures showing strong aliphatic peaks. At cold temperatures, the para domain surface functional groups change— A_{1030} and A_{1700} increased while A_{1600} and ($A_{1376} + A_{1456}$) decreased (aliphatic)—with the emergence of the sal sub-domain and transition

domain. It is also clear that the spectrum of the transition domain lies between the peri and para domains.

Figure 3.7a, b, c and d show topography, phase map, magnified phase map of the para domain, and chemical IR (at wavenumber 1456 cm^{-1}) images of bitumen at $T_1=25\text{ }^\circ\text{C}$, respectively. Figure 3.7e, f, g, and h show the same results at practically the same location, but now at $T_1=-20\text{ }^\circ\text{C}$, after a fast temperature reduction directly from $T_1=25\text{ }^\circ\text{C}$ to $T_1=-20\text{ }^\circ\text{C}$ with cooling rate of $\sim -90\text{ }^\circ\text{C}/\text{min}$ (i.e., continuous cooling from $T_1=25\text{ }^\circ\text{C}$ to $T_1=-20\text{ }^\circ\text{C}$ in half a minute). This cooling rate that can have a direct effect on the T_g , as discussed in the Appendix A, is limited by the fastest cooling rate capacity of the water-cooled thermoelectric device of the environmental chamber. By comparing the magnified panels of Figure 3.7 (Figure 3.7c and g), we observe that upon cooling, the para domain coarsens through the nucleation of the sal sub-domain. Hence, a narrow transition domain develops between peri and para domains after a fast cooling rate of $-90\text{ }^\circ\text{C}/\text{min}$.

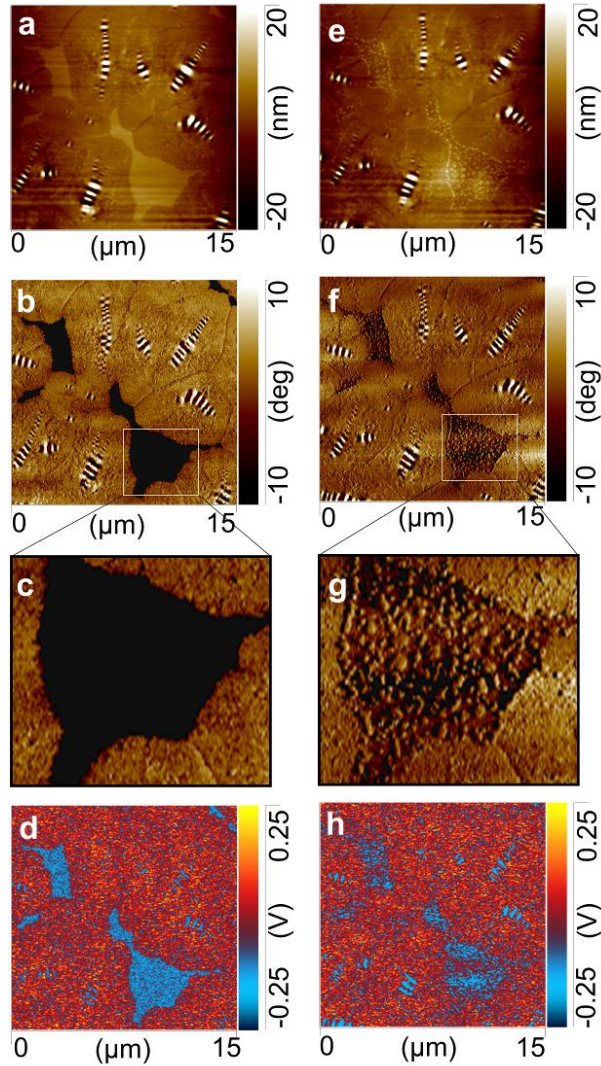


Figure 3.7 Coarsening of the para domain and plentiful appearance of the sal sub-domain with a narrow transition domain from very high cooling rates. AFM-IR results showing (a) topography, (b) Phase map (AFM phase), (c) Magnified phase map view of the marked area by the white square (see b), and (d) IR spectroscopy images for wavenumber 1456 cm^{-1} of bitumen at $T_1=25\text{ }^\circ\text{C}$. AFM-IR (e) topography, (f) phase map (AFM phase), (g) Magnified phase map view of the marked area by white square (see f) and (h) IR spectroscopy images for wavenumber 1456 cm^{-1} of bitumen at $T_1=-20\text{ }^\circ\text{C}$ (directly cooled from $T_1=25\text{ }^\circ\text{C}$ to $T_1=-20\text{ }^\circ\text{C}$ at an extreme cooling

rate of ~ -90 °C/min). Densely emerged sal sub-domain (see g) with limited transition domain, because of the fast cooling rate.

On the other hand, a slow cooling rate of -1.5 °C/min does not allow the development of a sizable sal sub-domain at the para domain (Figure 3.5e). In contrast to the fast cooling rate (shown in Figure 3.7), there is a reduced contrast between para and peri domains in a comparable slow cooling rate of -1.5 °C/min (Figure 3.5) due to the fact that the material does not have sufficient time for the development of a sizable transition domain between the para and peri domains. Moreover, a sharp narrow transition domain develops between peri and para domains, and numerous evenly spread sal sub-domains emerge in the para domain after experiencing a fast cooling rate of -90 °C/min. It is shown that the cooling procedure affects the distribution of the sal sub-domain as well as the size of the interfacial zone; this is a function of temperature, sal nucleation, and transport phenomena.

3.5 Conclusion

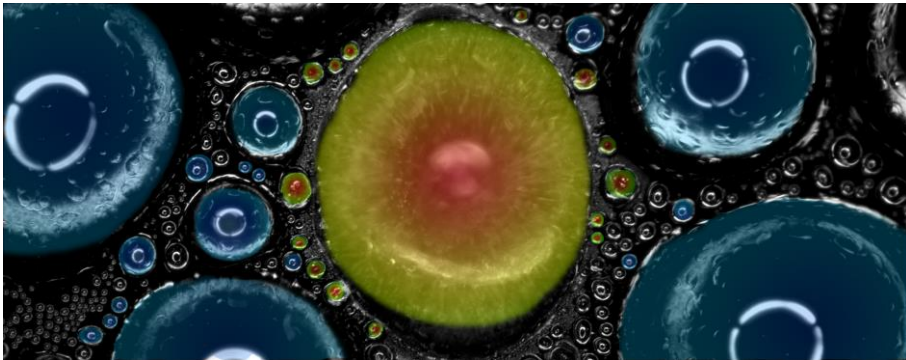
Employing advanced AFM-IR imaging, we showed that cooling bitumen to subzero environmental conditions causes significant changes in its mechanical, chemical, and topographical surface properties. We also found that new surface domains emerge at cold environmental conditions, namely, the transition domain between peri and para domains and the sal sub-domain, consisting of distinct island regions within the para domain. Nanoscale infrared spectroscopy showed that the transition domain has a chemical composition that is intermediate between those of the para and peri domains. We also showed that the peri and para domains are mechanically and chemically distinct at ambient conditions; however, when cooled

to subzero conditions, phase imaging and nanoscale infrared spectroscopy indicate that the properties in sample domains appear to become similar and that the transition domain—which separates them—emerges and broadens. This can be expected on the one hand as the different domains go through their respective glass transition and display stiffer properties. However, when cooled to subzero conditions, phase imaging and nanoscale infrared spectroscopy reveal that their properties become similar and that the transition domain—which separates them—emerges and broadens. And on the other hand, the diminishing of phase contrast is also a result of the sample becoming stiffer with cold temperatures – and therefore the contact stiffness becoming larger, which means that the tip doesn't penetrate the sample as much and thus the phase is less sensitive to material properties and therefore the contrast goes down in the phase images so that the AFM derived stiffness of different areas on the sample appear to be similar. Their emergence and distribution are highly dependent on how the sample is cooled, and the initial para domain size and shape. Also, very rapid, constant cooling rates over significant temperature differences, hinder the migration of sub-domains from forming large transition domains. Concerning chemical composition, we showed that the catana domain has the same chemistry as the surrounding peri domain. The amplitude of the catana structures decreases as a function of cooling, but the wavelength remains practically about the initial value. The results of this work significantly improve our fundamental understanding of the behavior of bitumen at subzero environmental temperatures, which, in addition to its fundamental value, has implications for the performance of bitumen in applications ranging from sealing to road engineering.

3.6 Acknowledgments

Financial support of the Swiss National Science Foundation under grant number 200020_169122 / 1 and the European Research Council under Advanced Grant 669908 (INTICE) are acknowledged. Beatrice Fischer of Empa is acknowledged for performing the FTIR measurements. Technical support from Bruker, specifically from Anirban Roy, Miriam Unger, and Igor Arkov, is gratefully acknowledged.

4 DROPWISE CONDENSATION FREEZING AND FROSTING ON BITUMINOUS SURFACES AT SUBZERO TEMPERATURES



This chapter is published as:

Tarpoudi Baheri, F.; Poulidakos, L. D.; Poulidakos, D.; Schutzius, T. M. Dropwise Condensation Freezing and Frosting on Bituminous Surfaces at Subzero Temperatures. *Journal of construction and building materials*, 298, 123851, (2021). <https://doi.org/10.1016/j.conbuildmat.2021.123851>.

4.1 Abstract

Freezing of atmospheric water on bituminous construction and road surfaces is a recurring event during winter. However, droplet freezing on bitumen and passive inhibition methods are poorly understood. Here we investigate relative humidity and substrate cooling effects on condensation freezing on subzero temperature bituminous surfaces and find that droplet freezing is explosive, with rapid local heating. We explain the related physics and find that relative humidity and cooling rate can affect droplet sizes and freezing temperatures. We then rationally embed phase change material microcapsules in bitumen, harnessing their latent heat to significantly delay freezing, demonstrating a viable option for frost mitigation.

4.2 Introduction

In countries with severe winter weather conditions, the clearance and maintenance of roads, roofs, and runways in winter is essential to ensure safe driving, living, and transportation conditions. Roads and many construction surfaces are commonly bitumen-based, and roads usually contain ca. 5 wt.% of bitumen (less than 20% by volume fraction)³³. Despite its low percentage, bitumen is the costliest portion of the mixture and due to its role as a binder and coating of aggregates, it has an important role on the overall mechanical and surface chemistry properties. Ice accumulation on bitumen-based surfaces, and in particular roads, is a multimillion-dollar problem with hidden costs such as asphalt road degradation (especially bitumen), and it has strategic and economic ramifications and drawbacks

ranging from delays in the delivery of goods to an increase in vehicular fuel consumption^{2,3}. Furthermore, several studies have shown a connection between road accidents and weather and pavement conditions in winter^{5,140–143}.

To address this problem, winter maintenance methods are employed, which can be categorized into two groups: passive methods (i.e., real-time maintenance is not needed) and active methods (i.e., site operation is needed). Conventional winter maintenance methods are mostly limited to active methods, which include chemical deicers, brine, and salt (predominantly sodium chloride). Salt is used to melt snow and ice, and is most effective at temperatures above -11 °C, close to the melting temperature of ice^{5,6}. The methods mentioned above may seem attractive at first, according to their low initial capital costs and facility of use¹⁴⁴, but eventually, salt and chemical deicers result in pavement degradation, which shortens the pavement service life^{145,146} and can be harmful to the environment, for example through freshwater salting⁹. Therefore, it is necessary to first improve our fundamental understanding of freezing on bituminous surfaces at the microscopic level, starting with dropwise frost formation from the condensation of environmental vapor, and then seek alternative, preferably passive methods for its deterrence. To this end, a possible passive method of mitigating the day and night temperature gradient leading to water freezing on bituminous surfaces, is to use phase change materials (PCM) in the bitumen composition, which act as thermal capacitors. It has been shown that temperature variations of PCM modified asphalt, caused by the daily temperature cycle, can be adjusted with the help of the latent heat of fusion of PCM²⁵.

Here we investigate the effect of environmental and surface temperature, relative humidity, and substrate cooling rates on condensation and ice formation

and propagation on the surface of bitumen using optical microscopy and infrared imaging techniques in a controlled climate chamber. Our results show that the initial condensation temperature is sensitive to the environmental relative humidity percentage ($RH\%$); however, it is practically independent of the cooling rate. After condensation, supercooled (an unstable state of a liquid below its freezing point) droplets can remain in the liquid state at lower subzero temperatures when, being cooled at faster rates or are in lower relative humidity conditions, where the droplets have smaller volumes. We then studied the physics of the ensuing explosively rapid freezing process from the supercooled water state and also capture and discuss an interesting mechanism of natural ice bridging among freezing drops, leading to frost propagation on a bituminous surface. Finally, we select and embed a phase change material (PCM) in the bitumen, at high-enough concentrations that still do not significantly affect mechanical¹⁴⁷ or surface properties, and study its heating effect upon solidification in delaying frosting, using differential scanning calorimetry and infrared imaging. We show that by rationally embedding PCMs within bitumen, we can markedly suppress and delay surface icing.

4.3 Materials and methods

4.3.1 MATERIALS

This study was conducted on virgin bitumen Q8 70/100 (penetration grade 70/100, density 1.029 g/cm^3 , of Middle Eastern origin) with a medium softness range of 82 (0.1 mm) needle penetration (EN 1426) and softening temperature (EN 1427) of $45.8\text{ }^\circ\text{C}$ and dynamic viscosity of $163\text{ Pa}\cdot\text{s}$ at 60°C . For this type of

bitumen, differential scanning calorimetry (DSC) results show a glass transition temperature of ca. -20 °C and a melting peak of ca. 28 °C with reported SARA (saturates, aromatics, resins, and asphaltene) fractions of 3.8, 59.6, 22.2 and 14.6 %, respectively ^{47,130}.

Direct tetradecane (a liquid PCM chemical) additives to bitumen target the principal properties of bitumen, which are critical for its performance in asphalt concrete ¹⁴⁸. Unlike the direct addition of such a PCM chemical, which softens the original bitumen and affects its principal properties ¹⁴⁸, microencapsulated PCM can survive the high temperatures and pressure that bitumen is exposed to during the artificial aging process without compromising its properties. It has also been experimentally shown that microencapsulated PCM safeguards bitumen from cold temperature cracks by releasing heat and improves bitumen's mechanical performance in subzero conditions ¹⁴⁹. PCM microcapsules can affect the mechanical properties of the modified bitumen although previous work has shown that PCM microcapsules at 25 wt.% concentration in bitumen does not negatively impact the mechanical properties of the bitumen binder at cold temperatures ¹⁴⁷. When latent heat is released by PCM microcapsules during crystallization, this can lead to bitumen softening at cold temperatures. Once crystallized, the PCM microcapsules can increase the complex modulus of bitumen, similar to filler minerals ¹⁴⁷. Concerning the leakage of the microcapsules, the PCM wax could potentially function as a rejuvenator oil for aged bitumen ¹⁴⁷. Microencapsulated PCM particles can be added during different stages of asphalt concrete preparation, and it has been reported that both wet (added to bitumen) and dry (added to asphalt mixture) processes alike have resulted in improved performance compared to non-modified reference samples ²⁷.

We selected a microcapsule PCM (μ PCM-21) fabricated by Microtek Labs, USA, to modify the bitumen in order to investigate icing delay. The core of the microcapsules consists of tetradecane (n-alkane $C_{14}H_{30}$), which has a melting temperature of ~ 6 °C and is known as a low-temperature phase change material¹⁴⁷. Its average particle size is reported by Kakar et. al.^{27,147} as being 21 μ m with 0.834 g/cm³ density and 195.5 J/g heat of fusion. The PCM material is encapsulated by a polymeric shell made of melamine-formaldehyde¹⁴⁷.

4.3.2 SOLUTION PREPARATION AND COATING

As a first step, the virgin bitumen was melted at 137 °C (mixing temperature) in an oven for 30 minutes. Then, the prepared dried microcapsules (at 110 °C for 5 minutes) were added to the melted virgin bitumen to reach 25% concentration by weight of the final blend. (see Appendix C, Figure C.1 illustrate the resistance of the PCM microcapsules to chemical, mechanical, and thermal stresses that they are exposed to during sample preparation.) Each of the virgin and modified melted bitumen solutions were then mixed in a speed mixer (Speed Mixer™, DAC 150.1 FVZ, Germany) for 2 min at 2,000 rpm. Next, 1 g of bitumen (virgin or PCM microcapsule modified) was removed with a spatula, and diluted in 4 ml toluene at 25 °C (Sigma-Aldrich 99.8%), then the entire solution was mixed using a shaker (Heidolph Multi Reax) at 2,000 rpm for 2 minutes. (Figure C.2 in Appendix C, shows a schematic drawing of the steps undertaken for the preparation of the sample.)

To fabricate thin virgin bitumen coatings, (termed “thin” virgin bitumen samples), we used a solvent casting approach. Here, 150 μ l of the virgin bitumen

solution was dispensed on a 22 mm diameter circular glass coverslip (Figure C.2). The liquid drop cast sample was left under a fume hood in ambient conditions until most of the toluene solvent evaporated, which we observed to occur within half an hour. Next, the samples were heated on a hotplate at 115 °C for 5 minutes, which is above the bitumen softening temperature and the toluene boiling temperature at 111°C, to ensure uniform and smooth surfaces. Thereafter, the samples were placed in a refrigerator for 5 min at 4 ± 2 °C to cool and solidify the bitumen layer on glass coverslips. Based on the mass and geometry of the sample and density of bitumen, the final bitumen thickness is expected to be ≈ 100 μm . This was further measured using an optical microscope (see Figure C.3 in Appendix C). This sample preparation method produces a smooth bitumen surface. We note that it is different from real-world conditions, where the surface of bitumen can be contaminated by foreign substances. Such idealized surfaces are useful for gaining fundamental insight into the effect of bitumen alone on ice formation.

To highlight the PCM effect, thicker bitumen samples (termed “thick” bitumen samples) were cast using layer by layer drop-casting technique to obtain a ~ 1 mm sample thickness as explained above for the thin films. Such samples were fabricated in Petri dishes, which had a diameter of 29 mm and a height of 10 mm. The final sample comprised four layers, with each layer originally containing 1,000 μl of virgin or PCM-modified solution. After the application of each layer, the sample was heated to 115 °C for 5 min to evaporate the solvent. After the fourth layer, the Petri dish samples were cooled in a refrigerator (4 ± 2 °C) for 5 minutes. To ensure that the solvent evaporated, the samples were given approximately 24 hours of conditioning time at room temperature before the experiments were conducted.

4.3.3 EXPERIMENTAL SETUP: CONSTANT COOLING RATE

“Constant cooling rate” experiments were used to study how ice formed on the thin virgin bitumen samples. The designed sample holder controlled the sample temperature by means of a central ~ 1 mm diameter copper pin section installed on a Linkam BSC 196 cryogenic stage (Figure 4.1a and see Appendix C, Figure C.4). The probability of ice nucleation is much higher at colder temperatures¹⁵⁰. Therefore, to ensure that we can observe the first droplet freeze, we opted to cool a limited region that we could visualize completely. Here, the sample should have a somewhat lower temperature relative to its surroundings, which also helps avoid the sample edge, which can affect condensation. The copper pin guarantees the initial condensation location, and freezing nucleation occurs in the field of view. Figure 4.1a shows a schematic drawing of the experimental setup with the location of the copper pin, which was used to locally cool the thin bitumen samples from the center of the region of study. The red and green circular symbols show the location of the cryogenic stage temperature (T_2) and the copper temperature sensor (T_1), respectively. To control humidity, nitrogen gas flow passes through the water bubbler, and humidified nitrogen mixes with the bypassed nitrogen line to regulate the relative humidity (RH) of the outlet via flow control valves. The use of a clean and controlled environment prevents the surface of bitumen from being contaminated by dust and foreign particles. Such particles can promote both condensation freezing nucleation and increase the complexity of the process on bituminous surfaces. Condensation freezing experiments were performed at five experimental conditions consisting of three cooling rates of 1 °C/min, 10 °C/min,

and 20 °C/min at *RH* 50% and three *RH* conditions of 20%, 50%, and 80% at 10 °C/min. The cryogenic stage operates at constant cooling based on the temperature feedback loop from T_2 (stage temperature). All experiments were initiated from $T_2 = 25$ °C after stabilization of the environmental temperature ($T_{env} = 21.5 \pm 0.5$ °C) and the defined *RH* condition (20%, 50% or 80%), this setting remained untouched until the end of the defined constant cooling rate at $T_2 = -50$ °C, considering 2 minutes of conditioning time at $T_2 = -50$ °C. Over the course of the experiment we also continuously recorded *RH*, T_{env} , T_1 and image frames (at constant frame per second rate); later we also synchronized frames with T_2 . We note that the maximum temperature difference between T_1 (copper pin) and T_2 (stage temperature) in all cases was less than 0.5 °C. Figure 4.1b, c are images of the copper pin from the optical microscope and infrared (IR) cameras.

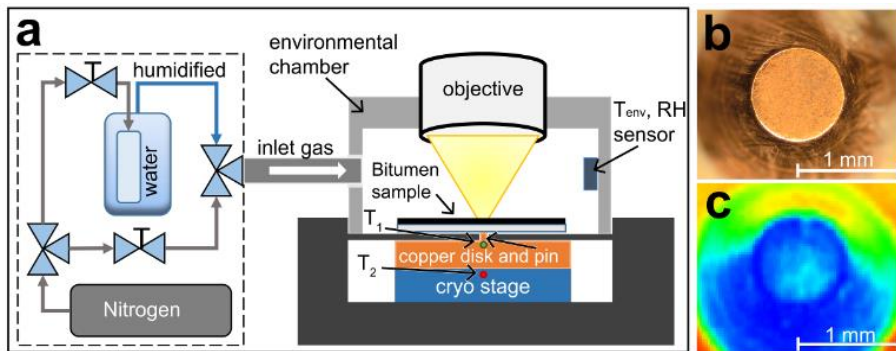


Figure 4.1 Experimental setup for constant cooling rate. a) Condensation freezing setup. Schematic of the inlet nitrogen gas supply system in the dashed line box (not to scale). The location of the thermocouple in the copper stage, T_1 , and the cryogenic stage feedback cryogenic stage, T_2 , temperature sensors are shown as green and red dots, respectively. The environmental sensor records chamber environment temperature T_{env} and relative humidity percentage *RH*. The location of the optical microscope objective or IR camera lens is shown as “objective”. b) Copper pin under the optical microscope at 5X magnification (without sample) and c) the same copper pin shown as seen from the IR camera (without sample).

The reported “condensation temperatures” were extracted from the corresponding frames of optical microscopy at the moment of detection of the first condensed droplets on the dry virgin bitumen surface (approximate resolution of 1 $\mu\text{m}/\text{pixel}$). We only recorded freezing events when supercooled droplets froze within the field of view, and the temperature of the corresponding frame is defined as the “freezing temperature”. Optical microscopy was performed using an Olympus BX60 optical microscope at 5X magnification and constant illumination in dark field mode for the condensation freezing experiment and 100X magnification in bright field mode to capture ice bridging. In a separate equivalent cryogenic stage configuration and experiment conditions, a FLIR SC7000 infrared camera was used to study the condensation freezing. (The location of the optical microscope objective or IR camera lens is shown as “objective” in Figure C.4a.)

4.3.4 EXPERIMENT SETUP: CONSTANT COOLING FLUX

The aim of the “constant cooling flux” experiments was to study ice formation on bitumen samples containing PCM. This was due to the fact that during constant cooling rate experiments, the feedback correction loop would compensate the heat released by the PCM. The constant cooling flux provides similar conditions without the existence of any correcting temperature feedback loop, thus capturing the heat released by the PCM microcapsules. We operated the thermoelectric element at constant input power, while the hot side of the thermoelectric element was kept at a constant temperature to reach stable constant cooling flux conditions on the cold side¹⁵¹ (Figure C.4b). To do this, another large temperature stage (CP-200HT-TT device from TE Technology Inc.) was used to

keep the hot side of the thermoelectric element at 0 °C (see Figure C.4b in Appendix C). At the given conditions, a thermoelectric element from Laird technologies™ (PC6-12-F1-4040-TA-W6) operated with constant 5V DC inlet voltage provides a nominal cooling flux of 6 [W] (online datasheet¹⁵²). Here, thick bitumen samples were used (thickness \approx 1mm). Optical and IR cameras were installed at a 30° angle with respect to the vertical, enabling simultaneous visualization (Figure C.4b). The IR camera measurements allowed us to acquire the average surface temperature of an approximately 3 mm by 4.5 mm sample area.

4.3.5 DIFFERENTIAL SCANNING CALORIMETRY (DSC)

DSC experiments were performed using a PerkinElmer® 7, 1993 device. The DSC analysis was conducted using 11.75 ± 2.50 mg of both virgin and PCM-modified bitumen. In addition, experiments were conducted on the bitumen specimens with ~ 1 μ l (1.22 ± 0.11 mg) of a single water droplet placed on top of a bitumen substrate in DSC sample molds under the same nitrogen purged environmental conditions of the DSC device (DSC baseline information when both sample holder were empty is provided in Figure C.5 of Appendix C.) We were interested in capturing material behavior at the cold temperature ranges with and without water. We performed the DSC measurements in a broader temperature range from 40 °C to -50 °C with two minutes of conditioning time at the limits of each thermal cycle. Three temperature cycles were performed in two 10 °C/min and 20 °C/min rates after initially heating samples to 40 °C from ambient temperature and conditioning for 2 minutes at 40 °C. (DSC analyses of virgin bitumen, PCM modified bitumen, and water¹⁵³ are reported in Figure C.6a, b, and Figure C.7, respectively, of Appendix C.)

4.4 Results and discussion

Bitumen, as a pavement and sealing material, is always expected to be in direct contact with water. There are many manifestations of such interactions, but here we are interested in studying water droplets initially formed as condensate from a humid environment, which can subsequently freeze upon reduction of atmospheric temperature. Water condensation forms on cold surfaces below the dew point. Supercooled water droplet freezing is a complex phenomenon^{78,84}. Upon cooling below its freezing point, condensed water is in a metastable, supercooled state, and in order to freeze, growing nuclei must overcome a free energy barrier to nucleation. Once overcome, further growth is energetically favorable, and such freezing is non-equilibrium and proceeds explosively fast (in the present study of the order of milliseconds)⁷⁸. During this time, the droplets only partially solidify, as latent heat is released as ice grows^{84,93}. Full solidification is completed in a subsequent markedly slower step (of the order of seconds; see Appendix C and Figure C.8), which is governed by the balance of the released latent heat and heat removal^{84,93}.

Figure 4.2 shows a micrograph and a temperature map of supercooled droplets condensed on bitumen. It can be seen that many droplets are still in a liquid state at temperatures far below 0 °C (surface temperature ~ -15 °C), while some droplets have frozen. Figure 4.2a shows a droplet that has just started to freeze and is marked with a dotted circle. Figure 4.2b shows an IR micrograph of a water droplet that has just started to freeze, and demonstrates that upon freezing—due to the rapidly released heat of fusion—the droplet actually attains a much higher temperature (the freezing equilibrium temperature of 0 °C) than its surroundings,

which are still at $-15\text{ }^{\circ}\text{C}$ (Figure 4.2b). Further implications of this heating phenomenon and its impact on droplet evaporation and freezing propagation will be discussed later in the paper.

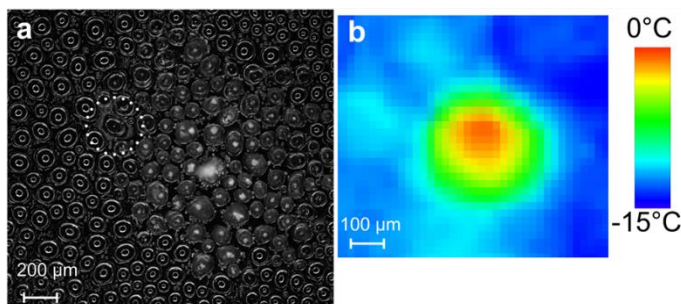


Figure 4.2 Condensation freezing on the bitumen surface. a) optical image of the supercooled water droplets during freezing. The droplet in the white dotted circle is an example of a freezing water droplet. b) Infrared image of a freezing droplet. Due to the released latent heat of fusion at the moment of freezing, the temperature of a supercooled droplet jumps to the equilibrium water freezing temperature of $0\text{ }^{\circ}\text{C}$.

Figure 4.3 shows five selected timeframes of vapor condensation and freezing on virgin bitumen surfaces. Extracted synchronized frames from optical microscopy at temperature steps of $5\text{ }^{\circ}\text{C}$, $-10\text{ }^{\circ}\text{C}$, $-25\text{ }^{\circ}\text{C}$, $-35\text{ }^{\circ}\text{C}$, and $-50\text{ }^{\circ}\text{C}$ at the $-10\text{ }^{\circ}\text{C}/\text{min}$ cooling rate experiments, which started from $25\text{ }^{\circ}\text{C}$ and proceeded until the target temperature of $-50\text{ }^{\circ}\text{C}$ was reached (see Video C.1 in Appendix C for a full sequence of surface frosting). The continuous humidified nitrogen stream provided three relative humidity levels of 20%, 50%, and 80% (at $T_{env} = 21.5 \pm 0.5\text{ }^{\circ}\text{C}$), in Figure 4.3a, Figure 4.3b, and Figure 4.3c, respectively. The ambient relative humidity changes the dew point; therefore, condensation is triggered at a warmer substrate temperature (earlier) in higher RH conditions for the same cooling rate (Figure 4.3b, c). The size of the condensed droplets is larger under higher RH conditions (Figure 4.3b and Figure 4.3c) compared to low relative humidity

DROPSWISE CONDENSATION FREEZING AND
FROSTING ON BITUMINOUS SURFACES AT SUBZERO
TEMPERATURES

conditions, such as a RH of 20% (Figure 4.3a). The dotted area in the $-35\text{ }^{\circ}\text{C}$ temperature panels show the extent of the frozen areas in the field of view. We see that more frost grows faster for higher RH and the freezing temperature is also warmer, and denser frost forms at higher RH conditions after freezing (Figure 4.3, $-50\text{ }^{\circ}\text{C}$ frame panels).

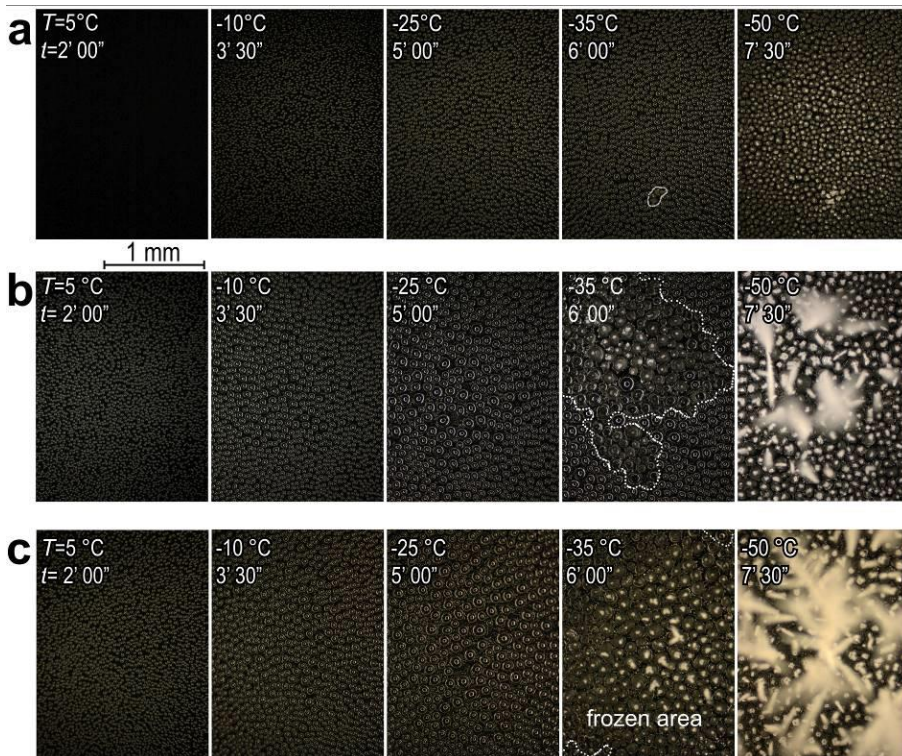


Figure 4.3 Condensation and freezing on the surface of virgin bitumen under different environmental relative humidity (RH) conditions. Five temperature steps of $5\text{ }^{\circ}\text{C}$, $-10\text{ }^{\circ}\text{C}$, $-25\text{ }^{\circ}\text{C}$, $-35\text{ }^{\circ}\text{C}$, $-50\text{ }^{\circ}\text{C}$ (synchronized time steps) at $-10\text{ }^{\circ}\text{C}/\text{min}$ constant cooling rate under three different environmental RH conditions ($T_{\text{env}} = 21.5 \pm 0.5\text{ }^{\circ}\text{C}$) are shown. a) $RH = 20\%$ b) $RH = 50\%$ c) $RH = 80\%$. Dotted regions at $-35\text{ }^{\circ}\text{C}$ panels show the extent of the frozen areas with different degrees of surface frosting: **a**, initiation ($RH\ 20\%$), **b**, partially frozen ($RH\ 50\%$), **c**, mostly frozen ($RH\ 80\%$).

Figure 4.4a, and Figure 4.4b show plots of condensation temperature vs. relative humidity (cooling rate = $-10\text{ }^{\circ}\text{C}/\text{min}$) and condensation temperature vs. cooling rate ($RH = 50\%$), respectively. Figure 4.4c and Figure 4.4d show plots of freezing temperature vs. relative humidity (cooling rate = $-10\text{ }^{\circ}\text{C}/\text{min}$) and freezing temperature vs. cooling rate ($RH = 50\%$), respectively. Figure 4.4a shows that there is a correlation between relative humidity and condensation temperature. However, at the same RH, there is little correlation between cooling rate and condensation temperature, Figure 4.4b. (We do observe that for different cooling rates, with constant $RH = 50\%$, the final volume of the condensed droplets was larger at a slower cooling rate of $-1\text{ }^{\circ}\text{C}/\text{min}$ due to the longer residence time on the cold substrate in comparison to the faster cooling rate of $-20\text{ }^{\circ}\text{C}/\text{min}$, Figure C.9.) We see that as RH increases, for constant cooling rate, so too does the freezing temperature, Figure 4.4c. We attribute this to the fact that under these conditions, more water can condense on the surface of bitumen when the relative humidity is higher, which increases the probability that a supercooled droplet will freeze. (Figure 4.3c and Figure C.9a show that for high relative humidity or low cooling rates, larger droplet-substrate contact diameters were observed just before freezing: ~ 600 to $1600\text{ }\mu\text{m}$; Figure 4.3a and Figure C.9b-c show that for low relative humidity or intermediate or fast cooling rates, droplet-substrate contact diameters were ~ 50 - $60\text{ }\mu\text{m}$, demonstrating the effects that cooling and relative humidity can have on condensed droplet sizes.) We also observe that the freezing temperature decreases with increased cooling rate, Figure 4.4d. We attribute this to the fact that as the surface gets colder faster, it has less time to condense water on it—decreasing the overall volume of supercooled water on the surface—that in turn decreases the likelihood of freezing and therefore reduces the freezing temperature.

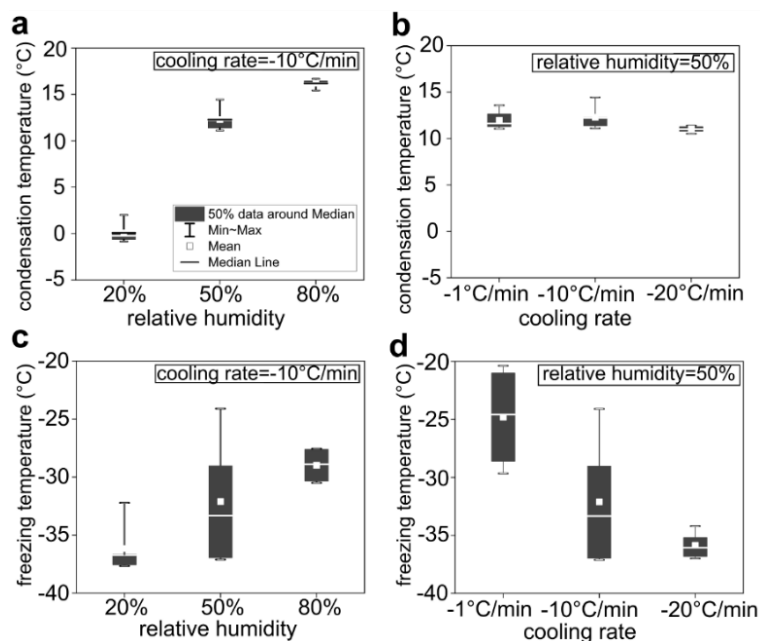


Figure 4.4 Condensation and freezing on the surface of virgin bitumen under different conditions. Initial condensation temperature a) under three RH conditions of 20%, 50%, and 80% at -10 °C/min cooling rate. b) at three cooling rates -1 °C/min, -10 °C/min, and -20 °C/min at RH = 50 %. Initial freezing temperature c) a) under three RH conditions of 20%, 50%, and 80% at -10 °C/min cooling rate. d) at three cooling rates -1 °C/min, -10 °C/min, and -20 °C/min at RH = 50 %. (For all cases, $T_{env} = 21.5 \pm 0.5$ °C).

Figure 4.5a shows portions of three supercooled liquid droplets—one larger, two smaller—on the bitumen substrate, and Figure 4.5b-d illustrates the very interesting phenomenon of “ice bridging”, which manifests itself during freezing on the bituminous surface and is a mechanism facilitating frost spreading^{93,154–156}. Previous work has shown that when a supercooled droplet freezes, it rapidly heats and evaporates, which here results in a condensation deposit, Figure 4.5b⁹³. Depending on the properties of the substrate, this deposit can freeze, forming a frost halo⁹³. If there is a neighboring supercooled droplet, due to the high vapor

pressure above it relative to the frozen droplet (for the same temperature), vapor diffusion can occur, resulting in an ice bridge forming between the frozen and supercooled droplets, Figure 4.5c^{154,155,157}. If the neighboring supercooled droplet is not too far away and is large enough to feed the growing ice bridge, then the ice bridge can form a connection between the two droplets and will cause the supercooled droplet to freeze¹⁵⁶ (see Video C.2 in Appendix C which shows the full ice bridging process on bitumen).

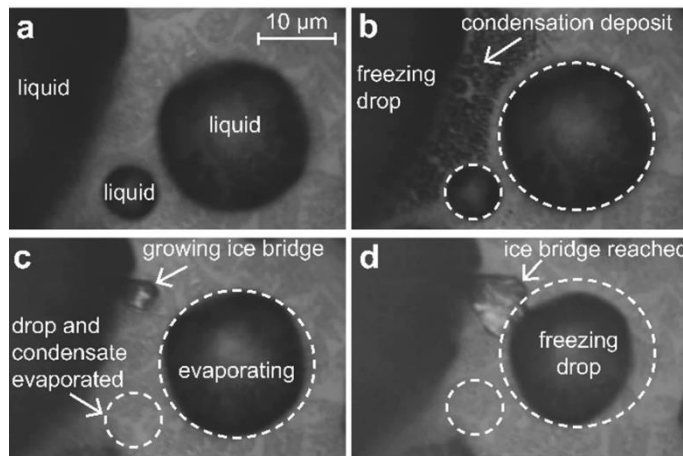


Figure 4.5 Microscopic ice bridging and freezing propagation on bitumen. a) Three supercooled liquid droplets. b) Freezing of the large droplet forms condensation deposits. c) An ice bridge grows while the condensation deposit and the smallest liquid droplet evaporate. d) The ice bridge reaches the medium size drop and freezes it.

To this end, we see that at subzero temperature conditions, suddenly, the large metastable droplet (Figure 4.5a) suddenly freezes (Figure 4.5b) with the mechanism discussed earlier. The simultaneously released latent heat is a practically adiabatic process (no heat losses within this very short time frame)⁹³. This increases the droplet temperature to the equilibrium freezing temperature of 0 °C, making it significantly warmer than its environment and causing flash evaporation from the

freezing droplet surface^{84,93}. The so-generated excess vapor radially diffuses outward and subsequently condenses around the freezing droplet, forming a condensation deposit (Figure 4.5b)⁹³. The condensation occurs in the form of isolated supercooled micron-sized droplets, which are visible in the optical microscope results, Figure 4.5b. Local vapor pressure gradients, substrate temperature, wettability, and substrate thermal conductivity govern the state of the condensation, whether or not this condensate deposit freezes, and desublimation around the frozen droplet⁹³ occurs. During the second slower stage of freezing (inner droplet freezing front propagation is not shown), whose rate is controlled by a balance of heat removal from the droplet into the substrate and latent heat of fusion, the droplet further solidifies. As a result of the droplet interface becoming ice and also eventually cooling, the evaporation rate also decreases⁹³. Afterwards, in the vicinity of the freezing droplet, the local relative humidity gradually declines until it is locally in equilibrium with the ice. The vapor pressure above the ice is lower than that above supercooled water at the same temperature conditions. As a result, if there are supercooled droplets near the fully solidified droplet, the latter will act as a humidity sink to the former, causing evaporation. Hence, condensate droplets on the surface can evaporate and disappear altogether, Figure 4.5c. Such vapor emitted from liquid evaporating/evaporated droplets can diffuse toward an adjacent ice droplet, deposit, and facilitate the formation and growth of an ice bridge, starting at the base of the larger frozen droplet, Figure 4.5c. The ice bridge can act as freezing initiator for any neighboring supercooled liquid droplet that it can reach, Figure 4.5d, leading to ice propagation and frost formation^{155,156}. We see

that the liquid droplet freezes as soon as the ice bridge connects, triggering the next iteration of bridging towards another liquid droplet, Figure 4.5d.

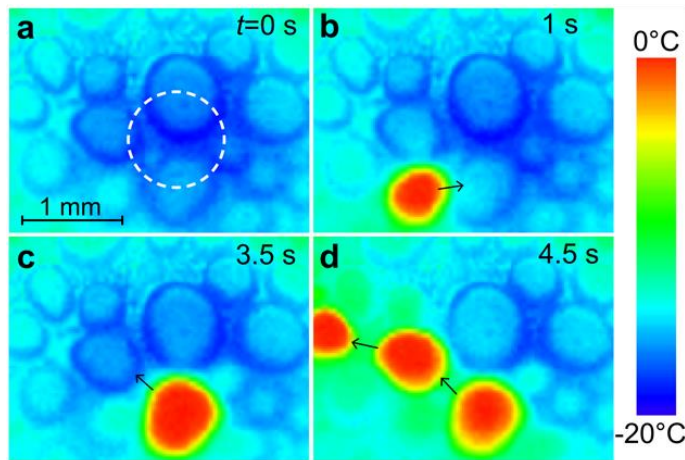


Figure 4.6 Thermal imaging of recalescence and cascade freezing. a) Condensed supercooled water droplets on bitumen. The white dotted line shows the location of the cooling pin below the bituminous layer. b) Rapid release of latent heat of fusion during supercooled droplet freezing causes the droplet temperature to increase to the equilibrium value. c-d) Ice bridging or freezing of the condensate deposit, as discussed in Figure 4.5, results in neighboring droplet freezing and “cascade freezing”. Arrows show the direction of a cascading freezing event.

Figure 4.6a shows supercooled water droplets on bitumen before freezing (the dashed line shows the location of the cold pin). The latent heat that is released due to freezing raises the temperature of the supercooled droplets to their equilibrium freezing temperature, 0 °C (Figure 4.6b-d). The evaporation rate of the droplet and the vapor pressure above it increases as a consequence. Eventually, the remaining surrounding supercooled droplets freeze. As discussed earlier, a plausible mechanism of the observed cascade freezing is ice bridging (Figure 4.5). Additional mechanisms have also been discussed in literature ¹⁵⁸. Finally, the frozen area spreads, and frost covers the entire surface. (See also Figure C.8 in Appendix C for

a microscopic image sequence showing recalescence and freezing propagation and also the related Video C.3 in Appendix C.)

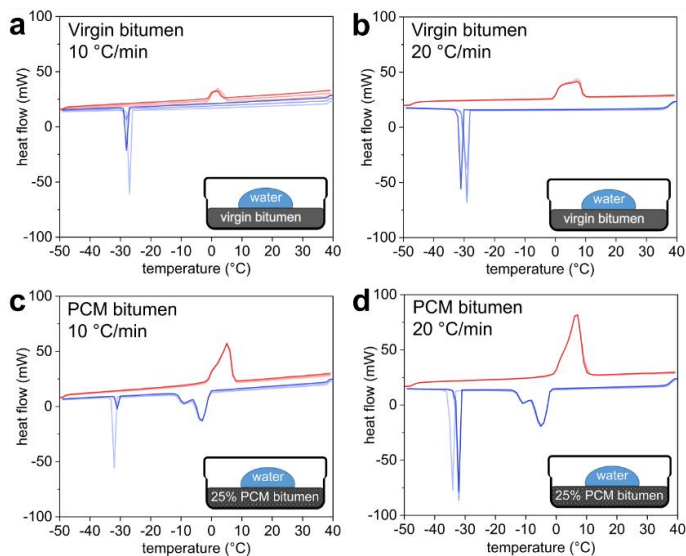


Figure 4.7 DSC analysis of the virgin and modified bitumen when in contact with a 1 μl water droplet (positive heat flow indicates an endothermic process). a) Virgin bitumen at 10 $^{\circ}\text{C}/\text{min}$ rate, b) virgin bitumen at 20 $^{\circ}\text{C}/\text{min}$ rate, c) 25 wt.% PCM modified bitumen at 10 $^{\circ}\text{C}/\text{min}$ rate, and d) 25 wt.% PCM modified bitumen at 20 $^{\circ}\text{C}/\text{min}$ rate. Each plot has three heating and cooling cycles.

Based on the above, we have determined the environmental conditions under which condensed droplets form and freeze on bitumen. We now aim to use this knowledge and rationally select and embed a phase change material in bitumen and study supercooled droplet freezing behavior and how this could be affected by this modification. For this, we first studied the natural thermal properties of virgin bitumen in contact with water droplets, which is shown by the DSC measurements in Figure 4.7a, b (see also Figure C.6a). Here we see that over this temperature range

(-50 to 40 °C), the thermal properties of water dominate that of bitumen. (The exotherm and endotherm are attributed to supercooled water freezing and ice melting, respectively.) To alter the freezing behavior of water on bitumen, we opt to add PCM—with a melting temperature near the melting point of water—to bitumen in order to produce a heating effect, targeting the retardation of icing and aiding the significant heating effect from the latent heat of the water. Here we study the effect of embedded PCM microcapsules in virgin bitumen—at a concentration where it does not significantly alter the desirable mechanical properties of it (25 wt.%)¹⁴⁷—which we find can actively release heat over the temperature range of 1 °C to -20 °C, depending on the cooling rate (Figure 4.7c, d, see also Figure C.6b, in Appendix C).

Despite the nature of metastable subcooled PCM material before crystallization, in the case of rapid PCM cooling (-20 °C/min), the crystallization activation of the PCM started at about the same temperature as the intermediate cooling (-10 °C/min), but the active temperature range—where the PCM still releases heat—depends on the time duration. Therefore, according to the cooling rates, the convoluted time durations on the temperature axis of the DSC results should be noted. (The measured PCM fusion peak temperature values are in the range of the -4 ± 3 °C; see Figure C.6b and Figure 4.7.) Kakar et al.¹⁴⁷ showed for the same PCM microencapsulated modified bitumen that we used here, the cold temperature mechanical performance of the material was improved by embedding 25 wt.% PCM in bitumen. Moreover, it has also been shown that this PCM microcapsule remains stable in the bitumen mixture without agglomeration¹⁴⁷. The DSC analysis detected water freezing latent heat release of 17 ± 9 J/g on both modified and virgin bitumen, while the PCM heat of fusion at 25 wt.%

concentration is 48 ± 3 J/g, Figure 4.7c, d. It is noted that the freezing temperature of a $1 \mu\text{l}$ water droplet on PCM modified bitumen is up to $\sim 7^\circ\text{C}$ lower compared to a water droplet freezing on control virgin bitumen specimens. We attribute this difference to the fact that the PCM releases a significant amount of heat, warming the droplet, meaning that the system is not isothermal and has to cool itself more in order to trigger supercooled droplet freezing.

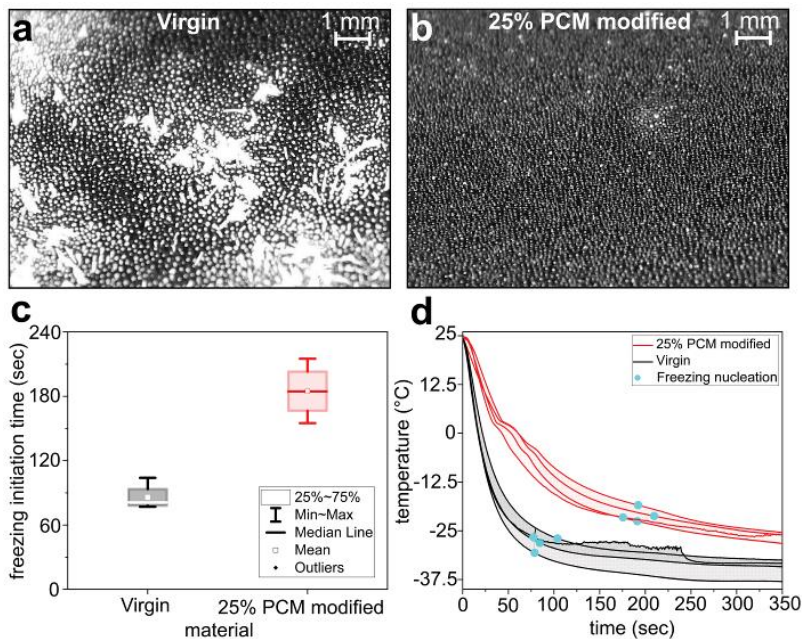


Figure 4.8 PCM can delay freezing on bitumen. Bitumen surfaces after 3 minutes cooling at the same constant cooling flux condition from 25°C for two material states of a) Virgin. b) 25 wt.% PCM-modified bitumen. c) Freezing initiation time on a bitumen surface plotted for virgin and 25 wt.% PCM-modified bitumen in black and red colors, respectively. d) Bitumen surface temperature measured by IR camera plotted for virgin and 25 wt.% PCM-modified bitumen in black and red colors, respectively. PCM activation occurs gradually as the cooling is done from the bottom of the bitumen. This manifests itself into a kink in the temperature profile of the surface temperature once the PCM effect

reaches the surface. Initial freezing nucleation temperatures are marked with blue circle symbols.

Figure 4.8a, b show the difference in frost development after 3 minutes of constant flux cooling on the virgin bitumen and the PCM-modified bitumen, respectively. Different degrees of frost formation and condensation indicate that there are differences in substrate temperature at the same environmental conditions. Analyzing the optical and infrared results of both surfaces shows that condensed water requires almost twice as long to freeze on the PCM-bitumen composite compared to the virgin bitumen at the same cooling and environmental conditions (Figure 4.8c). This means that the latent heat of fusion from the PCM microcapsules can delay the freezing of water on the bitumen surface. IR surface temperature measurements reveal that the bitumen containing PCM cools at a slower rate and has a significant effect on the surface temperature of bitumen, Figure 4.8d. PCM activation occurs gradually as the cooling is done from the bottom of the bitumen, manifesting itself as a kink in the temperature profile of the surface temperature once the PCM effect reaches the surface. The IR surface temperature history plots show that eventually, even after releasing all stored PCM heat, the surface temperature of modified bitumen remained at least 10 °C warmer at similar time steps compared to control virgin bitumen sample temperature at -30 °C, Figure 4.8d. We also see that the modified bitumen surface remains warmer even after freezing has initiated, which has implications for subsequent ice removal, as ice is known to adhere stronger to substrates at colder temperatures compared to warmer ones¹⁵⁹. We note that in many applications, the surface of bitumen may be contaminated—affecting and possibly promoting condensation nucleation and freezing—and that the present approach, which is based on embedding PCMs to

enhance surface heating and nucleation delay should also work to delay freezing under such challenging real-world conditions since it is based upon the bulk modification of bitumen and not the surface alone.

4.5 Conclusion

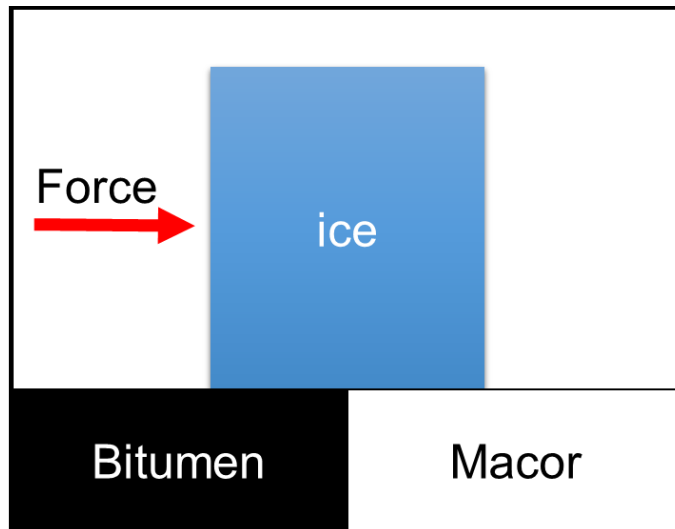
The complex process of condensation and freezing of water on bituminous materials was investigated. It was found that the initial temperature at which condensation initiated is highly dependent on the relative humidity and the available vapor above the cold surface. Different substrate cooling rates have a minor effect on the initial condensation temperature. However, for slow cooling rates, where bitumen remains exposed to colder temperatures for a longer period of time, water upon it freezes at relatively higher subzero temperatures. At the moment of freezing, the released latent heat causes the temperature of the supercooled droplets to jump to 0 °C, the equilibrium freezing temperature, causing local heating and evaporation. Subsequent local condensation of this vapor and its freezing among droplets initiates an interesting phenomenon of ice bridging and frost propagation, which we reveal with optical microscopy and high-speed infrared imaging. Embedding PCM microcapsules with a melting temperature close to that of water and at 25 wt.% in bitumen—a concentration that does not significantly alter mechanical properties—can markedly delay supercooled water freezing and frost formation. It is experimentally shown in the designed experimental condition and 25 wt.% concentration of the PCM microcapsules in bitumen, that the average freezing time shifts from about 85 seconds on virgin bitumen to about 185 seconds on PCM modified bitumen. This effect can postpone freezing incidence in constant

heat flux cooling and maintain ice-free bitumen surfaces. As discussed earlier, previous research has shown that the microcapsules can stay intact during the fabrication of asphalt concrete, as long as this is the case, the effect of PCM's is repeated through the melting and crystallization cycle dictated by the natural temperature fluctuations. Future research could focus on in situ performance of such novel additives.

4.6 Acknowledgments

Financial support of the Swiss National Science Foundation under grant number 200020_169122 / 1 and the European Research Council under Advanced Grant 669908 (INTICE) are acknowledged. Beatrice Fischer of Empa is acknowledged for performing the DSC measurements.

5 ICE ADHESION BEHAVIOR OF HETEROGENEOUS BITUMINOUS SURFACES



This chapter is published as:

Tarpoudi Baheri, F.; Poulikakos, L. D.; Poulikakos, D.; Schutzius, T. M. Ice Adhesion Behavior of Heterogeneous Bituminous Surfaces. *Journal of Cold Regions Science and Technology*, 192, 103405, (2021). <https://doi.org/10.1016/j.coldregions.2021.103405>.

5.1 Abstract

The phenomenon of icing, and the derived processes for its mitigation, are of great importance in many applications, ranging from transportation and energy to food and refrigeration. This phenomenon has been studied mostly with respect to its manifestation on rigid, homogeneous surfaces, with soft materials being the topic of more recent investigations. Although, icing often occurs on substrates that are chemically and mechanically heterogeneous, e.g., widely used asphalt concrete, which consists of rigid aggregates embedded in soft bitumen, to date, ice adhesion behavior on such substrates needs to be better understood. Here, we study ice adhesion stresses—the stresses necessary to remove ice—of ice blocks on heterogeneous materials, juxtaposing the behavior of the two main constituents of asphalt concrete, the rigid aggregates (modeled by Macor®) and bitumen, to the behavior of bitumen-Macor® composites. We show that the ice adhesion shear stress on Macor® is almost twice as large as that on bitumen, whereas the ice adhesion normal stress and the normal and shear components of composite stress are in a similar range. We synthesize composite substrates that consist of bitumen stripes on Macor® and find that increasing bitumen width leads to lower ice adhesion stress, while the stripe direction with respect to the applied force direction has a minor effect. Based on our findings, we then coat the most ice-adhesive component (Macor®) with a thin superhydrophobic coating and show that this can reduce ice adhesion stress on the heterogeneous substrates. We also find that for ice formed half on bitumen and half on Macor®, if Macor® is first and bitumen second with respect to the applied force direction (material order), then the measured ice adhesion stress is less compared to the reverse case in material order.

5.2 Introduction

Despite its common manifestation on roads, roofs, terraces, and sidewalks in cold climates, the fundamental issue of surface icing—and passive methods to prevent it and facilitate its removal—is not well understood. This includes condensation freezing on roads and, consequentially, attempting to prevent or delay ice formation, as well as investigating facile removal principles of frozen or snow-covered pavements, leading to the introduction of methods to reduce the stress needed to remove ice (termed here as ice adhesion stress) and facilitate ice removal. Road surfaces consist of two main components: Rigid aggregates (gravel), which are held together by a soft viscoelastic bituminous binder. They have drastically different wettability and stiffness properties, causing road surfaces to be both chemically and mechanically heterogeneous.

To date, research on ice adhesion mechanisms has focused on rigid materials^{95,160–163}, proposing textured low-surface energy coatings possessing low ice adhesion stress⁷². Liquid-infused (i.e., lubricated) surface technology has attempted to take advantage of embedded liquid interface properties in solid structures to reduce ice adhesion stresses^{80,164–166}. It is shown that the rigid phase arrangement and area fraction of the liquid-infused surface can control ice adhesion by governing local conductive heat transfer, ice-substrate interaction, and locally cracking initiation of the iced interface^{165,166}. Recently, the impact of substrate compliance on ice adhesion stress has attracted researchers' attention, and a number of studies have been undertaken on this topic^{167–173}. Petit *et. al.* have shown that substrate compliance does not have a significant role on freezing initiation time while later the substrate deformation influences interfacial area and consequently freezing

process is faster on softer substrates¹⁶⁷. Applied force on frozen interfaces can form surface instabilities and fringes, depending on the soft substrate thickness and the neighboring material properties, whether soft or rigid^{168,169}. It has been shown that a rigid object on a compliant substrate slides in shear mode unless the developing normal force (at the location of the applied force) reaches a critical value and detaches the interfaces of the rigid object and soft substrate¹⁷⁰. Despite the brittle ice removal from rigid materials, it is shown that ice detaches from soft surfaces in a dynamic stick-slip motion i.e., intermittent movement with recurring cycles of stationary and sliding phases¹⁷². Furthermore, for long enough ice blocks, ice adhesion could become independent of the ice area which results in very low ice adhesion stresses for large area ice-soft material interfaces¹⁷³.

While the behavior of ice on homogeneous surfaces is understood to a degree, the fundamentals of ice formation and adhesion on heterogeneous substrates—for both wettability and stiffness—are not, and relatively few studies have been conducted on this topic^{174–176}. Liu *et al.* showed that substrate hydrophobic-hydrophilic boundaries can block the ice-substrate front and alter the ice growth mode transition when the wettability of the solid substrate changes¹⁷⁴. Irajizad *et al.* measured ice adhesion stresses on heterogeneous materials—a low shear modulus material dispersed in a high shear modulus matrix—and showed that stress mismatch of ice interface with heterogeneous substrate can reduce ice adhesion stress¹⁷⁵. Once a minimal force is applied (resulting in approximately 1 kPa), ice detaches from the low shear modulus material phase and forms cavities at the interface of the substrate material and ice, leading to a stress concentration around the cavity and inducing crack and cavity growth and fracture of interfaces¹⁷⁵. Experiments performed on patterned rigid-soft substrates of aluminum-

polyurethane have shown that by increasing the area fraction percentage of the softer component (stripes from 2mm width to 10 mm, respecting 0% to 77% for 26 mm square samples), the ice adhesion is reduced independently of the substrate heterogeneity direction (stripes in the aluminum filled of the softer polyurethane phase) on the anisotropic substrate ¹⁷⁶.

Several ice adhesion studies have been conducted specifically on road surfaces, mostly focusing on practical applications ^{29,31,32,177–181}. It is shown that regardless of the bulk water or ambient conditions a layer of small, bubble-free ice crystals nucleate on the pavement surface once its temperature drops below subzero ¹⁸². However, this layer is strong and well adhered but if the nucleation could be prevented using either salt or changing the substrate surface energy, ice adhesion would be weaker due to larger ice crystals inner bulk water and entrapped bubbles ¹⁸². Peng *et al.* showed that replacing asphalt concrete fillers with anti-freezing salt-based components and fumed silica-based coating can delay freezing and significantly reduce the ice adhesion stress ³². Arabzadeh *et al.* showed that spraying superhydrophobic coatings on asphalt surfaces can also reduce ice adhesion stress ^{31,181}. By lowering the substrate asphalt concrete temperature from 0 °C to -10 °C, cohesive failure in ice becomes dominant compared to adhesive failure at the interface ¹⁷⁸. In large-scale asphalt concrete samples, Dan *et al.* found that the normal-tension ice adhesion depends logarithmically on the ice temperature, whereas in the case of the shear stress, a linear relation was exhibited ¹⁷⁷.

In this study, we investigate the fundamentals of ice adhesion stress on heterogeneous bituminous surfaces at smaller sub-centimeter scales. To this end, at sample surface temperature of $T_2 = -19.5 \pm 0.5$ °C, the impact of substrate

mechanical and chemical heterogeneity on ice adhesion stress is studied by juxtaposing soft viscoelastic bitumen next to rigid glass-ceramic aggregates that we model by Macor®. We synthesize heterogeneous substrates that consist of bitumen stripes on Macor® and find that increasing stripe width—for the same ice block size—leads to lower ice adhesion stress. We also find that the stripe direction with respect to the applied force direction does not have a pronounced effect on ice adhesion stress. Based on these findings, we then focus on modifying Macor®, the most adhesive component of the heterogeneous substrate, and to this end, we exploit an up-scalable, superhydrophobic, durable coating technique. We confirm that a superhydrophobic coating can significantly reduce the ice adhesion stress on Macor®. We also find that for ice blocks that are half on the bitumen stripe and half on Macor® (also superhydrophobic Macor®), if the rigid Macor® is first and softer bitumen second with respect to the applied force direction, then the measured ice adhesion stress is less compared to the reverse case. Our findings add to necessary fundamental knowledge contributing to the design of bituminous surfaces with facile ice removal behavior, paves the path for further studies in the future.

5.3 Methods and Material Studied

5.3.1 MATERIALS

Figure 5.1a shows a schematic of an ice block on a heterogeneous bituminous surface consisting of rigid Macor® (white) and soft bitumen (black), with the applied force for the removal of this block shown with the red arrow. The material used for the soft component was virgin bitumen Q8 70/100 with penetration grade

70/100, density 1.029 g/cm³ of Middle Eastern origin with a medium softness range of 82 (0.1 mm) needle penetration (EN 1426), and softening temperature (EN 1427) of 45.8 °C, and dynamic viscosity of 163 Pa-s at 60 °C. For this type of bitumen, differential scanning calorimetry (DSC) results indicated that its glass transition temperature is ca. -20 °C and that it has a melting peak at ca. 28 °C. The reported SARA (saturates, aromatics, resins, and asphaltene) fractions of this bitumen type are 3.8, 59.6, 22.2, and 14.6 %, respectively^{47,130}. SARA analysis is an operational method to separate the bitumen into its characteristic finite fractions according to the polarity, molar mass and aromatic content of the molecules⁴⁰. Figure 5.1b, and c show the significant mechanical and wetting behavior differences, relevant to ice adhesion, between the employed bitumen and Macor®. Bitumen is a temperature- and frequency-dependent viscoelastic material with a complex modulus, G , of 0.15 MPa at 20 °C and 81 MPa at -10 °C under 0.1 Hz, 10 % strain, shown in Figure 5.1b (see also Figure D1). Aggregates have random shapes and uncontrolled surface properties; therefore, we used Macor® as a representative material for asphalt concrete aggregates. Macor® has a complex modulus of 25.5 GPa over the experimental temperature range of this study, Figure 5.1b. The surface of bitumen is generally hydrophobic with an advancing contact angle of > 110° and a receding contact angle of ca. 75°, Figure 5.1c. On the other hand, Macor® is superhydrophilic and has a receding angle of < 5°, Figure 5.1c.

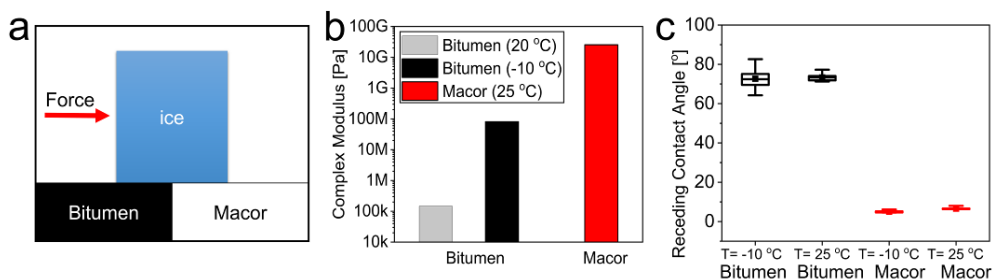


Figure 5.1 Ice adhesion on road-like materials at subzero temperatures. a) General schematic of ice formation on heterogeneous road-like surfaces. b) Complex modulus of bitumen at 20 °C and -10 °C at 0.1 Hz versus reported complex modulus of Macor® material at 25 °C¹⁸³. c) Receding contact angle of a water droplet on bitumen surface and Macor® at two sample temperatures of 25 °C and -10 °C and environmental condition of $RH < 1\%$ at 24 ± 1 °C.

Such high contact angle hysteresis on bitumen could be due to surface tension driven substrate deformation—due to its softness at room temperature—at the triple contact line, as has been shown for other soft substrates^{184–186}. Furthermore, previous work has shown that the surface of bitumen is complex, possessing heterogeneous surface chemistry and intrinsic roughness that potentially can affect contact angle hysteresis¹⁸⁷. Macor®, on the other hand, is a machinable glass-ceramic with similar properties to common aggregates such as limestone, basalt, and sandstone, and its hydrophilic property is to be expected, Table 5.1. Measurements shows that the studied Macor® has microscale surface roughness with average RMS roughness of 0.34 ± 0.04 μm (see Figure D2 and Figure D3) whereas reported average roughness RSM the commonly in the order of tens of micros^{188,189}. Based on the above, one should anticipate differences, with respect to ice adhesion, between the behavior of such a composite material and the case where the surface consists one of those materials, acting alone.

Table 5.1 **Properties of commonly used asphalt concrete aggregates and Macor® material at 25 °C**¹⁸³. Where values of, thermal conductivity (K), specific heat (C_p), density (ρ), apparent contact angle θ^* , and complex modulus (G) are reported.

	Thermal conductivity K ($\text{W}\cdot\text{m}^{-1}\cdot\text{K}^{-1}$)	Specific heat C_p ($\text{J}\cdot\text{kg}^{-1}\cdot\text{K}^{-1}$)	Density ρ ($\text{kg}\cdot\text{m}^{-3}$)	Contact angle θ^* (deg)	Complex modulus G (GPa)
Macor®	1.46	790	2520	Advancing: 28 ± 2 Receding: < 5	25.5
Basalt	1.7	840	2400-3100	74 ± 5	50
Limestone	1.26-3.0	909	2700	-	3-27
Sandstone	1.7-3.0	710-900	2850	-	10-20

5.3.2 SUBSTRATES AND COATINGS

To fabricate thin virgin bitumen coatings on a Macor® substrate—and also to create stripes of bitumen in Macor® notches—we used a solvent casting approach. To prepare the bitumen solution, 1 g of virgin bitumen was diluted in 4 ml toluene (Sigma-Aldrich 99.8%) at room temperature (ca. 25 °C) and mixed using a shaker (Heidolph Multi Reax) at 2,000 rpm for 2 minutes. A drop of 150 μl virgin bitumen solution was then dispensed on Macor® disks (1 mm thick, 18 mm diameter). The solvent cast sample was left under a fume hood in ambient conditions until most of the toluene solvent evaporated, which was observed to occur within half an hour. Next, samples were heated on a hotplate at 115 °C for five minutes, above the bitumen softening temperature of 45.8 °C and the toluene boiling temperature of 111 °C, to ensure uniform and smooth surfaces. Thereafter, the samples were placed in a refrigerator for five minutes at 4 ± 2 °C to cool and

solidify the bitumen coating layer. The final bitumen thickness was measured to be $\approx 225 \mu\text{m}$ (see also Figure D4a).

To create superhydrophobic surfaces on Macor[®], we deposited polymer-nanoparticle dispersions onto it by spray coating following a previously published method¹⁹⁰. The coating thickness was ca. $25 \mu\text{m}$ (see also Figure D4b). To prepare the dispersion for spray, we first made two stock solutions and a nanoparticle suspension. The first stock solution consisted of 10 wt.% PVDF (polyvinylidene fluoride) in NMP (N-Methyl-2-pyrrolidone) and was generated by adding PVDF to NMP and then mixing it slowly for 5 hours at 40 °C. The second stock solution consisted of 10 wt.% PMMA (poly(methyl methacrylate)) in acetone and was generated by combining PMMA beads with acetone and mixing it at 1200 rpm for 8 hours. The nanoparticle suspension consisted of 10 wt.% hydrophobic fumed silica (HFS; Aerosil R 8200, Evonik Industries) in acetone and was created by combining HFS and acetone and probe sonicating it for 30 seconds (130 W, 3 mm probe, 50% amplitude, 20 kHz frequency, Sonics Vibracell, VCX-130). One portion of each of the two solutions and ten portions of suspension were then combined and diluted with additional ten portion of acetone, resulting in a final 12 g mixture (for 0.5 g portions) can approximately coat an area of 25 cm^2 . To create stripes of bitumen on Macor[®], 200 μm deep notches were cut into the Macor[®] surface, with widths of either 0.5, 1, or 1.8 mm, and then they were filled with the bitumen-toluene solution (~ 22 wt.%, 1 gr bitumen in 4 μl toluene). The ice mold that we use to measure ice adhesion is a tube that has an inner diameter (ID) of 1.8 mm, so these bitumen stripe widths of 0.5, 1, and 1.8 mm correspond to ice-bitumen contact area fractions of $\phi = 35\%$, 67% , and 100% (experiments described

in detail later). We used pure Macor® surfaces ($\phi = 0\%$ bitumen-ice contact area) as control samples.

5.3.3 CHARACTERIZATION

We used a commercial goniometer (OCA35, DataPhysics Instruments GmbH) to perform contact angle measurements in sessile mode contact angle at $0.5 \mu\text{l/s}$ dosing rate with final droplet volume of $10 \mu\text{l}$. A homemade environmental chamber was installed on the goniometer stage for contact angle measurements in order to control sample temperature and environment relative humidity (RH) conditions (see Figure D5). The inlet nitrogen stream at room temperature provided $RH < 1\%$. The contact angle measurements were conducted at two sample temperatures of $25 \text{ }^\circ\text{C}$ and $-10 \text{ }^\circ\text{C}$, controlled by a thermoelectric element. Commercial software was used for contact angle post-processing (DataPhysics Instruments GmbH).

We performed ice adhesion in three modes of *pure shear stress* (applied force parallel and tangential to the substrate), *combined stress* (applied force at a finite height from the substrate and parallel to it), and *normal-tension stress* (force perpendicular to the substrate). The ice adhesion setup comprised four main elements (see Figure D6a, and b). A commercial cryogenic system was used as the cooling stage to cool the substrates to subzero temperatures (BSC 196 from Linkam Scientific Instruments Ltd.). The stage temperature was set to $-24.5 \text{ }^\circ\text{C}$, and the surface temperature was measured $T_2 = -19.5 \pm 0.5 \text{ }^\circ\text{C}$ by a T-type thermocouple. A copper plate was designed and installed on the cold stage for mounting and holding samples firmly. At least 20 minutes of conditioning time was considered after cooling the stage from room condition to the target temperature at $-20 \text{ }^\circ\text{C}/\text{min}$ to

ensure the water column was frozen on the sample. An environmental chamber was built from transparent Plexiglas® and mounted on top of the cryogenic stage to control humidity and prevent condensation and frosting on the sample. Inlet N₂ gas guarantees dry environmental condensation to prevent frost formation on the surfaces. Over the conditioning time before conducting the ice adhesion stress measurement experiments, environmental conditions stabilize at $T_1 = 13 \pm 1$ °C and $RH < 1\%$ and environmental temperature of 24 ± 1 °C.

A force sensor (Mark-10 model M5-5) was connected to a rod to induce force while measuring the ice adhesion force for a given ice contact area. An opening at the chamber wall was used as an access point for the force sensor rod. A pointed head was installed on the rod for the pure shear and combined stress ice adhesion tests to push 9 mm tall ice mold made of hard plastic (polystyrene) cylinders with an inner diameter of $D_i = 1.8$ mm and an outer diameter $D_o = 3$ mm. Initially, the empty ice molds were gently placed on the sample surface and then filled with deionized water up to 8 mm in height from the bottom. The height of the tip of the rod from the sample surface (h) was set to zero for the *pure shear mode* (Figure D6a). For combined stress, a force was applied parallel to the substrate surface at the center-of-mass of the ice ($h = 4$ mm). For the normal-tension mode, a triangular ring was attached to the same size ice molds. The force rod was mounted on top of the ice cylinder and connected to it by a hook, and the force was applied away from and normal to the substrate surface.

The force sensor was installed on linear stage (NRT150/M, Thorlabs, Inc.), and the height (h) was adjusted by a lab jack (L490/M, Thorlabs, Inc.), according to the required experimental modes. All ice adhesion experiments were conducted by induced force from a rod starting from a stationary mode with an acceleration

of $a = 0.01 \text{ mm/s}^2$, far enough to reach the constant velocity of $V = 0.1 \text{ mm/s}$ steady-state velocity condition at contact. This velocity was selected based on commonly reported and recommended values in other similar ice adhesion experiments^{72,191,192}.

Samples were placed in configuration to accommodate two bitumen stripe directions, resulting in a perpendicular force and the other to result in a parallel force with respect to the notch. For the composite bitumen-Macor® samples, the circular ice mold was placed on the bitumen stripe so that the stripe was in the middle of the ice cross-sectional area. Despite the directional independence of samples in the normal-tension ice adhesion mode, these samples were installed in a perpendicular direction as defined before (Figure D8a). To compare mean value differences between each set of data for different ice adhesion tests on heterogeneous materials, we conducted a statistical two-sampled, two-sided Student's t-test and determined the probability (P) associated with a Student's paired-test.

In the configuration where the ice mold cross-sectional area was placed on the bitumen-Macor® boundary where the bitumen stripe width was 1.8 mm so that half of the ice area was in contact with the bitumen and the other half was in contact with the Macor® ceramic (Figure D8b). For two ice adhesion modes of pure shear stress and combined stress, the impact of the material order was examined with respect to the applied force, which was parallel to the substrate surface.

5.4 Results and Analysis

First, we show the results of the ice adhesion experiments on homogeneous Macor® and virgin bitumen. Figure 5.2a-c depicts a schematic drawing of the ice

adhesion experimental setup in three different modes: pure shear stress, combined stress, and normal-tension stress, respectively. Figure 5.2d-f show plots of the experimentally measured force vs. time in these three different modes on bitumen and Macor® substrates; the maximum magnitude of the force required to remove ice from the substrate, F^* , measured during these experiments were used to calculate the ice adhesion stress along with the ice-substrate contact area. The combined stress mode has a lower F^* due to the torque generated by force acting at the bottom corner of the mold. Figure 5.2g-i shows ice adhesion stresses based on F^* on bitumen and Macor®, for the three modes of pure shear (τ_{shear}^*), combined stress (τ_{cs}^* , and σ_{cs}^*), and normal-tension (σ_{normal}^*). We calculate the pure shear ice adhesion stress by $\tau_{\text{shear}}^* = 4F^*/(\pi D_i^2)$, the combined ice adhesion stress by $\tau_{\text{cs}}^* = 4F^*/(\pi D_i^2)$ and $\sigma_{\text{cs}}^* = 8hF^*/(\pi D_i^3)$, and the normal ice adhesion stress by $\sigma_{\text{normal}}^* = -4F^*/(\pi D_i^2)$.

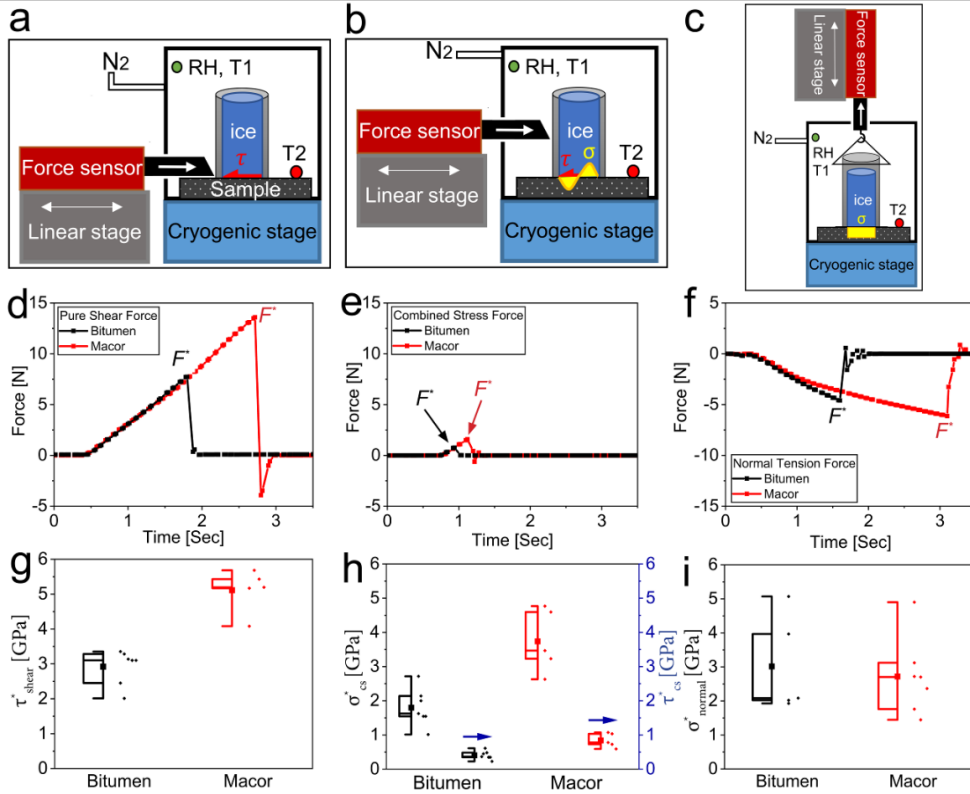


Figure 5.2 Ice adhesion modes on heterogeneous bitumen. Schematic drawing of experimental modes to measure a) pure shear stress b) combined stress, and c) normal-tension stress. Examples of experimentally measured force curves vs. time for d) pure shear stress, e) combined stress, and f) normal-tension stress ice adhesion modes. Calculated stresses based on absolute peak force F^* defined in (d) (e) or (f) are plotted in the box plot (left) and data points (right) for three modes of g) pure shear (τ_{shear}^*), h) combined stresses (σ_{cs}^* and τ_{cs}^*), and i) normal-tension (σ_{normal}^*) plotted for the absolute tensile force value. Each data point represents an experiment of ice adhesion stress measurement.

F^* was higher on Macor® in all investigated modes compared to bitumen. Also, such force vs. time plots are consistent with a brittle breakage behavior, as the force values drop rapidly after the peak, especially for the pure shear and normal-tension modes. For the combined stress ice adhesion measurements, σ_{cs}^* is significantly

greater than τ_{cs}^* , indicating that normal stresses dominate. This is due to the mathematical correlation $\sigma_{cs}^*/\tau_{cs}^* = 2h/D_i$ depending on of h and D_i values. The value of τ_{shear}^* as well as τ_{cs}^* and σ_{cs}^* on Macor® are approximately twice the corresponding values on the bitumen substrate alone (Figure 5.2g, and h). From this, we see that ice adheres stronger to Macor® relative to bitumen. In contrast, the value of σ_{normal}^* on bitumen and Macor® shows higher data scattering (Figure 5.2i). This can be explained by Kendall's theory describing removal of a rigid object from an elastomer in tensile mode. Based on this theory, the tensile modulus is three times higher than the shear modulus^{193,194}. Here we assume that viscoelastic bitumen is primarily elastic in cold temperatures, which explains the fact that primarily tensile failure was seen.

Using heterogeneous bituminous surfaces that consist of a bitumen stripe on Macor®, Figure 5.3a shows plots of τ_{shear}^* vs. the bitumen-ice contact area fraction, ϕ . ϕ was varied by varying the stripe width while keeping the ice-substrate contact area the same. The direction of the bitumen stripe along its long length is perpendicular to the applied force for four bitumen-ice surface fractions ($\phi = 0\%$, 35%, 67%, and 100%). Figure 5.3b shows a plot of τ_{shear}^* vs. ϕ for the configuration where the stripe direction along its long length is parallel to the applied force direction. Results of the probability (P), associated with a Student's paired T-test, with a two-tailed distribution, are shown for each pair of samples only when the difference between two groups is significant (i.e. $P < 0.05$) by red lines.

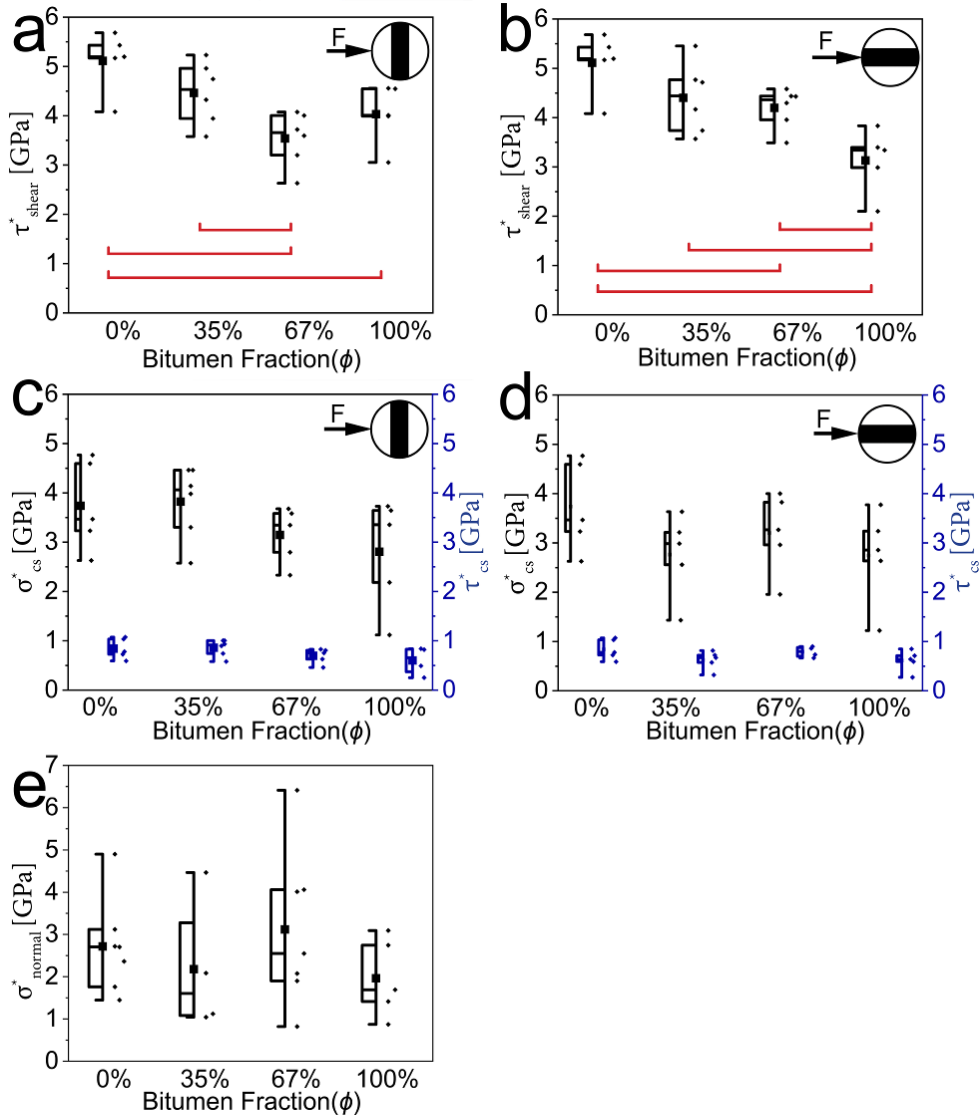


Figure 5.3 Impact of substrate heterogeneity and anisotropy on ice adhesion.

Results are shown for four bitumen-ice area fractions of $\phi = 0\%$ (i.e., pure Macor®), 35%, 67%, and 100%. Samples were installed in two selective stripe directions—defined as the direction along the long length of the stripe—namely, perpendicular and parallel to the applied force. Plots of τ^*_{shear} vs. ϕ for a) perpendicular and b) parallel applied force directions; results of probability associated with a Student's paired T-test, with a two-tailed

distribution, are shown by red lines only for each pair of samples only when the difference between two groups is significant (i.e. $P < 0.05$). Plots of σ_{cs}^* and τ_{cs}^* vs. ϕ for c) perpendicular and d) parallel applied force directions. e) Plot of σ_{normal}^* vs. ϕ , and such measurements are neutral to the direction of the stripe with respect to the applied force direction; but samples were installed in similar perpendicular directions as panels (a) and (c).

Figure 5.3c and Figure 5.3d shows plots of σ_{cs}^* and τ_{cs}^* vs. ϕ for the cases where the applied force—which is applied parallel to the substrate interface—is acting in a direction that is perpendicular and parallel to the bitumen stripe along its long direction, respectively. Figure 5.3e shows a plot of σ_{normal}^* vs. ϕ .

When bitumen is $\phi = 0\%$, this means that the substrate is pure Macor[®], and such substrates have the highest values of τ_{shear}^* of the four surface bitumen fractions studied. The lowest value of τ_{shear}^* was measured in the case of $\phi = 67\%$ (Figure 5.3a). In the case of an applied parallel force to the bitumen stripe (Figure 5.3b), τ_{shear}^* correlates well with ϕ . Similar to the combined stress results in Figure 5.3c-d, the values of σ_{normal}^* in Figure 5.3e show a large spread. As mentioned before, in our experimental mode for the combined shear stress measurements, the value of σ_{cs}^* (magnitude) is larger than τ_{cs}^* . From the T-test comparison (Figure 5.3a, b), it is evident that ϕ has a marked impact on τ_{shear}^* but not on σ_{cs}^* , τ_{cs}^* , and σ_{normal}^* .

Armed with an improved knowledge of ice adhesion stress on both homogeneous and composite samples, we can state that Macor[®] is the component with the highest values of τ_{shear}^* , σ_{cs}^* , τ_{cs}^* , and σ_{normal}^* . To reduce its adhesion to ice, we deposited a previously developed superhydrophobic coating¹⁹⁰ onto the Macor[®] surface. Micrographs of pure Macor[®] (Figure 5.4a) and the superhydrophobic coated Macor[®] (Figure 5.4b; SHM) reveal that the coating is

uniform. SHM was measured to have a receding contact angle of $> 150^\circ$ at room condition (Figure 5.4c) with very small $< 1^\circ$ contact angle hysteresis. Even with care taken to keep environmental conditions dry, while cooling the substrate to -10°C , condensation likely formed on the Macor® and SHM surface roughness, causing the receding contact angle to decrease. This is a result of the fact that the droplet is at ambient temperature and has a higher vapor pressure around the droplet ¹⁹⁵. Using Macor® and SHM substrates, Figure 5.4d, Figure 5.4e, and Figure 5.4f show plots of τ_{shear}^* ; σ_{cs}^* and τ_{cs}^* ; and σ_{normal}^* , respectively.

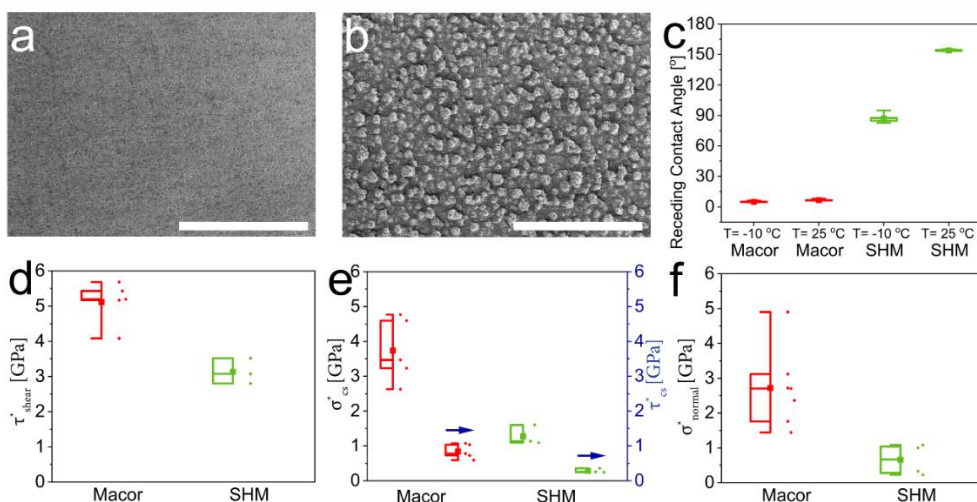


Figure 5.4 Reducing ice adhesion to Macor®. Micrographs of a) a pure Macor® surface and b) a Macor® substrate with a superhydrophobic coating (SHM). c) Receding contact angles of a water droplet on Macor® and SHM at two sample temperatures of 25°C and -10°C and environmental condition of $RH < 1\%$ at $24 \pm 1^\circ\text{C}$. Plots of ice adhesion stress on Macor and SHM: d) τ_{shear}^* , e) σ_{cs}^* and τ_{cs}^* , and f) σ_{normal}^* . Scale bars: (a)-(b) 1 mm.

The wettability results show that the superhydrophobic behavior of this and any other similar coating depends on the environmental temperature and the relevant values of contact angles are not those of measurements in standard atmospheric conditions but those measured at the actual low-temperature

experimental conditions (Figure 5.4c). Increasing the hydrophobicity of Macor® leads to a decrease in τ_{shear}^* , σ_{cs}^* , τ_{cs}^* , and σ_{normal}^* —by approximately half—compared to its initial value on untreated Macor® (Figure 5.4d-f). Several possible mechanisms contribute to reducing ice adhesion stress on hydrophobic surfaces. First, trapped air pockets in the surface topography of hydrophobic coatings provide weak mechanical bonding between ice and substrate¹⁹⁶. These cavities can behave as localized stress zones and make it easier to break the ice–substrate interface¹⁹⁷. Secondly, low surface energy coatings can reduce ice adhesion stress⁷². Furthermore, it is possible that a portion of the superhydrophobic coating is actually removed during the ice detachment process, with the top layer of the coating acting as a sacrificial layer. From the practical aspects, on the one hand, using a superhydrophobic coating on pavements raises concerns of coating durability, and the reduced traction forces on the pavement due to surface chemical treatments that could negatively affect skid resistance. On the other hand, it is shown that mechanical hysteresis resulting from rubber tire deformation with pavement's rough surface topography can hold the required friction^{31,181,198,199}.

Before discussing our results further, we reiterate our objective of increasing the intrinsic icephobicity of surfaces relevant to roads after understanding ice adhesion on heterogeneous bituminous surfaces with the main component elements of road surfaces (bitumen and gravel). The next consideration is the effect of the *material order* in the direction of applied force (that is, bitumen first or Macor® first) on ice adhesion stress. The ice contact areas on these materials are equal. Figure 5.5a shows a plot of τ_{shear}^* vs. the material order appearance with respect to the applied force direction for bitumen-Macor® and bitumen-SHM substrates.

Figure 5.5b shows a plot of σ_{cs}^* and τ_{cs}^* vs. the material order appearance with respect to the applied force direction for bitumen-Macor® and bitumen-SHM substrates.

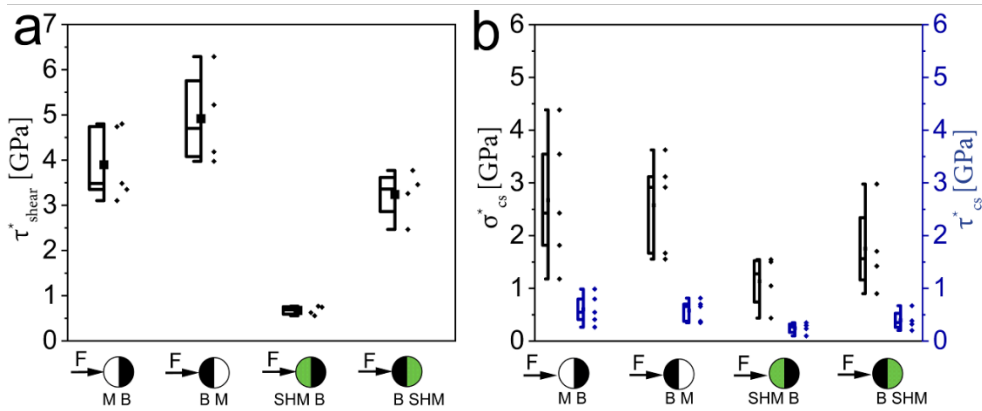


Figure 5.5 The role of material order on ice adhesion to heterogeneous bituminous surfaces. Ice adhesion on the boundary of compliant-rigid materials and impact of the material order for ice adhesion mode of a) τ_{shear}^* and b) σ_{cs}^* and τ_{cs}^* . The color code and abbreviations are black for bitumen (B), red for Macor® (M), and green for chemically coated superhydrophobic Macor® (SHM).

When the rigid Macor® (or SHM) is placed before the softer bitumen, τ_{shear}^* is lower than in the opposite case, Figure 5.5a. In both material order configurations, by making the Macor® superhydrophobic, the value of τ_{shear}^* decreases. Notably, lower τ_{shear}^* were recorded when synergy both parameters of the material order and Macor® surface coating. The lowest value of τ_{shear}^* was measured when the SHM was the first material to appear—relative to the applied force—followed by bitumen. In the case of the combined stress, the material order appearance relative to the applied stress direction has an effect on σ_{cs}^* and τ_{cs}^* , although both results are less pronounced compared to the pure shear stress case.

Although σ_{cs}^* is larger than τ_{cs}^* , the trend remains similar, and the SHM-bitumen substrate shows a lower ice adhesion stress (Figure 5.5b).

The above behavior—where the ice adhesion stresses are lower when the rigid material appears first, and the softer material appears second relative to the applied force—can be explained by the interfacial interaction of ice with rigid and soft substrates. Soft materials, to an extent, can deform by the stresses in any direction, while rigid materials cannot follow interfacial strains in contact with another solid body. The elasticity of a soft substrate can potentially prevent early micro-crack formation under small strains, and the existing cracks cannot connect and propagate along with the interface. The applied force hits the ice mold from a single point with a high-stress concentration at the location of force. Therefore, when the soft material appears first relative to the applied force, larger stresses on the soft material can be paid off by high strains and allow the rigid section also contributes to the carrying ice adhesion stress. When the rigid section is the first material, due to negligible strain, the stress cannot completely transmit, and the contribution of the soft section remains limited. Thereafter, the half area of the ice mold on the rigid section mainly takes the stresses, and when the stress reaches the critical point, the ice substrate detaches by lower applied forces.

5.5 Discussion and conclusions

This study investigated ice adhesion on heterogeneous (bitumen-Macor®) materials representative of elementary road surface composition in three modes: pure shear, combined stress, and normal-tension. We showed that Macor® yields the highest ice adhesion stresses compared to bitumen. Two parameters of the sample heterogeneity, namely, direction with respect to the applied force

(perpendicular or parallel) and the bitumen fraction of the composite substrates mainly affect the pure shear mode adhesion. By increasing the bitumen fraction, the pure shear stress mode showed a decreasing trend. Moreover, it is shown that a superhydrophobic coating can reduce the ice adhesion stresses of rigid Macor® at low temperatures. Ice adhesion stresses of Macor® after surface treatment decrease to the same range as for homogeneous bitumen alone and is half of the initial (before coating) value of pure Macor®. We also found that for ice formed half on the bitumen and half on Macor® (or Macor® made superhydrophobic), if Macor® is first and bitumen second (material order), with respect to the applied force direction, then the measured ice adhesion stress is less compared to the reverse case. This material order combined with the surface treatment modification reduced ice adhesion stresses further. In this case, the results were also lower than ice adhesion stress values for each component material.

The present basic results show concepts that can affect ice adhesion on surfaces relevant to road and other applications, where mechanical heterogeneity is present. Future studies can exploit such basic concepts on larger scale applications, aiding the development of surfaces with facile ice removal properties, while also complying with available guidelines and standards of mechanical performance, skid resistance, and environmental footprint.

5.6 Acknowledgments

This work was supported by the Swiss National Science Foundation [grant numbers 200020_169122 / 1]; and the European Research Council under Advanced Grant (INTICE) [grant number 669908].

6 CONCLUSIONS & OUTLOOK

6.1 Conclusions

This thesis has contributed to developing a deeper understanding of the bituminous materials subzero temperature behavior and interfacial phenomena of condensation freezing and ice adhesion, constructing a pathway for designing intrinsic icephobic bituminous surfaces.

First, the bitumen surface microstructures were studied as a function of cooling from room condition. Then, the chemical composition of the bitumen surface domains was analyzed, and their chemical contrast was mapped using an advanced microscopy technique. It is shown that new transition and sal domains emerge at cold temperatures in addition to the bitumen initial three surface domains. Moreover, we show that the bitumen surface microstructures evolve based on both temperature and the cooling rate.

Then, the focus thesis shifted to the topic of the interaction of bitumen with water and delved into condensation freezing phenomena on bituminous surfaces. It is shown that initial environmental relative humidity and substrate cooling rate can alter the condensation and freezing nucleation temperatures. The mechanisms of different phenomena such as temperature jump and ice bridging of the freezing supercooled droplets on bituminous surfaces were explained. Toward designing intrinsic icephobic road materials, a phase change material modification was introduced, and its performance at subzero temperatures to prevent condensation freezing was examined.

Finally, ice adhesion stresses on bituminous surfaces were investigated, and affecting parameters were studied. The goal was set to measure ice adhesion on heterogeneous soft-rigid surfaces reminiscent of the heterogeneous asphalt road surfaces. The results showed that the heterogeneity direction has no pronounced impact on the ice adhesion stress. In contrast, rigid-soft heterogeneous substrate material order with respect to the applied stress can significantly decrease ice adhesion stress if the rigid material is the first material. Ice on modified samples showed lower adhesion stresses by taking advantage of surface treatment technology developments regarding fabricating hydrophobic and icephobic surfaces.

6.2 Outlook

This thesis investigated the fundamentals of icing-resistant bitumen-based materials. It would be valuable to upscale the current approaches and test the abrasion resistance, mechanical durability, and skid-resistance of the materials. The environmental footprint and service life performance of such modified surfaces need to also be examined. Two technologies were investigated on the one hand, bitumen modification and on the other aggregate surface modification. Both these technologies can be developed further to retard ice formation and reduce ice adhesion in asphalt pavements.

Based on the current developed knowledge, we could also suggest further studies on designing an artificial aggregate with embedded inner phase change material and outer shell with intrinsic superhydrophobic surface properties. These engineered aggregates could replace as fillers or other mineral aggregates of the asphalt mixture. It is also recommended to tune the phase change material capacity

and activation temperature based on the day and night temperature cycle to prevent overheating of pavement during the day sunlight by absorbing heat and postponing ice formation overnight by releasing heat.

APPENDIX A

Specimen properties

Annealed bitumen sample on the glass coverslip, disregarding the edges, covers approximately a uniform thickness. To estimate the thickness of the 1.5 ± 0.5 mg heat-casted bitumen samples on the coverslips, we assume that bitumen covers approximately an area of 2 mm by 2 mm uniformly (Figure A.1a). The bitumen is from Q8 petroleum²⁰⁰ with penetration grade 70/100 and a density of 1029 kg/m^3 . Therefore we can calculate its volume based on the known weight and density for a given area, and then it is possible to calculate the approximate film thickness.

$$m = \rho V = \rho Ah \quad (\text{A. 1})$$

$$2 \times 10^{-3} [\text{gr}] = \left(1029 \times 10^3 \left[\frac{\text{gr}}{\text{m}^3} \right] \right) \times (4 \times 10^{-6} [\text{m}^2]) \times h [\text{m}]$$

$$h = 4.86 \times 10^{-4} [\text{m}] \approx 500 [\mu\text{m}]$$

AFM-IR and experimental setup

We used a nanoIR2 device from Anasys Inc./Bruker. A pulse tuned laser gun from Daylight Solutions, model MIRcat-2400, is used as the IR laser, consisting of four sources, covering a range of wavenumbers from 892 cm^{-1} to 1958 cm^{-1} (wavelength: 5 to $11.5 \mu\text{m}$; maximum power: 50 mW). This IR range is suitable for characterizing organic materials such as bitumen.

This AFM-IR is equipped with an environmental chamber to run scans in controlled conditions. Besides, we used aluminum and copper disks to elevate the sample position for the AFM-IR measurements, but we confirmed that surface temperature quickly follows the stage temperature (see Figure 3.4d). Since we cannot monitor the surface temperature (T2) during scanning, we calibrated the

sample surface temperature (T₂) versus the stage stepwise cycle (T₁) using a T-type thermocouple for similar conditions.

To do AFM-IR scans in the tapping mode, the AFM topography and phase scans were collected using the first mechanical resonance of the cantilever. We used gold-coated probes (Model: PR-Ex-TbIR-A-10) in the attraction regime of the tapping cantilever tip and sample. In the attraction regime, the cantilever operates below its free oscillation resonance. The free oscillating tapping peak frequency was tuned while the cantilever was at a distance of 100 μm above the sample surface. The first mechanical resonance frequency of the probes was 60 ± 15 kHz, with a spring constant of 1 to 7 N/m. The corresponding phase angle for the resonance frequency peak served as the reference phase angle and zero value for the AFM phase contrast image and as an intermediate value for the substrate compliance. However, the operating frequency of the cantilever during scanning is different from the free oscillation resonance, because when the cantilever approaches the surface, tip, sample forces emerge. Therefore, we set the operation frequency resonance 5% below the free oscillation peak based on the manufacturer's recommendations. The AFM scan setting was for the attraction regime of the tapping cantilever tip and sample. In the attraction regime, the cantilever operates below its free oscillation resonance (set to 5% below free oscillation peak based on the manufacturer recommendation). The corresponding phase angle for the resonance frequency peak served as the reference phase angle and zero value for the AFM phase contrast image as an intermediate value for the substrate compliance.

We scanned all AFM-IR images in an enclosed environmental chamber to control humidity and sample temperature. Figure A.1b shows a schematic drawing and thermal diagram of the AFM-IR chamber. The black thin film (ca. 0.5 mm

thickness) is the heat-casted bitumen sample on a glass coverslip Figure A.1a. Two copper and aluminum disks (each 1 mm thick) raise the position of the sample and hold it on the magnetic temperature stage. We use a thin film of thermal paste in between all of the interfaces to reduce the thermal conduction resistance. In a control test, a T-type thermocouple on the bitumen surface measures the surface temperature (T_2) with stage temperature (T_1). Temperature history T_1 vs. T_2 was plotted in Figure 3.4d (in the main text) to show the heat diffusion delay through the sample and sample holder.

The thermoelectric device (Peltier stage) cools the sample by removing heat away from the sample, and the heat exchanger transfers heat to the coolant water. The pump circulates water as a coolant fluid of the thermoelectric in a closed loop. Water circulation through the heat exchanger removes the heat away from the hot side of the Peltier stage. It should be noted that the circulating water temperature never goes below its freezing temperature. Removed heat dissipates to the environment from the water reservoir at room conditions. The control feedback loop of the thermoelectric device is connected to the T_1 sensor, as shown in Figure A.1b by the red dot. The surface temperature and cooling rates were verified by measuring the sample stage temperature, T_2 versus T_1 , as shown in Figure A.1b. To avoid icing on our bitumen surface, we circulate dry nitrogen flow in the chamber, keeping the humidity low during the AFM scan.

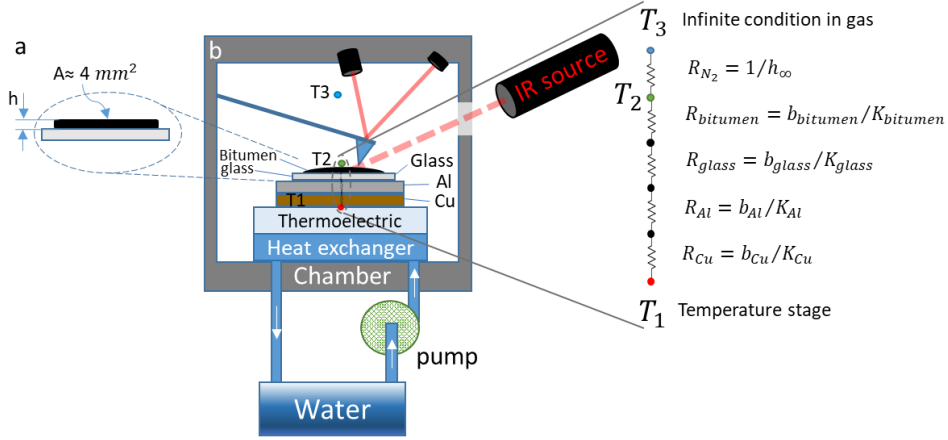


Figure A.1 Schematic drawing of the AFM-IR enclosed environmental chamber, the stage temperature cooling cycle, and sample properties. a) Sample on a glass slide. b) Configuration of AFM cantilever *and* thermal resistance diagram, the laser feedback detector, and an IR transparent window. Copper and aluminum disks (each with 1 mm thickness) elevate the sample position. Color dots show the location of the three thermocouples, red dot: stage temperature thermocouple (T1), green dot: thermocouple for surface temperature (T2) measurement, blue dot: humidity sensor and thermocouple as environmental temperature sensor (T3).

Thermal properties of the bitumen sample are obtained from the literature³³, and for the other materials, we obtained properties from a heat transfer textbook²⁰¹. The thermal resistance of each layer is calculated by $R=b/K$, b is the layer thickness, and K is the thermal conductivity. The thickness of the materials are as follows:

$$b_{Cu} = 1 \text{ mm}, b_{Al} = 1 \text{ mm}, b_{glass} = 0.25 \text{ mm}, b_{bitumen} \approx 0.5 \text{ mm}$$

The thermal conductivity of the materials are as follows^{33,201}:

$$K_{Cu} = 385 \text{ [W/m.K]}, K_{Al} = 205 \text{ [W/m.K]},$$

$$K_{glass} = 0.8 \text{ [W/m.K]}, K_{bitumen} \approx 0.15 \text{ [W/m.K]}$$

Therefore, the total thermal resistance is calculated as the sum of the individual resistances:

$$\begin{aligned}
 R_{\text{total}} &= \frac{b_{\text{Cu}}}{K_{\text{Cu}}} + \frac{b_{\text{Al}}}{K_{\text{Al}}} + \frac{b_{\text{glass}}}{K_{\text{glass}}} + \frac{b_{\text{bitumen}}}{K_{\text{bitumen}}} & (\text{A. 2}) \\
 &= \frac{1 \times 10^{-3}}{385} + \frac{1 \times 10^{-3}}{205} + \frac{0.25 \times 10^{-3}}{0.8} \\
 &\quad + \frac{0.5 \times 10^{-3}}{0.15} = 3.33 \times 10^{-3} \text{ [K/W]}
 \end{aligned}$$

Cantilever resonance properties

During cantilever free oscillation tuning, we set the zero phase angle based on the manufacturer's recommendation. The value of the phase angle was set to zero for the frequency of the first mechanical resonance peak. This means that the reference phase of the lock-in is adjusted to zero at the unique operating frequency depending on the cantilever to yield results independent of the cantilever mechanical resonance properties. It is useful to perform an auto-tuning before the experiment to cancel out differences from cantilever to cantilever (which are not relevant for the comparison on or within the samples) leading to the phase images in this manuscript being relative values to the initial zero phase reference values. If we change the cantilever and use another cantilever of the same type, we will obtain a similar stiffness map. Otherwise, it would be challenging to compare scan results from different cantilevers. Figure A.2 shows the amplitude (deflection of the cantilever in volts) and phase shift (in degrees) of the cantilever in (a) first and (b) second mode mechanical resonance frequencies.

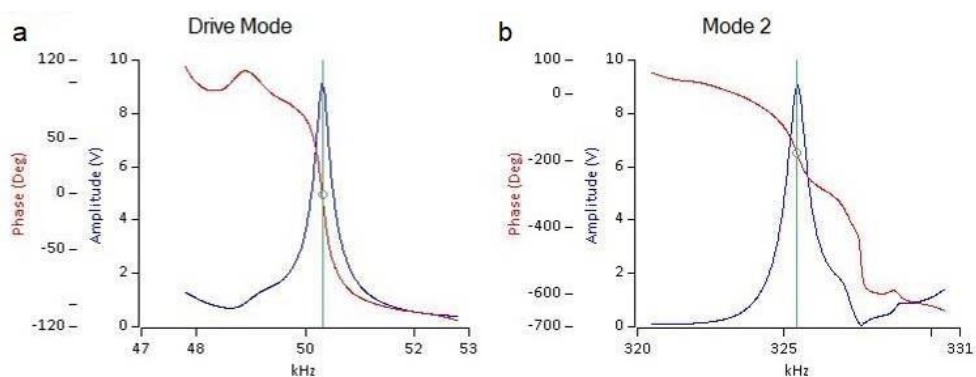


Figure A.2 An example of phase and amplitude versus frequency for an AFM-IR cantilever probe (Model: PR-Ex-TbIR-A-10). a) Oscillation phase and amplitude signal versus free oscillation tapping frequencies at the first mechanical resonance and, b) the second mechanical resonances.

Keeping the setpoint value constant is not practical because the cantilever and substrate temperature have an effect on the required set point for a good scan. The exact nm values for the cantilever amplitude is not provided. Therefore we always used the auto setpoint function as recommended by the manufacturer to keep the results comparable. We always used the auto setpoint function. The maximum oscillation amplitude of the cantilever is in the range of 7 V to 9 V. 70% of that value is the auto setpoint value. Usually, the setpoint was in the range of 4 V to 6 V. We always chose about 0.3 to 0.5 V below the auto set point to make sure that the tip keeps following the surface topography for the entire scan.

Post-processed and original AFM images at various temperature steps

Figure A.3 shows post-processed AFM phase scans (original images are shown in Figure A.5) based on their color contrast to calculate area fractions of para, sal, and transition domains. False-colored blue indicates para domain.

Emerged sal sub-domain at cold temperatures is colored artificially in red and green, showing the transition domain.

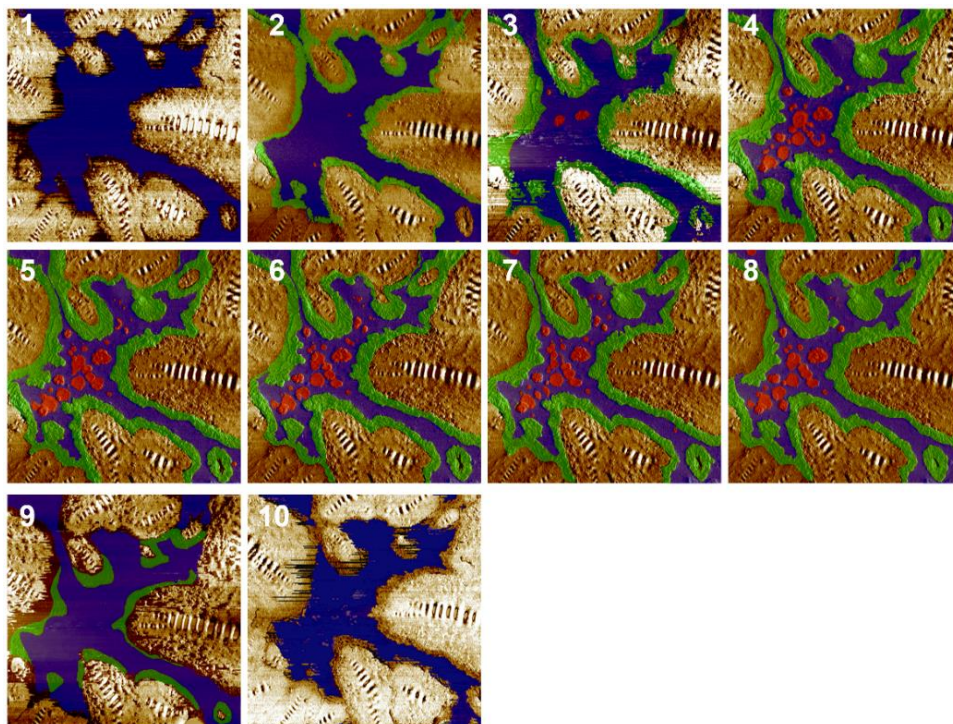


Figure A.3 False colored domains of the bitumen AFM phase scans at the same location. All scans conducted at dry condition ($T_3 = 20 \pm 3^\circ\text{C}$, $\text{RH} < 3\%$) in ten stepwise temperature stages (T_1) steps: 1: $+25^\circ\text{C}$ 2: $+15^\circ\text{C}$, 3: 0°C , 4: -10°C , 5: -20°C , 6: -25°C , 7: -30°C , 8: -35°C then the sample were reheated to the initial conditions, step 9: reheat to 0°C and 10: reheat to 25°C . Color code: green: transition domain, blue: para domain, red: sal sub-domain.

Figure A.4 shows an example of an AFM topography scan consisting of ten sequential stage temperature steps. Starting from Figure A.4-1 at room condition ($T_1 = 25^\circ\text{C}$) para domain is smooth, but it coarsens below $T_1 = 0^\circ\text{C}$ (Figure A.4-3). After reheating to $T_1 = 0^\circ\text{C}$ (Figure A.4-9), the topographical trace of newly emerged sal sub-domain and transition domain fade with decreasing temperature.

At the final step 10 reheating to the initial condition $T_1=25\text{ }^\circ\text{C}$ (Figure A.3-10) surface re-heals and formed roughness disappears.

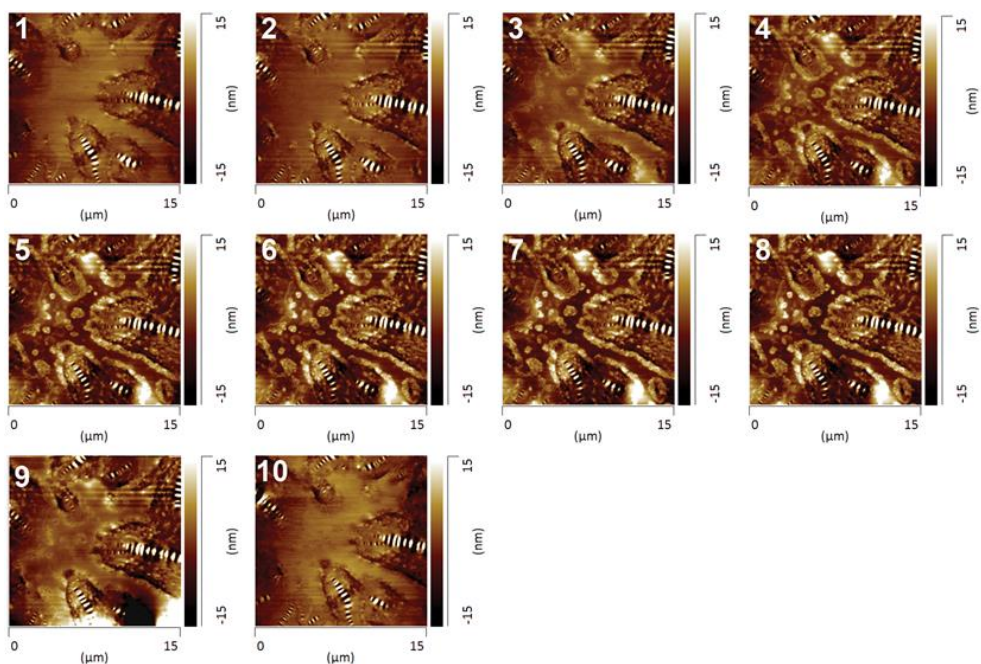


Figure A.4 Example of a sequence of AFM topography scan at the same location. All scans conducted at dry condition ($T_3=20\pm 3\text{ }^\circ\text{C}$, $\text{RH}<3\%$) in ten stepwise temperature stages (T_1) steps: 1: $+25\text{ }^\circ\text{C}$ 2: $+15\text{ }^\circ\text{C}$, 3: $0\text{ }^\circ\text{C}$, 4: $-10\text{ }^\circ\text{C}$, 5: $-20\text{ }^\circ\text{C}$, 6: $-25\text{ }^\circ\text{C}$, 7: $-30\text{ }^\circ\text{C}$, 8: $-35\text{ }^\circ\text{C}$ then the sample was reheated to the initial conditions as follows: step 9: reheat to $0\text{ }^\circ\text{C}$ and 10: reheat to $25\text{ }^\circ\text{C}$.

Figure A.5 shows the corresponding AFM phase scan for the topography scans in Figure A.4 in tapping mode. However, at the beginning (Figure A.5-1), peri and para domains have high color contrast, which indicates the para domain is softer than the peri domain, but their mechanical properties develop to be closer as the para domain stiffens at cold temperatures. Again the main changes and emergence of new domains are visible at $T_1=0\text{ }^\circ\text{C}$ (Figure A.5-3), and the sal sub-domain and transition domain grow gradually at lower temperatures (Figure A.5-4 to Figure A.5-8). After reheating to $25\text{ }^\circ\text{C}$ (Figure A.5-9 and Figure A.5-10), para

and peri domains recover their high phase contrast. It is noteworthy to mention that upon reheating the domains that do not fully recover, we attribute this to thermal aging as bitumen is a highly thermally sensitive material. This is expected as previous work has shown that the bitumen at 25 °C needed almost 24 hours to fully regain structural equilibrium¹²⁰.

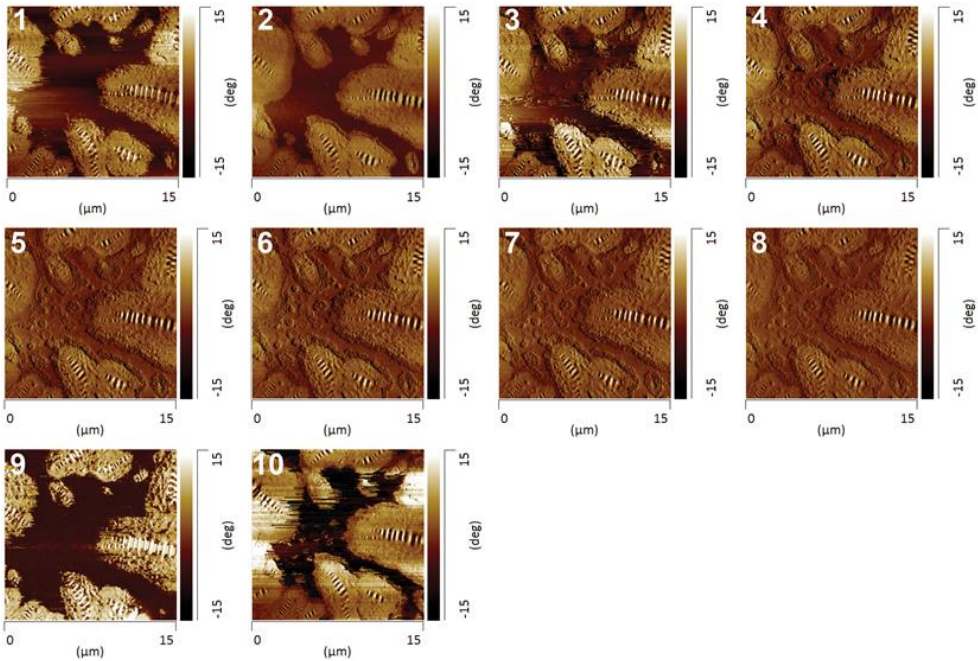


Figure A.5 Example of a sequence of AFM phase scans (stiffness map) at the same location. All scans conducted at dry condition ($T_3 = 20 \pm 3$ °C, $RH < 3\%$) in ten stepwise temperature stages (T1) steps: 1: +25 °C 2: +15 °C, 3: 0 °C, 4: -10 °C, 5: -20 °C, 6: -25 °C, 7: -30 °C, 8: -35 °C then the sample was reheated to the initial conditions as follows: step 9: reheat to 0 °C and 10: reheat to 25 °C.

Figure A.6 defines the boundary of domains on the topography scans based on their corresponding AFM phase scans. Moreover, overlaying of AFM scans of the same locations on each other indicated that distance in between microstructures, which is because of volumetric change as a function of temperature decrease. Figure A.6 shows the supporting information of Figure 3.3

from the Chapter 3. We always defined domains based on the stiffness map (AFM phase image). To recognize the location of the protruded area, we marked boundaries of domains on the topography scans (Figure A.6a and b) based on their corresponding stiffness maps (Figure A.6d and e). Magnified views of (Figure A.6b, and e) are plotted as Figure A.6c and f panels, respectively. Both the sal sub-domain and transition domains protrude from the surface and make a distinguishable contrast from their initial host domains. Moreover, comparing the same location AFM scans (Figure A.6a with b) at different temperatures, indicates that microstructures are shifted, and the distance between microstructures has been changed, which could be due to the material, volumetric changes as a function of temperature decrease.

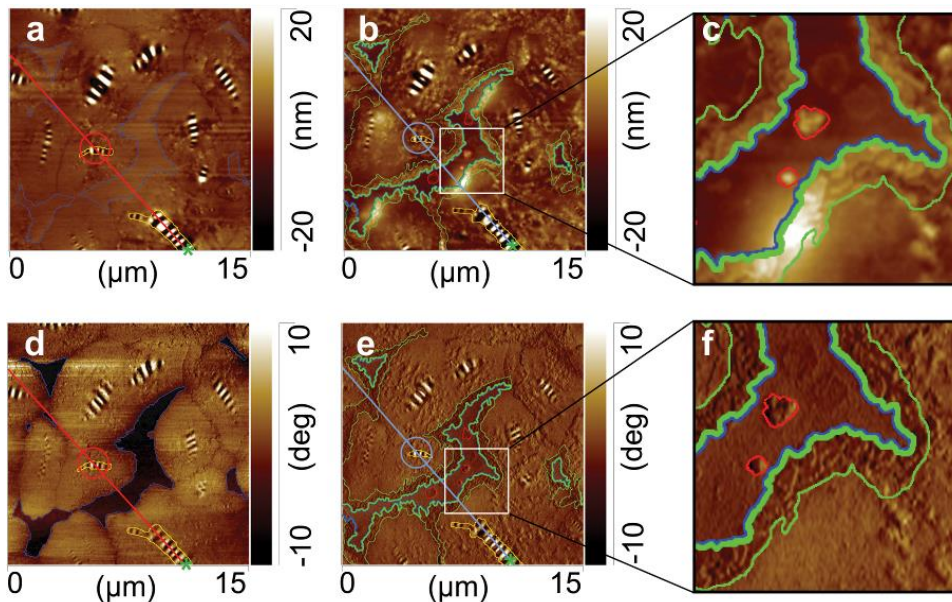


Figure A.6 Defining boundaries of the surface domains on the topography scans based on the corresponding stiffness maps (AFM phase scan) for two temperature steps of the stepwise cooling. Topography scans at practically the same location, selected steps from a sequential stepwise cooling, a) topography at $T_1=25$ °C, the red straight line shows the pass through-line of the surface profile at high temperature and the red circle indicates location of

a bee structure. b) Corresponding AFM phase scans at $T_1=25$ °C. c) zoomed area for the location of the square, see (b). d) topography at $T_1=-20$ °C, blue straight line shows the pass through-line of the surface profile at low temperature, and the blue circle indicates the location of the same bee structure. e) Corresponding AFM phase scans at $T_1=-20$ °C. f) Zoomed area for the location of the square, see (e). Color-code, red: the boundary of sal sub-domain, blue: the boundary of the para domain, green: the boundary of the transition domain and yellow: the boundary of catana domain.

Furthermore, as mentioned earlier in the main text, the wrinkles of the bee structures shrink at cold temperatures, and their amplitude and length decrease by 10-20%. However, their wavelength value varies around its initial value (Figure A.7). This information is for this particular crude origin, and its validity for other crudes remains to be investigated.

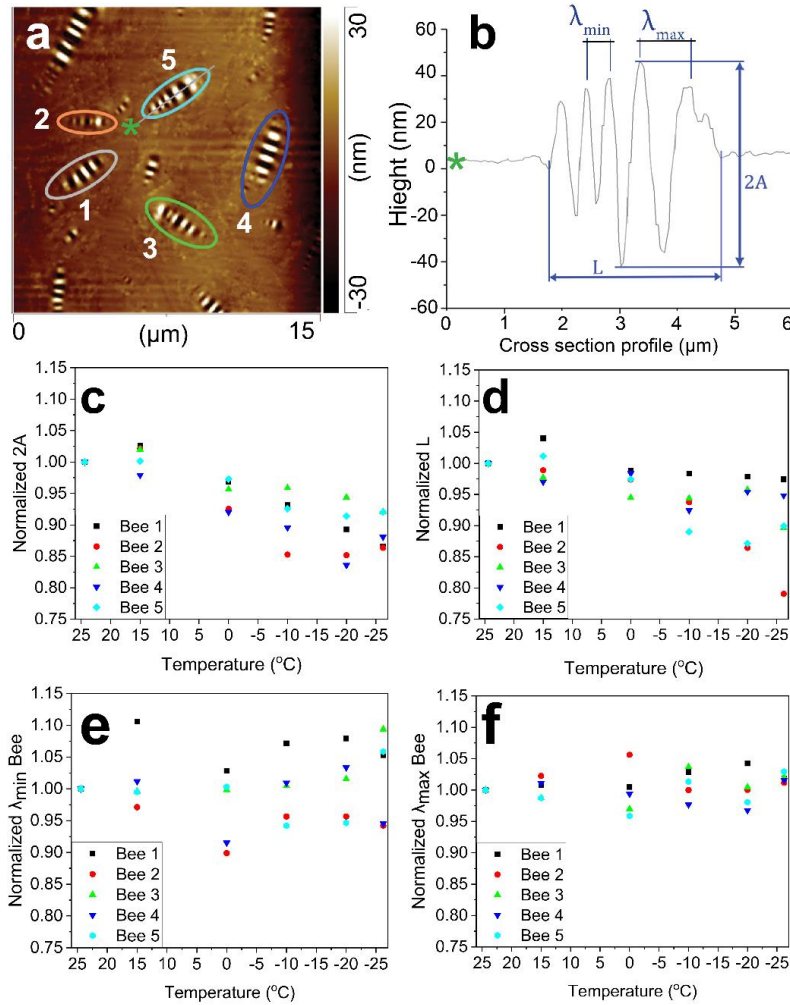


Figure A.7 Effect of temperature on the profile of the catana domain. All values are normalized by their initial value at room temperature. (a) Location of the color-labeled catana domains. (b) Definition of twice the amplitude $2A$: distance from the minimum valley to maximum hill in the y -direction, catana domain length L : from the first wrinkle to end of the last period when $y=0$. We showed the smallest and the largest measured bee profile wavelength with λ_{\min} and λ_{\max} (c) Normalized the $2A$ of each tracked catana domain versus temperature. (d) The plot of the ratio of the length of each catana domain to its initial length at 25 °C, i.e., normalized L with respect to the stage temperature. (e) The ratio of the smallest wavelength of each catana domain to its initial length at 25 °C, i.e., normalized λ_{\min} with respect to the stage temperature. (f) The ratio of the largest wavelength of each catana domain to its initial length at 25 °C, i.e., normalized λ_{\max} with respect to the stage temperature.

DSC analysis

We followed a previously reported DSC bitumen sample preparation method¹³⁰, to perform DSC experiments using a PerkinElmer® 7, 1993 device with temperature change rates of 1.5 °C/min and 90 °C/min, which match our AFM-IR experiments (Figure A.8).

When heating or cooling a sample at the same rate, the glass transition occurs practically in the same temperature range; however, in the cooling ramp, the glass transition temperature range can be broader¹³⁰. Therefore, for clarity, only the heating curve is reported here. Bitumen has four different components that crystallize at various temperature ranges: asphaltenes: 40 to 60 °C, resins: 10 to 20 °C, aromatics: -34 to -15 °C and saturates: -88 to -60 °C^{104,115}. Guo et al.²⁰² reported that the heating and cooling rates affect the crystallization and the glass transition temperatures of bitumen. They found that they were unable to determine a glass transition temperature for relatively low heating rates. We also found that we were unable to accurately calculate any glass transition temperature for the slow heating rate of 1.5 °C/min^{202,203} (Figure A.8).

During the cooling cycle and depending on the cooling rate, waxy paraffinic compounds crystallize (freeze or solidify) in an amorphous state and subsequently form different surface microstructure patterns¹³⁰. During reheating, when the temperature reaches or exceeds T_g , the methylene groups of n-alkane chain with sufficient mobility rearrange to all necessary conditions of crystallization¹³⁰. Our findings corroborate previous results²⁰²: Figure A.8 shows a clear glass transition at a cooling rate of 90 °C /min of $T_g = -35.75$ °C. Considering the T_g of the SARA fractions, this indicates that at this rate, the developed microstructures can be attributed to the asphaltenes and resins. However, at a slower cooling rate of 1.5

°C/min, although no T_g could be clearly distinguished in the bulk material using DSC data, still at the nanoscale microstructures do appear as shown, for example in Figure A.8.

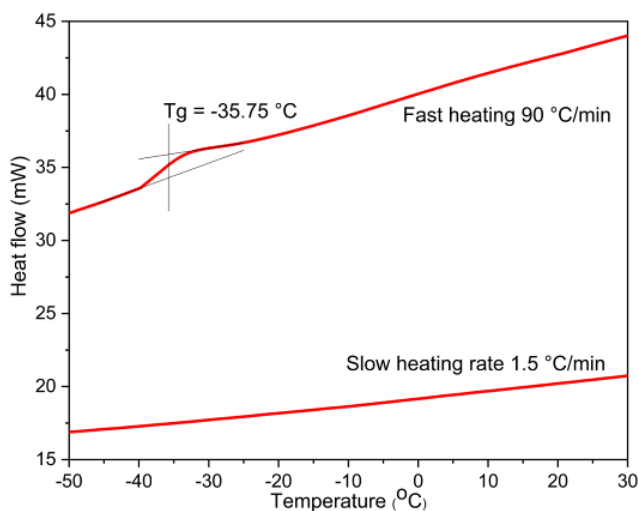


Figure A.8 DSC results of the Q8 70/100 virgin bitumen. For two heating rates of 1.5 °C/min and 90 °C/min calculated T_g for the fast rate of 90 °C/min is -35.75 °C.

CHEMISTRY ANALYSIS BY IR METHODS

Figure A.9 shows both unfiltered and noise filtered local AFM-IR spectra using the Savitzky-Golay function (Figure A.9a) next to the original signals plotted in Figure A.9b; bulk FTIR spectra in both panels is an average of 32 measurements without applying the noise filter. The plotted spectra demonstrate that the filtered AFM-IR spectra (Figure A.9a) show the same peaks and follows the same trend as the original noisy signal (Figure A.9b).

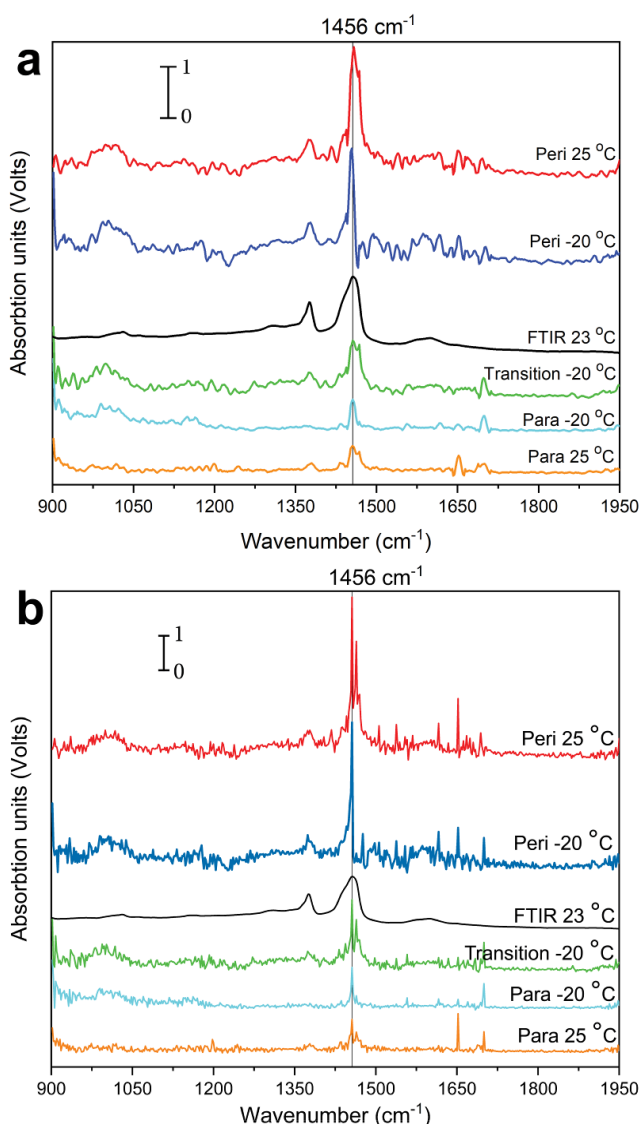


Figure A.9 Post-processed vs. noisy IR spectra of the surface domains in two temperature conditions: $T_1=25\text{ }^\circ\text{C}$ and $T_1=-20\text{ }^\circ\text{C}$. (a) Smoothed AFM-IR spectra by Savitzky-Golay function. A fifth-order polynomial was fitted on the six neighboring points. Bulk FTIR result is not smoothed. (b) Raw data from local AFM-IR and bulk FTIR spectra. Spectra of bitumen at 25 °C (para: orange line, peri: red line) and -20 °C (para: cyan line, peri: blue line, transition domain: green line) and the bulk FTIR spectra at 23 °C in both case plotted by the black line. The straight black line shows the location of the 1456 cm⁻¹ wavenumber.

Figure A.10a shows an AFM phase scan after a fast cooling rate, ~ -90 °C/min starting from 25 °C at T1 = -20 °C. The selected area with a white square (Figure A.10a) shows the high-resolution scan with the scan rate of 0.4 Hz for a scan area of 5 μm by 5 μm with the resolution of 500 scan points and 100 scan lines, Figure A.10b. In Figure A.10b, we show the false-colored para domain in blue, the newly emerged domains of sal in red, and the transition domain in green. Figure A.10 demonstrates the similarities both in the chemistry and mechanical properties of the sal sub-domain and transition domain at cold temperatures. Previous s-SNOM results by Fischer et al.¹²⁰ (at room condition or 0 °C, not specified) showed that the para domain consists of at least partially sulfoxide groups, and the peri domain consists of at least partially carbonyl groups. On the other hand, a recent study¹²⁶ on bitumen using a similar AFM-IR device and sample preparation method corroborates our results and shows that the peri domain also contains sulfoxide groups. AFM-IR results after a very fast cooling rate (-90 °C/min) at -20 °C show a carbonyl rich peri domain (Figure A.10f) and sulfoxide rich peri domain next to the at least a partially sulfoxide rich para domain (Figure A.10d). This result confirms that the transition domain and sal sub-domain have similar chemical composition, but the para domain exhibits a different contrast, especially for the sulfoxide 1030 cm^{-1} and aliphatic 1456 cm^{-1} chemical functional groups.

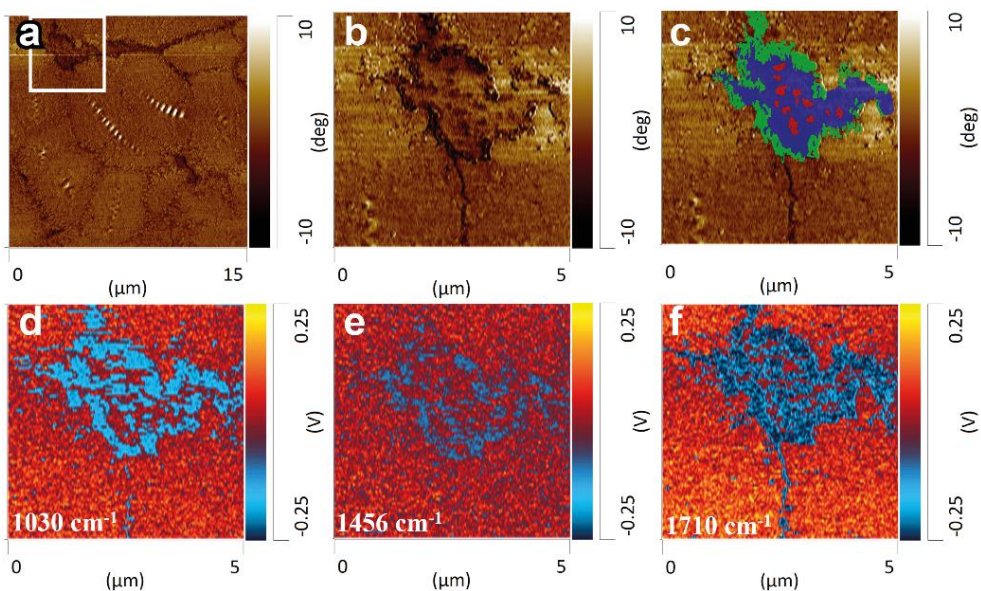


Figure A.10 Bitumen main chemical functional groups concentration distribution at cold temperatures, similar IR mapping for the transition, and sal sub-domain. AFM phase scan at (a) $T_1 = -20$ °C (directly cooled from $T_1 = 25$ °C to $T_1 = -20$ °C at a cooling rate of ~ 90 °C/min), white square shows location of the high resolution zoomed scan (b) AFM phase scan of the selected area (see a) (c) false-color of domains (see b). Color-code, blue: para domain, green: transition domain, red: sal domain. IR mapping of practically the same location at $T_1 = -20$ °C using different wavenumbers to detect (d) sulfoxide groups: 1030 cm^{-1} (e) aliphatic groups: 1456 cm^{-1} (f) carbonyl groups: 1710 cm^{-1} .

APPENDIX B



This chapter contains submitted results to ISBM, Lyon 2020:

Tarpoudi Baheri, F.; Rico Luengo, M; Schutzius, T. M.; Poulidakos, D.; Poulidakos, L. D.; The Effect of Additives on Water Vapor Condensation on Bituminous Surfaces. in Proceedings of the RILEM International Symposium on Bituminous Materials (eds. Di Benedetto, H. et al.) 1783–1789 (Springer International Publishing, 2022).

This chapter contains results of subsequent publication:

Tarpoudi Baheri, F.; Rico Luengo, M; Schutzius, T. M.; Poulidakos, D.; Poulidakos, L. D.; The Effect of Additives on Water Vapor Condensation on Bituminous Surfaces. *Journal of Testing and Evaluation*, (2021).
<https://doi.org/10.1520/JTE20210251>.

The radius of curvature of bitumen surface domains

A nanoIR2 device in tapping AFM-only mode was utilized to perform high resolution surface topography scan. This device was equipped with a water coolant thermoelectric stage and was used in conjunction with an environmental chamber to control the sample temperature. We purged the chamber volume with nitrogen to maintain environmentally dry conditions ($RH < 3\%$) and prevent surface frosting at subzero temperatures. We used atomic force microscopy in a high resolution of 1024 scan points and 1024 lines for a square scan area of $5\ \mu\text{m}$ by $5\ \mu\text{m}$. The scans were performed at two temperatures, $25\ ^\circ\text{C}$, and $-10\ ^\circ\text{C}$. Thereafter we analyzed the radius of curvature of the AFM topography scans with the use of a MATLAB® script.

Here we show the surface topography development of bitumen due to cooling. Figure B.1a, b show the contour plots of overlaid mean surface curvature (H) on the height profile as a surface plot based on high-resolution AFM scans of peri and para domains at the same location. The central flat area is the para domain (see Figure B.1a) which is surrounded by rough peri domain at $25\ ^\circ\text{C}$ as a consequence of cooling to $-10\ ^\circ\text{C}$; both domains develop more roughness (Figure B.1b). The definition of the mean surface curvature H is given in Figure B.1c, showing that it depends on the two principal radii of curvature R_1 and R_2 . In other words, the radius of curvature is the radius of the circular arc that best fits in the normal section or combination of those on a 3D surface. Negative values are for concave and positive for convex curvatures. Figure B.1d shows a histogram of the surface area fraction vs. the surface radius of curvature, given by $R = 1/H$. The histogram of Figure B.1d presents the surface area coverage percentage by different radius of the curvature size magnitudes for two temperatures of 25°C and $-10\ ^\circ\text{C}$.

Even though the radius of curvatures in the range of few nanometers can boost initial condensation and due to the AFM probe (cantilever tip) and substrate interactions and viscoelastic nature of our studied material, we could not measure surface roughness below 200 nm. Still, it can be seen that the area fraction of the smaller micro-pits increases as a function of cooling (Figure B.1d). A more remarkable topographical evolution can be observed in the initial flat para domain than the surrounding, compared to the initially rough peri domain.

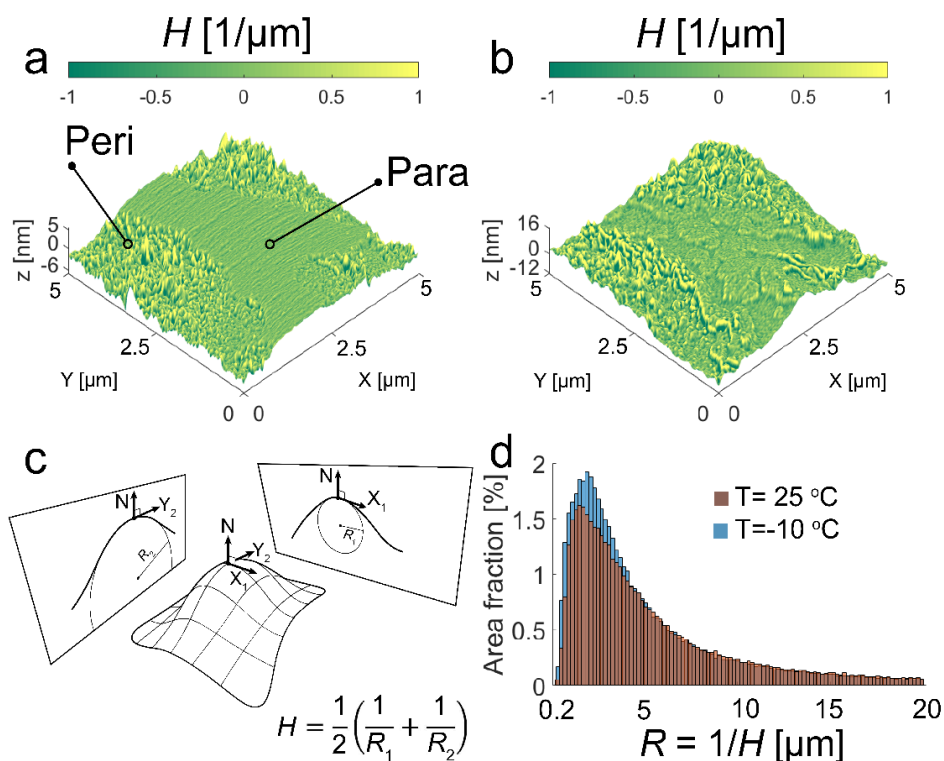


Figure B.1 **Effect of temperature on the curvature of the bitumen surface.** The mean curvature (H) is overlaid on the height profile as a surface plot based on high-resolution AFM scan of peri and para domain at the same location, central flat area, is para domain surrounded by rough peri domain, a) $T=25\text{ °C}$, and b) $T=-10\text{ °C}$. c) Schematic shows an arbitrarily curved surface in 3D which principal radii of curvature are R_1 and R_2 projected to two perpendicular plane. d) Histogram plots the surface area fraction occupied by surface roughness with different radius of curvature magnitudes. The para domain of the bitumen surface becomes rougher after cooling.

Wettability of bitumen surface domains

Optical microscopy was performed using an Olympus BX60 microscope. Two configuration modes were used to acquire optical images: dark field (DF), and differential interference contrast (DIC). Scattered light provides the DF image contrast, resulting in the visibility of bee structures, while DIC mode is better suited to detect bitumen surface structures such as peri and para domains. We first recorded condensation occurrences in DF mode and then allocated the condensation sites to the different bitumen domains using the corresponding DIC images. Several studies have confirmed that optical microscopy shows the same surface topography pattern as AFM scanning images [15-16] although not with the same resolution. Furthermore, the optical microscope equipped with a cryogenic stage provides simultaneous observation of topography and water phase change on the bitumen surface.

Condensation experiments were performed under the optical microscope on samples at room conditions ($T = 21 \pm 1$ °C; $RH = 50\%$) by introducing hot humidified nitrogen stream (at $T_{\infty} = 35 \pm 0.5$ °C and $RH = 95 \pm 1\%$) on the bitumen surface. Exposing the sample to the hot vapor provides $P_{\infty}/P_{sat}=1.6$ supersaturation condition on the sample, where the vapor pressure is P_{∞} , and the saturation vapor pressure at the corresponding temperature is P_{sat} . Here, it is of interest to observe the condensation of water droplets on the three main domains of bitumen: catana, peri, and para.

Bitumen's three main surface domains of catana, peri and para are detectable by optical DIC image (Figure B.2a). Figure B.2b shows zoomed area of the selected section from Figure B.2a, and the corresponding DF image is shown in Figure B.2c.

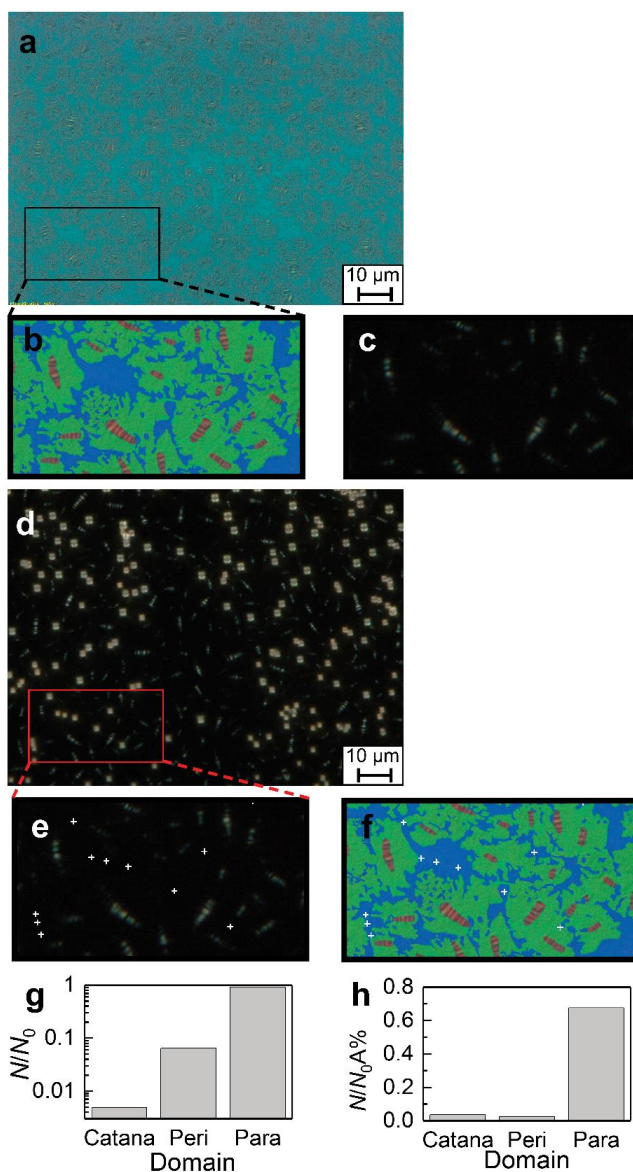


Figure B.2 Selective wettability of bitumen surface domains. a) DIC image (X100). b) Domains are highlighted by colors of, red: catana, green: peri, and blue: para. c) only bee structures are visible in DF images. d) Condensation event was recorded in DF view. e) Centers of the condensed droplets marked by white plus marks on DF images. f) Overlaid condensation sites on the DIC image of the same location. g) Ratio of the condensed droplets' number per each specific domains (N) over the total count of the condensed droplets (N_0). h) Normalized ratio of the condensed droplet with respect to the surface area fraction of each domain ($A\%$).

Figure B.2d shows a snapshot of the condensation frame. Centers of the condensed droplets are marked with white plus marks in Figure B.2e, and allocation to the different domains in Figure B.2f. The analysis of more than a thousand droplet condensation sites captured for five repeatable experiments under the same conditions shows that almost 90% of the droplets condensed on the para domain and approximately 9% on the peri domain, and less than 1% on the catana domain (Figure B.2g). The results were normalized with respect to the area fraction of each domain showing the para domain remained as the most favorable location for droplets to condense. Possible reasons for the observed preferential condensation could be the development of micro-pits in addition to the intrinsic differences of the surface chemistry of these two domains.

APPENDIX C

PCM microcapsule resistance examination

PCM microcapsules can resist mechanical and thermal stresses during sample preparation and when in contact with bitumen and toluene (Figure C.1). Figure C.1a and Figure C.1e show images of filter paper that have had a drop of a solution containing PCM modified bitumen and virgin bitumen placed on them, respectively.

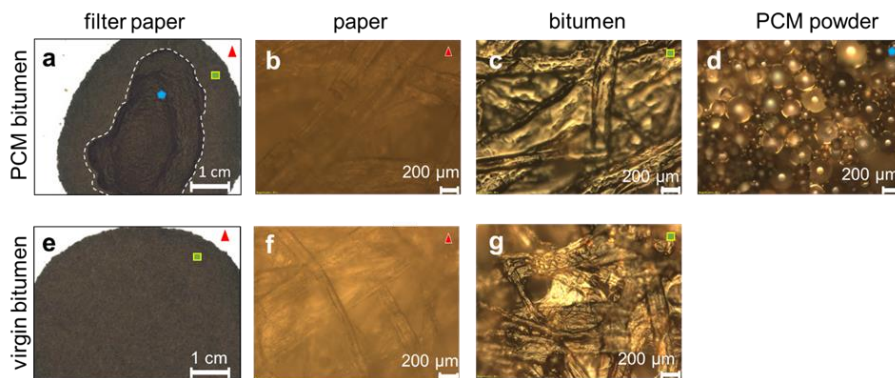


Figure C.1 **PCM microcapsule bitumen blend and virgin bitumen after mechanical and thermal stresses in contact with toluene solvent.** 150 μl of diluted bitumen in toluene on filter paper a) PCM modified bitumen stain on the filter paper e) Virgin bitumen stain on the filter paper. b), and f) The red triangle shows the location under an optical microscope for the only paper. The green square shows the stained part of the filter paper with c) PCM-modified bitumen and g) virgin bitumen. d) The blue hexagon in (a) shows the location of the microcapsules in the PCM-modified bitumen, as seen under an optical microscope.

As the drop wets the paper, it spreads, but it does not cover the whole sheet. The outer edges of the sheets, which are not covered by bitumen, have the same fibrous microstructure, Figure C.1b, f. Furthermore, micrographs of the outer edge of the bitumen deposits reveal that the PCM containing deposit and virgin bitumen

are similar, Figure C.1c, g. However, micrographs of the central portion of the PCM containing deposit reveal pristine PCM microcapsules, indicating that the processing conditions used for this study do not damage the PCM microcapsules, Figure C.1d.

Bitumen sample preparation and examination

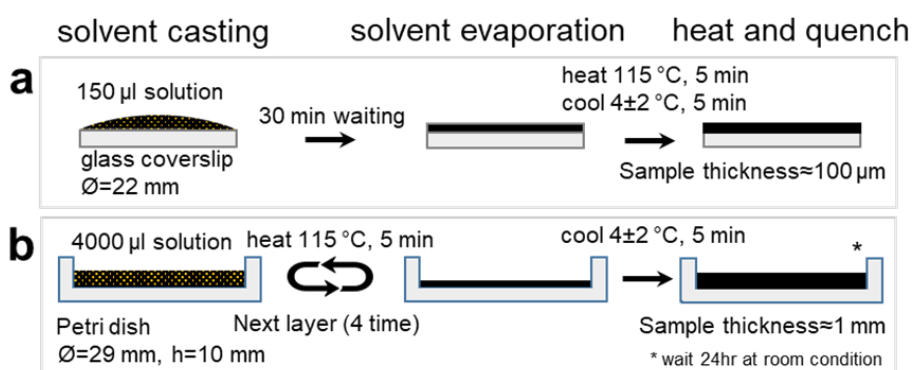


Figure C.2 **Sample preparation procedure.** a) The drop-casting method used to prepare the thin film samples for the condensation freezing studies under constant cooling rates and different environmental conditions. b) The layer by layer drop-casting method used for the thick bitumen samples used to compare the PCM-modified bitumen to the virgin bitumen in the constant cooling flux experiments.

As described in the Chapter 4 (section 4.3.2 Solution preparation and coating), we followed two sample preparation protocols based on the solvent casting method for this study. Figure C.2a shows a schematic of the “thin bitumen sample” preparation steps. Figure C.2b shows a schematic of the procedures used for the layer-by-layer drop-casting method that was used to prepare the “thick bitumen samples” in order to examine the performance of the PCM-modified bitumen in cold conditions.

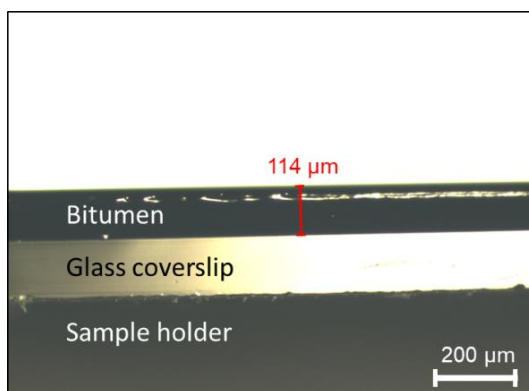


Figure C.3 Cross-section of the thin bitumen sample casted on a glass coverslip. Optical microscopy shows a uniform thickness of bitumen on the glass substrate.

For Figure C.2a, the “thin” virgin bitumen sample, we always placed 150 μl (~ 135 mg) of the diluted bitumen to evaporate on glass coverslips. After 25 minutes of evaporation in ambient conditions, the remaining sample weight decreases to ~ 35 mg (above 75 wt.% of the solution is toluene), and after the heating and quenching, the weight of the bitumen coating equaled 34 ± 1 mg. According to the mass of the bitumen coating material, the density, and the geometry of the covered area on the glass coverslip, it is expected the final coating thickness will be ~ 100 μm . This is further measured using an optical microscope (Figure C.3).

Experimental setups

Two sample cooling protocols were used for this study: Constant cooling rate and constant cooling flux. Figure C.4a, illustrates the constant cooling rate setup, which used a microscope and infrared (IR) camera to study condensation and freezing on bitumen. (“Objective” here refers to objectives for the microscope and lenses for the infrared camera at individual use of each from the access point.) For the constant cooling flux experiments, a thermoelectric device was used, and it was

possible to visualize the bitumen surface simultaneously with IR and optical cameras (Figure C.4b).

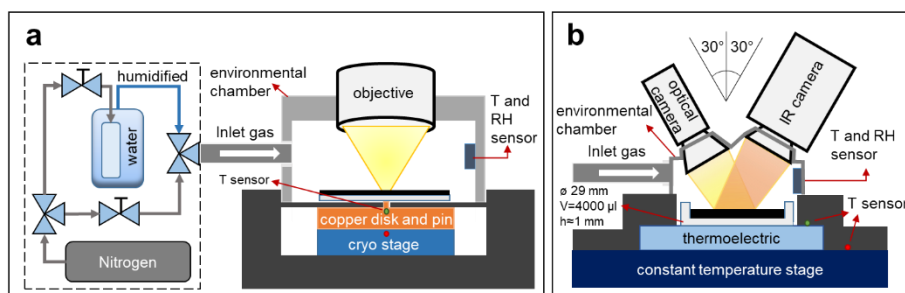


Figure C.4 **The experimental setups.** a) Constant cooling rate setup using a cryogenic stage. The location of the optical microscope objective or IR camera lens is shown as "objective". b) Constant cooling flux using a thermoelectric device.

DSC analysis

DSC BASELINE CALIBRATION

Figure C.5 shows DSC baseline graphs at two temperature rates of 10 °C/min and 20 °C/min for three cycles in the range of -50 °C to 40 °C, when both DSC pan holders are empty.

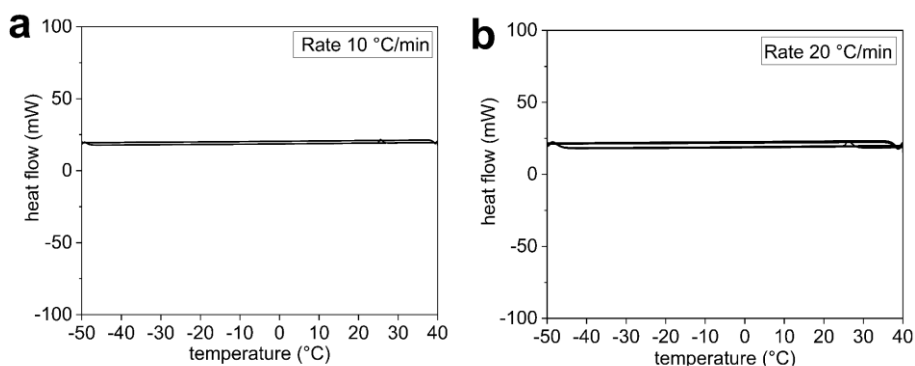


Figure C.5 **DSC baseline measurements for three cycles when both sample holders are empty.** a) 10 °C/min and b) 20 °C/min temperature rates.

Here in Figure C.6a, and b, we reported DSC analyses of virgin and the PCM modified material, respectively. We find that a faster cooling rate shifts the PCM crystallization temperature toward lower temperatures (and the melting to higher peak temperatures) with a similar initiation temperature. Noting that different cooling rates alter the process duration, and this factor is hidden on the x-axis, the overall amount of heat released over time is similar. For different temperature rates, the heat of fusion and absorbed heat over melting for the PCM modified bitumen are approximately 44 ± 1 J/g. This value correlates with analytical calculations as 25 wt.% of the blend containing PCM microcapsules with 195.5 J/g, so that the released heat is distributed within a larger mass of PCM modified bitumen material.

DSC ANALYSIS OF MATERIALS

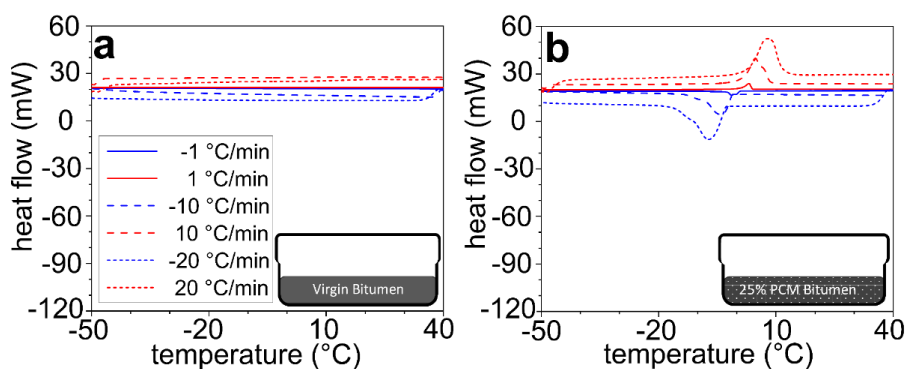


Figure C.6 **DSC analysis of the heat flow of the virgin and modified bitumen in environmentally dry condition (up, endothermic process)**. One thermal loop of each three temperature rates 1 °C/min, 10 °C/min and 20 °C/min is plotted for a) virgin bitumen. b) 25 wt.% PCM modified bitumen.

Figure C.7 demonstrates that the freezing temperature of the water is dependent of the cooling rate and that this occurs in the supercooled state of the water droplet, but melting is always initiated at 0 °C. It is also important to note

that the measured melting enthalpy is close to the reported 334 J/g at 0 °C value

153

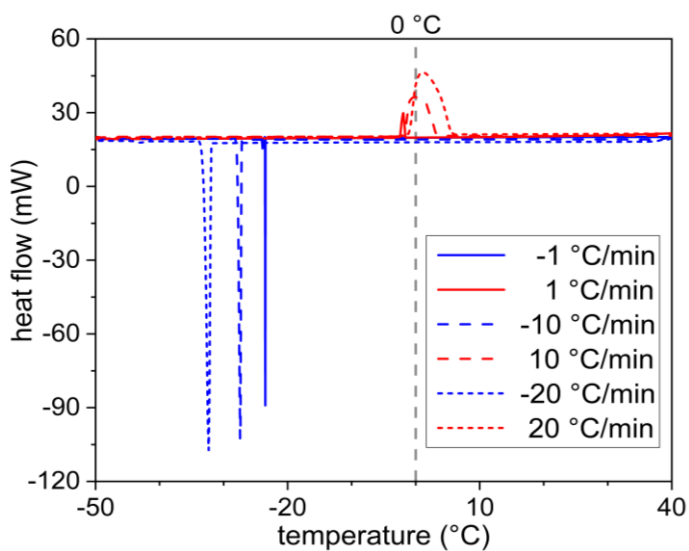


Figure C.7 **DSC results for a 1 mg single water droplet.** Three different temperature rates of 1 °C/min, 10 °C/min, and 20 °C/min. Cooling cycle after initial heating from 40 °C in blue and heating cycle plotted in red from -50 °C.

Water condensation freezing

CASCADE FREEZING OF SUPERCOOLED DROPLETS

Figure C.8a shows supercooled condensed droplets before freezing; then, suddenly, stable freezing nucleation forms in one of the supercooled droplets (recalescence freezing), and it becomes opaque (Figure C.8b). The freezing droplet then causes neighboring droplets to freeze (Figure C.8c), and the frozen area extends via cascade freezing (Figure C.8d-e).

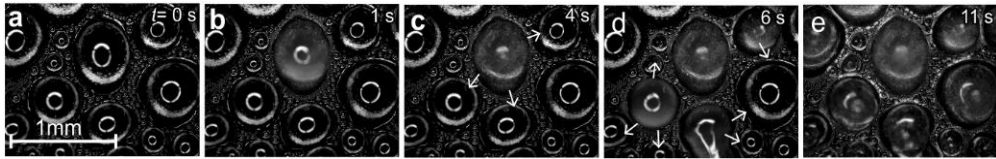


Figure C.8 **Recalescence and cascade freezing of supercooled droplets and freezing front spreading to cover the entire surface.** Optical microscopy view. a) Supercooled liquid droplet. b) One of the droplets becomes opaque after freezing nucleation. c) The frozen droplet initiates the freezing nucleation of neighboring droplets. d) Freezing front spreads. Arrows indicate the expanding freezing area direction.

COOLING RATE EFFECT ON CONDENSATION FREEZING

Figure C.9 provides image series corresponding to Figure 4.3 for the $RH = 50 \text{ wt.}\%$ ($T_{em} = 21.5 \pm 0.5 \text{ }^\circ\text{C}$) case at three cooling rates of $-1 \text{ }^\circ\text{C}/\text{min}$ (Figure C.9a), $-10 \text{ }^\circ\text{C}/\text{min}$ (Figure C.9b) and $-20 \text{ }^\circ\text{C}/\text{min}$ (Figure C.9c). The droplet sizes are large under slower cooling conditions of $-1 \text{ }^\circ\text{C}/\text{min}$ (Figure C.9a), and frost forms at a higher temperature.

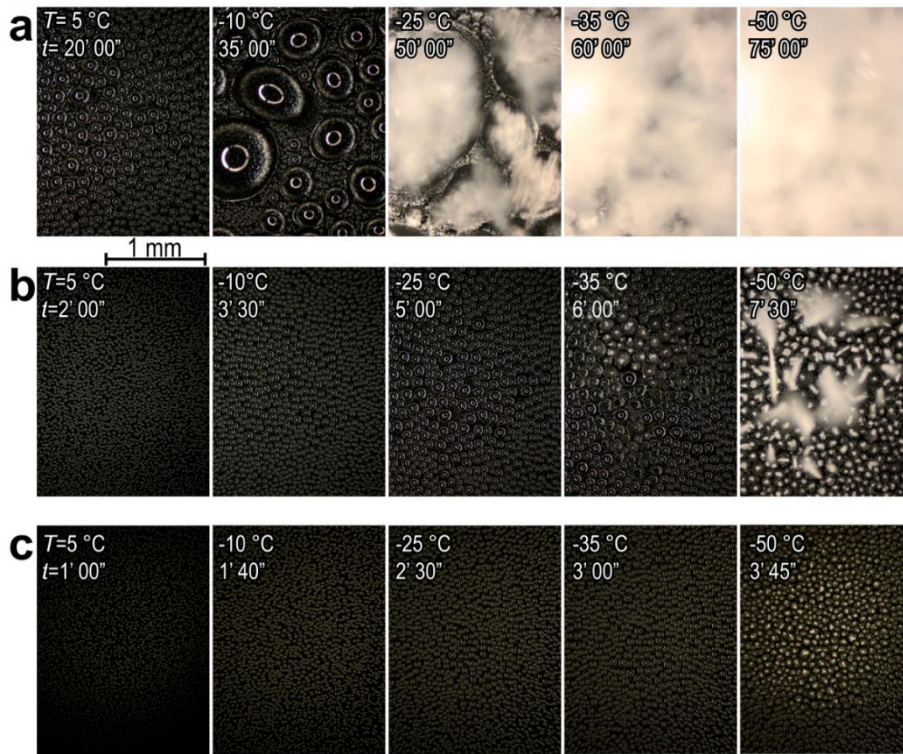


Figure C.9 The effect of cooling rate on condensation freezing for $RH = 50\%$. Temperature and time steps are synchronized under a similar initial $RH = 50\%$ condition at different cooling rates of a) $-1\text{ }^{\circ}\text{C}/\text{min}$ b) $-10\text{ }^{\circ}\text{C}/\text{min}$ and c) $-20\text{ }^{\circ}\text{C}/\text{min}$.

Supporting Videos

Video C.1 **Condensation freezing on virgin bitumen surface.** Environmental $RH=50\%$ ($T_{env} = 21.5 \pm 0.5$ °C), cooling at -20 °C/min from 25 °C to -50 °C and waiting 2 minutes at -50 °C, under an optical microscope in dark field at 5X magnification. The red circle shows the location of the cold pin, and the blue circle (from $T=-37$ °C frame) highlights the initial freezing droplet. Video captured at 5 fps and the clock shows real time. Playback speed changes depending on the state of condensation freezing.

Video C.2 **Ice bridging on virgin bitumen surface.** Environmental $RH=50\%$ ($T_{env} = 21.5 \pm 0.5$ °C), cooling at -20 °C/min, cooling at -20 °C/min from 25 °C to -50 °C, under an optical microscope in bright field at 100X magnification. Captured at 10 fps, playback video at 1/3 real time for limited temperature range of -36 °C to -41 °C.

Video C.3 **Thermal imaging on virgin bitumen surface.** Environmental $RH=50\%$ ($T_{env} = 21.5 \pm 0.5$ °C), cooling at -1 °C/min, from 25 °C to -35 °C. Captured by IR camera at 2 fps, playback 5 times faster than real time.

APPENDIX D

Bitumen is a complex material with temperature-dependent viscoelastic mechanical properties. Figure D1a shows plots of the complex modulus of bitumen vs. frequency using a dynamic shear rheometer (DSR; Physica MCR 301 DSR, Anton Paar® GmbH, Austria). The bitumen that was used was virgin Q8 70/100 bitumen, and the frequency sweep was done from 0.1 to 20 Hz for temperatures of -10 °C, 0 °C, 10 °C, 20 °C, 30 °C (Figure D1b).

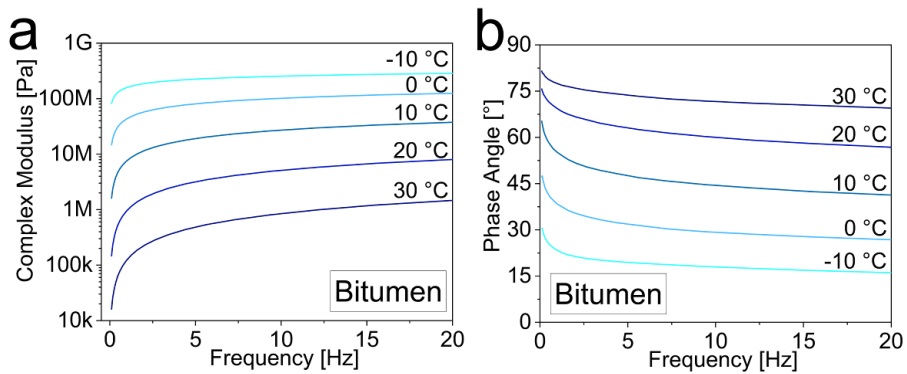


Figure D1 **Dynamic shear rheometer results of bitumen over frequency sweep at different temperatures.** a) Complex modulus vs. frequency of for various temperatures. b) Phase angle vs. frequency for various temperatures.

Figure D2 shows that the surface roughness features are in the microscale range.

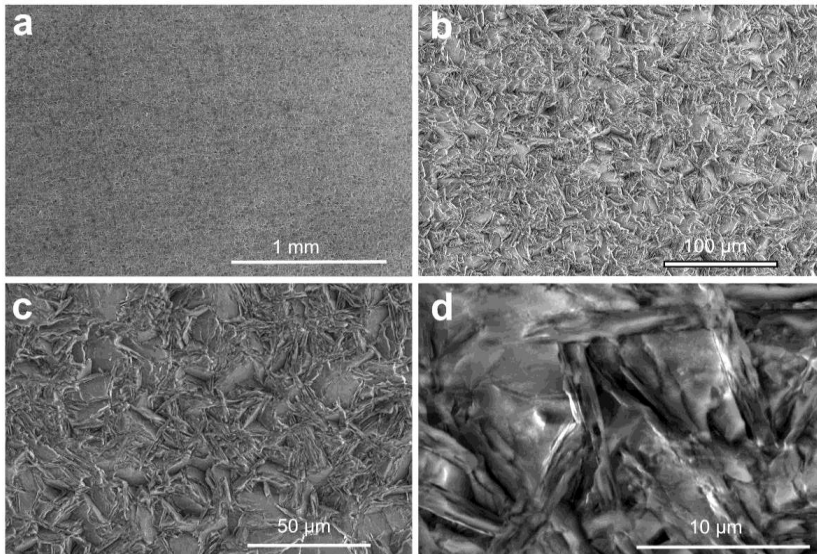


Figure D2 **Surface topography of Macor®.** a)-d) SEM micrographs of the untreated Macor® surface used in the study. Magnification increases from (a) to (d).

Figure D3 shows an example surface topography of Macor® measured by a profilometer, and we found that the root-mean-square (RMS) surface roughness was $0.34 \pm 0.04 \mu\text{m}$ (average of five separate measurements).

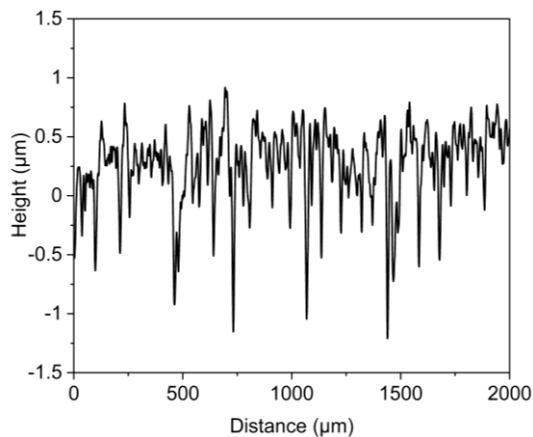


Figure D3 **Surface roughness of Macor®.** A single linear profilometry scan of the untreated Macor® surface used in this study. We did five separate linear scans that were 2 mm long, and we found that the average RMS roughness was $0.34 \pm 0.04 \mu\text{m}$.

In comparison, X. Gan *et al.* have reported that the RMS surface roughness of aggregates used in pavement is in the range of $\sim 25 \mu\text{m}$ to $\sim 34 \mu\text{m}$ (Gan, 2017; see Table A1). For cold regions application, researchers characterized similar aggregates and found that they had RMS surface roughness values of $\sim 6 \mu\text{m}$ (granite) and $\sim 7 \mu\text{m}$ (gabbro)¹⁸⁸. So while the RMS surface roughness of untreated Macor® is smaller than that of aggregates used in cold regions, we also found that by treating Macor® with a superhydrophobic coating the ice adhesion stress was reduced. Also, if the aggregates are treated to be superhydrophobic, water will not penetrate through the surface for the larger roughnesses typical of the aggregates mentioned above. Hence, in this case the effect of roughness on adhesion is expected to be minor.

Table A1 Comparison of surface roughness from various aggregates and Macor®.

Rock type	Macor®	Granite	Gabbro	Limestone	Basalt
RMS roughness [μm] (references)	0.34 ± 0.04	29.00 ¹⁸⁹	33.87 ¹⁸⁹	32.06 ¹⁸⁹	24.84 ¹⁸⁹
		6.35 ± 0.90 ¹⁸⁸	7.21 ± 0.67 ¹⁸⁸		

As it is not possible to cut the Macor® substrate, we cast bitumen on the same geometry glass coverslip. Cross-section of solvent cast bitumen on circular 18 mm diameter glass coverslip shows uniform thickness far away from the sample edge. Here we show cross-section images of a bitumen coating with a thickness of ca. $225 \mu\text{m}$ on a glass coverslip (Figure D4a) and superhydrophobic coated circular 18 mm diameter Macor® with a coating thickness of ca. $25 \mu\text{m}$ (Figure D4b).

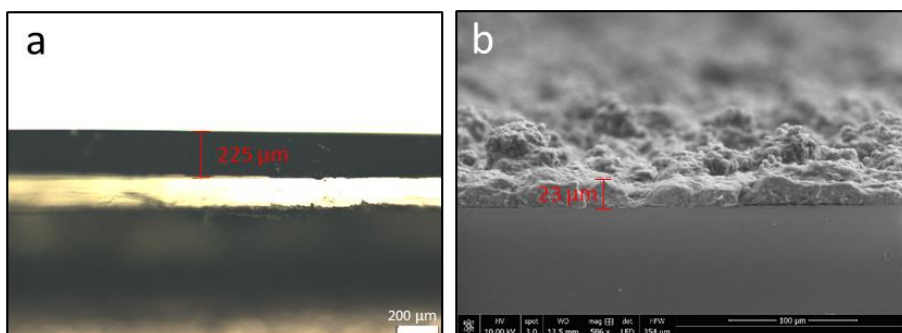


Figure D4 **Thickness analysis of bitumen and superhydrophobic coating.** a) Cross-sectional image of a bitumen coating on glass coverslip revealing its thickness. b) Scanning electron micrograph showing a view of a superhydrophobic coating Macor®.

Figure D5 depicts the contact angle measurement setup. A homemade environmental chamber equipped with a thermoelectric temperature stage and inlet nitrogen to keep environmental condition dry ($RH < 1\%$) at 24 ± 1 °C. The homemade chamber is installed on a commercial goniometer apparatus (OCA35, DataPhysics Instruments GmbH) which only the camera, syringe, and light source are shown in Figure D5.

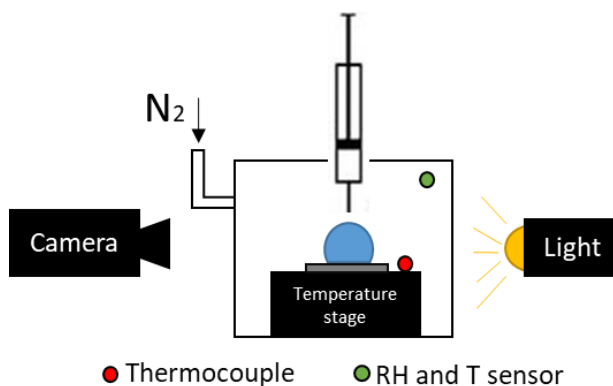


Figure D5 **Contact angle measurement setup.** Schematic drawing of an environmental chamber with nitrogen inlet to control RH and thermoelectric modulus installed as temperature stage to control the sample temperature. Green dot shows the location of the environmental temperature and RH and T sensor and red dot shows the location of a thermocouple attached to the stage to measure the sample temperature. The environmental chamber is installed on a commercial goniometer apparatus which camera, syringe, and light source are belonged.

Custom build ice adhesion setup is shown in Figure D6a, b. It consists of four main sections: 1-cryogenic stage, liquid nitrogen reservoir, and its controller, 2- transparent environmental chamber with inlet N_2 to provide the dry experimental ambient condition, 3- Mark-10 model M5-5 force sensor connected to a rod to apply/record force. 4- NRT150/M linear stage from Thorlabs for constant velocity movements of the force sensor.

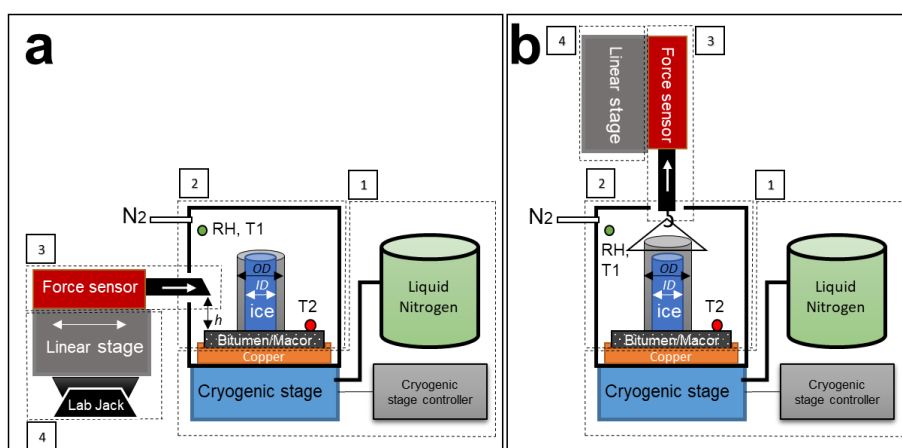


Figure D6 **Schematic drawing of the ice adhesion experimental setup.** a) For pure shear and combined stresses experiments, b) for normal-tension stress experiments. The cryogenic stage setup controls temperature (1), the chamber keeps the environmental $RH < 1\%$ condition in control, the green dot shows the location of the environmental temperature ($T1$) and RH sensor, and the red dot shows the location of a T-type thermocouple which reads the sample surface temperature. (2), the force sensor measures and records the force (3). The linear stage provides constant velocity to apply force for ice adhesion measurements (4) and lab jack to change the applied force height h for pure shear and combined stresses experiments.

To form ice, a water column (volume $\sim 25 \mu\text{l}$) was gently placed on the test surface, which is then cooled down to $-20 \text{ }^\circ\text{C}$. Figure D7b shows the water column on the bitumen surface. Figure D7c shows the water column freezing, and Figure D7d shows it after it has completely frozen. We see that ice nucleation starts from the liquid-substrate interface and propagates upwards. After several minutes, the entire column freezes. Figure D7d shows that the ice is cloudy, which we attribute

to small bubbles that form naturally during freezing. We note that we did not detect any large, trapped air pockets.

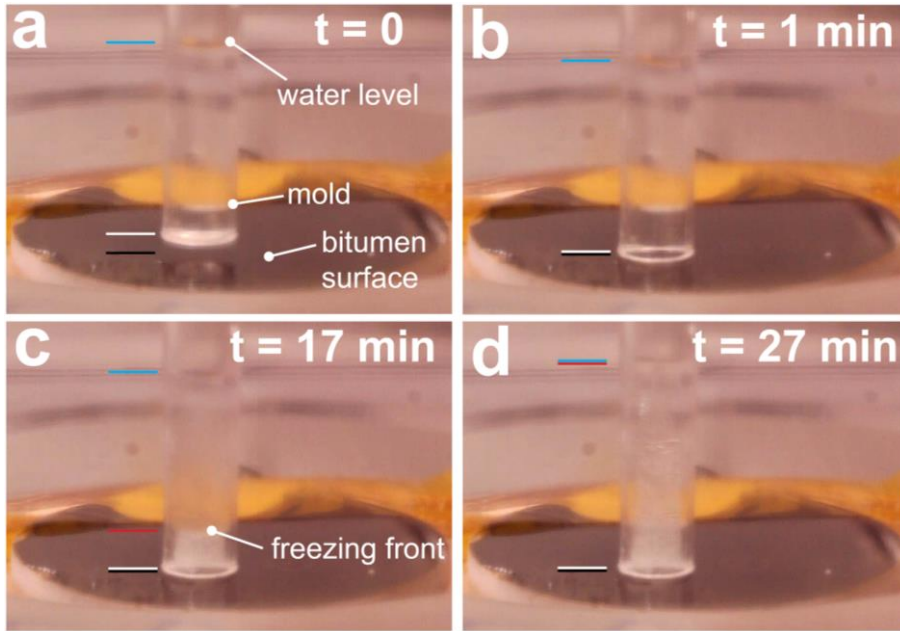


Figure D7 **Forming ice for ice adhesion experiments.** a) The mold is filled with water and is placed in contact with bitumen. Lines shown: bitumen surface (—), bottom of water mold (white line) and the water level (—). b) The water column is placed in contact with the bitumen surface. c) The substrate is cooled and the water starts to freeze (opaque). The freezing front propagates upwards from the bottom (—). d) The water column is completely frozen and is opaque, indicating the presence of tiny bubbles.

Figure D8a shows top-view schematics of ice mold on composite samples in two parallel and perpendicular directions to the applied force. For studying the impact of the material order, the ice mold was placed on the boundary of rigid-soft materials where the notch size is 1.8 mm (Figure D8b). We repeated the material order experiments on superhydrophobic coated Macor® samples.

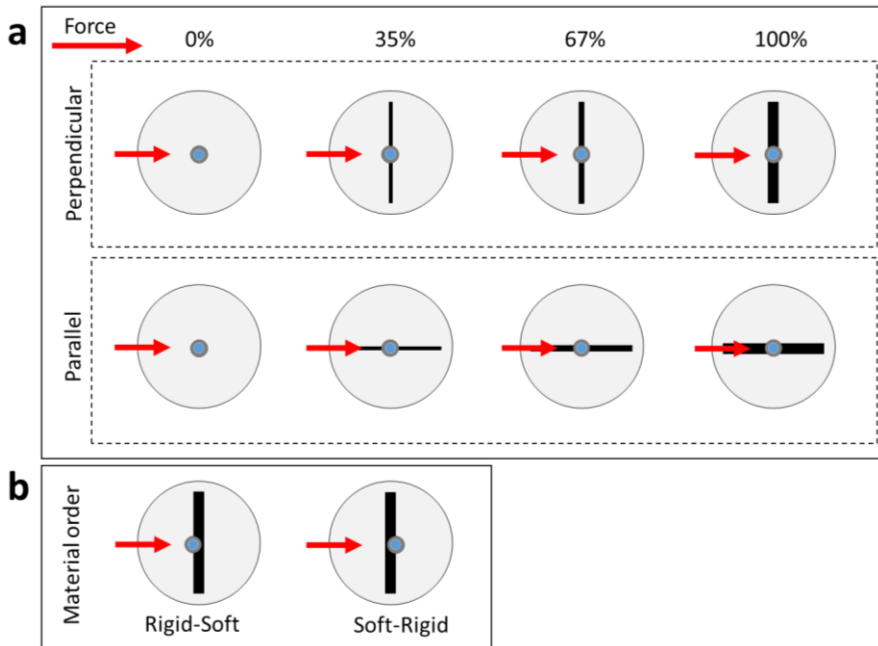


Figure D8 **Bitumen stripe and applied force directions for ice adhesion measurements on bituminous substrates.** a) Sample direction for two directions of the bitumen stripe when is perpendicular or parallel with respect to the applied force. Schematics show bitumen stripe width at three area fraction percentages ϕ regarding 35%, 67%, and 100% of iced area coverage. b) Schematic drawing of placing samples on the boundaries of 1.8 mm bitumen stripe with Macor®, when Macro® is first material with respect to the applied force or the opposite.

7 BIBLIOGRAPHY

- (1) ANDREY, J.; OLLEY, R. Relationships between Weather and Road Safety : Past and Future Research Directions. *Climatol. Bull.* **1990**, *24* (3), 123–137.
- (2) Yao, Y.; Zhao, X.; Zhang, Y.; Chen, C.; Rong, J. Modeling of Individual Vehicle Safety and Fuel Consumption under Comprehensive External Conditions. *Transp. Res. Part D Transp. Environ.* **2020**, *79* (January), 102224. <https://doi.org/10.1016/j.trd.2020.102224>.
- (3) Kelting, D. L.; Laxson, C. L. *Review of Effects and Costs of Road De-Icing with Recommendations for Winter Road Management in the Adirondack Park*; Adirondack Watershed Institute: New York, NY, 2010.
- (4) Roads and Traffic Facts and Figures. *Swiss Federal Roads Office (FEDRO)*. 2013.
- (5) Juga, I.; Nurmi, P.; Hippi, M. Statistical Modelling of Wintertime Road Surface Friction. *Meteorol. Appl.* **2013**, *20* (3), 318–329. <https://doi.org/10.1002/met.1285>.
- (6) Giuliani, F.; Merusi, F.; Polacco, G.; Filippi, S.; Paci, M. Effectiveness of Sodium Chloride-Based Anti-Icing Filler in Asphalt Mixtures. *Constr. Build. Mater.* **2012**, *30*, 174–179. <https://doi.org/10.1016/j.conbuildmat.2011.12.036>.
- (7) Kuemmel, D.; Hanbali, R. *Accident Analysis of Ice Control Operations*; 1992.

-
- (8) Charola, A. E.; Rousset, B.; Bläuer, C. Deicing Salts: An Overview. In *4th International Conference on Salt Weathering of Buildings and Stone Sculptures*; 2017; p 16.
- (9) Judd, J. H. Lake Stratification Caused by Runoff from Street Deicing. *Water Res.* **1970**, *4* (8), 521–532. [https://doi.org/10.1016/0043-1354\(70\)90002-3](https://doi.org/10.1016/0043-1354(70)90002-3).
- (10) Dugan, H. A.; Bartlett, S. L.; Burke, S. M.; Doubek, J. P.; Krivak-Tetley, F. E.; Skaff, N. K.; Summers, J. C.; Farrell, K. J.; McCullough, I. M.; Morales-Williams, A. M.; Roberts, D. C.; Ouyang, Z.; Scordo, F.; Hanson, P. C.; Weathers, K. C. Salting Our Freshwater Lakes. *Proc. Natl. Acad. Sci.* **2017**, *114* (17), 4453–4458. <https://doi.org/10.1073/PNAS.1620211114>.
- (11) Bagampadde, U.; Isacson, U.; Kiggundu, B. M. Classical and Contemporary Aspects of Stripping in Bituminous Mixes. *Road Mater. Pavement Des.* **2004**, *5* (1), 7–43. <https://doi.org/10.1080/14680629.2004.9689961>.
- (12) Zhou, Z.; Li, H.; Liu, X.; He, W. Investigation of Sea Salt Erosion Effect on the Asphalt-Aggregate Interfacial System. *Int. J. Pavement Res. Technol.* **2020**, *13* (2), 145–153. <https://doi.org/10.1007/s42947-019-0095-2>.
- (13) Khan, A.; Redelius, P.; Kringos, N. Toward a New Experimental Method for Measuring Coalescence in Bitumen Emulsions: A Study of Two Bitumen Droplets. *Colloids Surfaces A Physicochem. Eng. Asp.* **2016**, *494*, 228–240. <https://doi.org/10.1016/j.colsurfa.2016.01.045>.
- (14) Sun, Y.; Wu, S.; Liu, Q.; Hu, J.; Yuan, Y.; Ye, Q. Snow and Ice Melting Properties of Self-Healing Asphalt Mixtures with Induction Heating and

- Microwave Heating. *Appl. Therm. Eng.* **2018**, *129*, 871–883.
<https://doi.org/10.1016/j.applthermaleng.2017.10.050>.
- (15) Yang, F.; Li, K.; Xiong, R.; Guan, B.; Zhao, H. Investigation on Deicing Property of Steel Wool Fiber-Reinforced Asphalt Mixture by Induction Heating. *Adv. Mater. Sci. Eng.* **2020**, *2020*, 1–10.
<https://doi.org/10.1155/2020/5250628>.
- (16) Liu, Z.; Yang, X.; Wang, Y.; Luo, S. Engineering Properties and Microwave Heating Induced Ice-Melting Performance of Asphalt Mixture with Activated Carbon Powder Filler. *Constr. Build. Mater.* **2019**, *197*, 50–62.
<https://doi.org/10.1016/j.conbuildmat.2018.11.094>.
- (17) Gao, J.; Guo, H.; Wang, X.; Wang, P.; Wei, Y.; Wang, Z.; Huang, Y.; Yang, B. Microwave Deicing for Asphalt Mixture Containing Steel Wool Fibers. *J. Clean. Prod.* **2019**, *206*, 1110–1122.
<https://doi.org/10.1016/j.jclepro.2018.09.223>.
- (18) Giuliani, F.; Merusi, F.; Polacco, G.; Filippi, S.; Paci, M. Effectiveness of Sodium Chloride-Based Anti-Icing Filler in Asphalt Mixtures. *Constr. Build. Mater.* **2012**, *30*, 174–179.
<https://doi.org/10.1016/j.conbuildmat.2011.12.036>.
- (19) Zhong, K.; Sun, M.; Chang, R. Performance Evaluation of High-Elastic/Salt-Storage Asphalt Mixture Modified with Mafilon and Rubber Particles. *Constr. Build. Mater.* **2018**, *193*, 153–161.
<https://doi.org/10.1016/j.conbuildmat.2018.10.185>.

-
- (20) Xiao, Q. Y.; Cui, H. J.; Li, N. L.; Zhang, C. L. Study on Ice Breaking on Crumbed Rubber Asphalt Pavement Based on Self-Stress Method. *Appl. Mech. Mater.* **2012**, 256–259 (PART 1), 1807–1812. <https://doi.org/10.4028/www.scientific.net/AMM.256-259.1807>.
- (21) Wei, H.; He, Q.; Jiao, Y.; Chen, J.; Hu, M. Evaluation of Anti-Icing Performance for Crumb Rubber and Diatomite Compound Modified Asphalt Mixture. *Constr. Build. Mater.* **2016**, 107, 109–116. <https://doi.org/10.1016/j.conbuildmat.2016.01.003>.
- (22) Chunxiu, Z.; Yiqiu, T. Study on Anti-Icing Performance of Pavement Containing a Granular Crumb Rubber Asphalt Mixture. *Road Mater. Pavement Des.* **2009**, 10 (SI), 281–294. <https://doi.org/10.3166/rmpd.10hs.281-294>.
- (23) Farnam, Y.; Krafcik, M.; Liston, L.; Washington, T.; Erk, K.; Tao, B.; Weiss, J. Evaluating the Use of Phase Change Materials in Concrete Pavement to Melt Ice and Snow. *J. Mater. Civ. Eng.* **2016**, 28 (4). [https://doi.org/10.1061/\(ASCE\)MT.1943-5533.0001439](https://doi.org/10.1061/(ASCE)MT.1943-5533.0001439).
- (24) Chen, M.; Wan, L.; Lin, J. Effect of Phase-Change Materials on Thermal and Mechanical Properties of Asphalt Mixtures. *J. Test. Eval.* **2012**, 40 (5), 20120091. <https://doi.org/10.1520/jte20120091>.
- (25) Refaa, Z.; Kakar, M. R.; Stamatidou, A.; Worlitschek, J.; Partl, M. N.; Bueno, M. Numerical Study on the Effect of Phase Change Materials on Heat Transfer in Asphalt Concrete. *Int. J. Therm. Sci.* **2018**, 133 (March), 140–150. <https://doi.org/10.1016/j.ijthermalsci.2018.07.014>.

- (26) Li, F.; Zhou, S.; Chen, S.; Yang, J.; Zhu, X.; Du, Y.; Yang, Z. Low-Temperature Organic Phase Change Material Microcapsules for Asphalt Pavement: Preparation, Characterisation and Application. *J. Microencapsul.* **2018**, *35* (7–8), 635–642. <https://doi.org/10.1080/02652048.2018.1559248>.
- (27) Bueno, M.; Kakar, M. R.; Refaa, Z.; Worlitschek, J.; Stamatiou, A.; Partl, M. N. Modification of Asphalt Mixtures for Cold Regions Using Microencapsulated Phase Change Materials. *Sci. Rep.* **2019**, *9* (1), 20342. <https://doi.org/10.1038/s41598-019-56808-x>.
- (28) Zhou, X.; Kastiukas, G.; Lantieri, C.; Tataranni, P.; Vaiana, R.; Sangiorgi, C. Mechanical and Thermal Performance of Macro-Encapsulated Phase Change Materials for Pavement Application. *Materials (Basel)*. **2018**, *11* (8), 1–18. <https://doi.org/10.3390/ma11081398>.
- (29) Gao, Y.; Qu, L.; He, B.; Dai, K.; Fang, Z.; Zhu, R. Study on Effectiveness of Anti-Icing and Deicing Performance of Super-Hydrophobic Asphalt Concrete. *Constr. Build. Mater.* **2018**, *191*, 270–280. <https://doi.org/10.1016/j.conbuildmat.2018.10.009>.
- (30) Arabzadeh, A.; Ceylan, H.; Kim, S.; Gopalakrishnan, K.; Sassani, A. Fabrication of Polytetrafluoroethylene-Coated Asphalt Concrete Biomimetic Surfaces: A Nanomaterials-Based Pavement Winter Maintenance Approach. *Int. Conf. Transp. Dev. 2016* **2016**, No. July, 54–64. <https://doi.org/10.1061/9780784479926.006>.
- (31) Arabzadeh, A.; Ceylan, H.; Kim, S.; Gopalakrishnan, K.; Sassani, A.

- Superhydrophobic Coatings on Asphalt Concrete Surfaces. *Transp. Res. Rec. J. Transp. Res. Board* **2016**, *2551* (January), 10–17. <https://doi.org/10.3141/2551-02>.
- (32) Peng, C.; Chen, P.; You, Z.; Lv, S.; Xu, F.; Zhang, W.; Yu, J.; Zhang, H. The Anti-Icing and Mechanical Properties of a Superhydrophobic Coating on Asphalt Pavement. *Constr. Build. Mater.* **2018**, *190*, 83–94. <https://doi.org/10.1016/j.conbuildmat.2018.09.128>.
- (33) Read, J.; Whiteoak, D. *The Shell Bitumen Handbook, 5th Edition*, 5th ed.; Thomas Telford Ltd: London, 2003. <https://doi.org/10.1680/sbh.32200>.
- (34) Sörensen, A.; Wichert, B. Asphalt and Bitumen. *Ullmann's Encycl. Ind. Chem.* **2009**. https://doi.org/10.1002/14356007.a03_169.pub2.
- (35) Boulangé, L.; Bonin, E.; Saubot, M. Physicochemical Characterisations of the Bitumen-Aggregate Interface to Get a Better Understanding of Stripping Phenomena. *Road Mater. Pavement Des.* **2013**, *14* (2), 384–403. <https://doi.org/10.1080/14680629.2013.803494>.
- (36) Cui, S.; Blackman, B. R. K.; Kinloch, A. J.; Taylor, A. C. Durability of Asphalt Mixtures: Effect of Aggregate Type and Adhesion Promoters. *Int. J. Adhes. Adhes.* **2014**, *54*, 100–111. <https://doi.org/10.1016/j.ijadhadh.2014.05.009>.
- (37) Cala, A.; Caro, S.; Lleras, M.; Rojas-Agramonte, Y. Impact of the Chemical Composition of Aggregates on the Adhesion Quality and Durability of Asphalt-Aggregate Systems. *Constr. Build. Mater.* **2019**, *216*, 661–672.

<https://doi.org/10.1016/j.conbuildmat.2019.05.030>.

- (38) MACOR® [http://psec.uchicago.edu/ceramics/MACOR Data Sheet.pdf](http://psec.uchicago.edu/ceramics/MACOR_Data_Sheet.pdf) (accessed Mar 29, 2021).
- (39) Lesueur, D. The Colloidal Structure of Bitumen: Consequences on the Rheology and on the Mechanisms of Bitumen Modification. *Adv. Colloid Interface Sci.* **2009**, *145* (1–2), 42–82. <https://doi.org/10.1016/j.cis.2008.08.011>.
- (40) Yu, X.; Burnham, N. A.; Tao, M. Surface Microstructure of Bitumen Characterized by Atomic Force Microscopy. *Adv. Colloid Interface Sci.* **2015**, *218*, 17–33. <https://doi.org/10.1016/j.cis.2015.01.003>.
- (41) Schmets, A.; Kringos, N.; Pauli, T.; Redelius, P.; Scarpas, T. On the Existence of Wax-Induced Phase Separation in Bitumen. *Int. J. Pavement Eng.* **2010**, *11* (6), 555–563. <https://doi.org/10.1080/10298436.2010.488730>.
- (42) Redelius, P.; Soenen, H. Relation between Bitumen Chemistry and Performance. *Fuel* **2015**, *140*, 34–43. <https://doi.org/10.1016/j.fuel.2014.09.044>.
- (43) Lu, X.; Langton, M.; Olofsson, P.; Redelius, P. Wax Morphology in Bitumen. *J. Mater. Sci.* **2005**, *40* (8), 1893–1900. <https://doi.org/10.1007/s10853-005-1208-4>.
- (44) Pauli, A. T.; Grimes, R. W.; Beemer, A. G.; Turner, T. F.; Branthaver, J. F. Morphology of Asphalts, Asphalt Fractions and Model Wax-Doped

- Asphalts Studied by Atomic Force Microscopy. *Int. J. Pavement Eng.* **2011**, *12* (4), 291–309. <https://doi.org/10.1080/10298436.2011.575942>.
- (45) Nahar, S. N.; Schmets, A. J. M.; Scarpas, A.; Schitter, G. Temperature and Thermal History Dependence of the Microstructure in Bituminous Materials. *Eur. Polym. J.* **2013**, *49* (8), 1964–1974. <https://doi.org/10.1016/j.eurpolymj.2013.03.027>.
- (46) Sourty, E. D.; Tamminga, A. Y.; Michels, M. A. J.; Vellinga, W. P.; Meijer, H. E. H. The Microstructure of Petroleum Vacuum Residue Films for Bituminous Concrete: A Microscopy Approach. *J. Microsc.* **2011**, *241* (2), 132–146. <https://doi.org/10.1111/j.1365-2818.2010.03409.x>.
- (47) Fischer, H. R.; Dillingh, E. C.; Hermse, C. G. M. On the Microstructure of Bituminous Binders. *Road Mater. Pavement Des.* **2014**, *15* (1), 1–15. <https://doi.org/10.1080/14680629.2013.837838>.
- (48) Jacob N. Israelachvili. Intermolecular and Surface Forces. In *Intermolecular and Surface Forces*; Elsevier, 2011; p iii. <https://doi.org/10.1016/B978-0-12-391927-4.10024-6>.
- (49) Van Poel, C. Der. A General System Describing the Visco-Elastic Properties of Bitumens and Its Relation to Routine Test Data. *J. Appl. Chem.* **2007**, *4* (5), 221–236. <https://doi.org/10.1002/jctb.5010040501>.
- (50) MASSON, J.-F.; LEBLOND, V.; MARGESON, J. Bitumen Morphologies by Phase-Detection Atomic Force Microscopy. *J. Microsc.* **2006**, *221* (1), 17–29. <https://doi.org/10.1111/j.1365-2818.2006.01540.x>.

- (51) LOEBER, L.; SUTTON, O.; MOREL, J.; VALLETON, J.-M.; MULLER, G. New Direct Observations of Asphalts and Asphalt Binders by Scanning Electron Microscopy and Atomic Force Microscopy. *J. Microsc.* **1996**, *182* (1), 32–39. <https://doi.org/10.1046/j.1365-2818.1996.134416.x>.
- (52) Hung, A. M.; Fini, E. H. AFM Study of Asphalt Binder “Bee” Structures: Origin, Mechanical Fracture, Topological Evolution, and Experimental Artifacts. *RSC Adv.* **2015**, *5* (117), 96972–96982. <https://doi.org/10.1039/C5RA13982A>.
- (53) Fischer, H. R.; Dillingh, E. C. On the Investigation of the Bulk Microstructure of Bitumen – Introducing Two New Techniques. *Fuel* **2014**, *118* (1), 365–368. <https://doi.org/10.1016/j.fuel.2013.11.008>.
- (54) Ganter, D.; Franzka, S.; Shvartsman, V. V.; Lupascu, D. C. The Phenomenon of Bitumen ‘bee’ Structures–Bulk or Surface Layer–a Closer Look.’ *Int. J. Pavement Eng.* **2020**, *0* (0), 1–9. <https://doi.org/10.1080/10298436.2020.1823390>.
- (55) de Gennes, P.-G.; Brochard-Wyart, F.; Quéré, D. Capillarity and Gravity. In *Capillarity and Wetting Phenomena*, Springer New York: New York, NY, 2004; pp 33–67. https://doi.org/10.1007/978-0-387-21656-0_2.
- (56) Ruiz-Cabello, F. J. M.; Kusumaatmaja, H.; Rodríguez-Valverde, M. a.; Yeomans, J.; Cabrerizo-Vílchez, M. a. Modeling the Corrugation of the Three-Phase Contact Line Perpendicular to a Chemically Striped Substrate. *Langmuir* **2009**, *25* (9), 8357–8361. <https://doi.org/10.1021/la900579s>.

- (57) Shirtcliffe, N. J.; McHale, G.; Newton, M. I. Learning from Superhydrophobic Plants: The Use of Hydrophilic Areas on Superhydrophobic Surfaces for Droplet Control. *Langmuir* **2009**, *25* (24), 14121–14128. <https://doi.org/10.1021/la901557d>.
- (58) Choi, W.; Tuteja, A.; Mabry, J. M.; Cohen, R. E.; McKinley, G. H. A Modified Cassie-Baxter Relationship to Explain Contact Angle Hysteresis and Anisotropy on Non-Wetting Textured Surfaces. *J. Colloid Interface Sci.* **2009**, *339* (1), 208–216. <https://doi.org/10.1016/j.jcis.2009.07.027>.
- (59) Barthlott, W.; Neinhuis, C. Purity of the Sacred Lotus, or Escape from Contamination in Biological Surfaces. *Planta* **1997**, *202*, 1–8. <https://doi.org/10.1007/s004250050096>.
- (60) Yang, S.; Ju, J.; Qiu, Y.; He, Y.; Wang, X.; Dou, S.; Liu, K.; Jiang, L. Peanut Leaf Inspired Multifunctional Surfaces. *Small* **2014**, *10* (2), 294–299. <https://doi.org/10.1002/sml.201301029>.
- (61) Neinhuis, C. Characterization and Distribution of Water-Repellent, Self-Cleaning Plant Surfaces. *Ann. Bot.* **1997**, *79* (6), 667–677. <https://doi.org/10.1006/anbo.1997.0400>.
- (62) Ensikat, H. J.; Ditsche-Kuru, P.; Neinhuis, C.; Barthlott, W. Superhydrophobicity in Perfection: The Outstanding Properties of the Lotus Leaf. *Beilstein J. Nanotechnol.* **2011**, *2*, 152–161. <https://doi.org/10.3762/bjnano.2.19>.
- (63) Koch, K.; Barthlott, W. Superhydrophobic and Superhydrophilic Plant

- Surfaces: An Inspiration for Biomimetic Materials. *Philos. Trans. R. Soc. A Math. Phys. Eng. Sci.* **2009**, *367* (1893), 1487–1509. <https://doi.org/10.1098/rsta.2009.0022>.
- (64) Cassie, A. B. D.; Baxter, S. WETTABILITY OF POROUS SURFACES. **1944**, No. 5, 546–551.
- (65) Wenzel, R. N. Resistance of Solid Surfaces to Wetting by Water. *J. Ind. Eng. Chem. (Washington, D. C.)* **1936**, *28*, 988–994. <https://doi.org/10.1021/ie50320a024>.
- (66) Zellmer, S.; Lindenau, M.; Michel, S.; Garnweitner, G.; Schilde, C. Influence of Surface Modification on Structure Formation and Micromechanical Properties of Spray-Dried Silica Aggregates. *J. Colloid Interface Sci.* **2016**, *464*, 183–190. <https://doi.org/10.1016/j.jcis.2015.11.028>.
- (67) Hobbs, P. V. *Ice Physics*; Oxford classic texts in the physical sciences; New York: Oxford University Press, 2010.
- (68) Michael J. Moran, Howard N. Shapiro, Daisie D. Boettner, M. B. B. *Fundamentals of Engineering Thermodynamics, 9th Edition*; Wiley; 9th edition, 2018.
- (69) Water Phase Diagram <https://courses.lumenlearning.com/cheminter/chapter/phase-diagram-for-water/> (accessed Mar 29, 2021).
- (70) Makkonen, L. Surface Melting of Ice. *J. Phys. Chem. B* **1997**, *101* (32), 6196–

6200. <https://doi.org/10.1021/jp963248c>.
- (71) Makkonen, L. Ice Adhesion - Theory, Measurements and Countermeasures. *J. Adhes. Sci. Technol.* **2012**, *26* (4–5), 413–445. <https://doi.org/10.1163/016942411X574583>.
- (72) Meuler, A. J.; Smith, J. D.; Varanasi, K. K.; Mabry, J. M.; McKinley, G. H.; Cohen, R. E. Relationships between Water Wettability and Ice Adhesion. *ACS Appl. Mater. Interfaces* **2010**, *2* (11), 3100–3110. <https://doi.org/10.1021/am1006035>.
- (73) Mittal, K. L. Adhesion Measurement of Thin Films. *Electrocompon. Sci. Technol.* **1976**, *3* (1), 21–42. <https://doi.org/10.1155/APEC.3.21>.
- (74) Hejazi, V.; Sobolev, K.; Nosonovsky, M. From Superhydrophobicity to Icephobicity: Forces and Interaction Analysis. *Sci. Rep.* **2013**, *3*. <https://doi.org/10.1038/srep02194>.
- (75) Nosonovsky, M.; Hejazi, V. Why Superhydrophobic Surfaces Are Not Always Icephobic. **2012**. <https://doi.org/10.1021/nn302138r>.
- (76) Kulinich, S. A.; Farzaneh, M. Alkylsilane Self-Assembled Monolayers: Modeling Their Wetting Characteristics. *Appl. Surf. Sci.* **2004**, *230* (1–4), 232–240. <https://doi.org/10.1016/j.apsusc.2004.02.031>.
- (77) Guo, P.; Zheng, Y.; Wen, M.; Song, C.; Lin, Y.; Jiang, L. Icephobic/Anti-Icing Properties of Micro/Nanostructured Surfaces. *Adv. Mater.* **2012**, *24* (19), 2642–2648. <https://doi.org/10.1002/adma.201104412>.

- (78) Jung, S.; Tiwari, M. K.; Doan, N. V.; Poulikakos, D. Mechanism of Supercooled Droplet Freezing on Surfaces. *Nat. Commun.* **2012**, *3* (1), 615. <https://doi.org/10.1038/ncomms1630>.
- (79) Jung, S.; Dorrestijn, M.; Raps, D.; Das, A.; Megaridis, C. M.; Poulikakos, D. Are Superhydrophobic Surfaces Best for Icephobicity? **2011**, *27*, 3059–3066. <https://doi.org/10.1021/la104762g>.
- (80) Kim, P.; Wong, T. S.; Alvarenga, J.; Kreder, M. J.; Adorno-Martinez, W. E.; Aizenberg, J. Liquid-Infused Nanostructured Surfaces with Extreme Anti-Ice and Anti-Frost Performance. *ACS Nano* **2012**, *6* (8), 6569–6577. <https://doi.org/10.1021/nn302310q>.
- (81) Menini, R.; Farzaneh, M. Elaboration of Al₂O₃/PTFE Icephobic Coatings for Protecting Aluminum Surfaces. *Surf. Coatings Technol.* **2009**, *203* (14), 1941–1946. <https://doi.org/10.1016/j.surfcoat.2009.01.030>.
- (82) Meuler, A. J.; Smith, J. D.; Varanasi, K. K.; Mabry, J. M.; McKinley, G. H.; Cohen, R. E. Relationships between Water Wettability and Ice Adhesion. *ACS Appl. Mater. Interfaces* **2010**, *2* (11), 3100–3110. <https://doi.org/10.1021/am1006035>.
- (83) Schutzius, T. M.; Jung, S.; Maitra, T.; Graeber, G.; Köhme, M.; Poulikakos, D. Spontaneous Droplet Trampolining on Rigid Superhydrophobic Surfaces. *Nature* **2015**, *527* (7576), 82–85. <https://doi.org/10.1038/nature15738>.
- (84) Graeber, G.; Schutzius, T. M.; Eghlidi, H.; Poulikakos, D. Spontaneous Self-

- Dislodging of Freezing Water Droplets and the Role of Wettability. *Proc. Natl. Acad. Sci.* **2017**, *114* (42), 11040–11045. <https://doi.org/10.1073/pnas.1705952114>.
- (85) Zhang, Y.; Anim-Danso, E.; Bekele, S.; Dhinojwala, A. Effect of Surface Energy on Freezing Temperature of Water. *ACS Appl. Mater. Interfaces* **2016**, *8* (27), 17583–17590. <https://doi.org/10.1021/acsami.6b02094>.
- (86) Kim, M. H.; Kim, H.; Lee, K. S.; Kim, D. R. Frosting Characteristics on Hydrophobic and Superhydrophobic Surfaces: A Review. *Energy Convers. Manag.* **2017**, *138*, 1–11. <https://doi.org/10.1016/j.enconman.2017.01.067>.
- (87) Kakar, M. R.; Hamzah, M. O.; Akhtar, M. N.; Saleh, J. M. Evaluating the Surface Free Energy and Moisture Sensitivity of Warm Mix Asphalt Binders Using Dynamic Contact Angle. *Adv. Civ. Eng.* **2019**, *2019*. <https://doi.org/10.1155/2019/9153603>.
- (88) Kakar, M. R.; Hamzah, M. O.; Akhtar, M. N.; Woodward, D. Surface Free Energy and Moisture Susceptibility Evaluation of Asphalt Binders Modified with Surfactant-Based Chemical Additive. *J. Clean. Prod.* **2016**, *112*, 2342–2353. <https://doi.org/10.1016/j.jclepro.2015.10.101>.
- (89) Lv, J.; Song, Y.; Jiang, L.; Wang, J. Bio-Inspired Strategies for Anti-Icing. *ACS Nano* **2014**, *8* (4), 3152–3169. <https://doi.org/10.1021/nn406522n>.
- (90) Wang, F.; Li, C.; Lv, Y.; Lv, F.; Du, Y. Ice Accretion on Superhydrophobic Aluminum Surfaces under Low-Temperature Conditions. *Cold Reg. Sci. Technol.* **2010**, *62* (1), 29–33.

<https://doi.org/10.1016/j.coldregions.2010.02.005>.

- (91) Heydari, G.; Thormann, E.; Järn, M.; Tyrode, E.; Claesson, P. M. Hydrophobic Surfaces: Topography Effects on Wetting by Supercooled Water and Freezing Delay. *J. Phys. Chem. C* **2013**, *117* (42), 21752–21762. <https://doi.org/10.1021/jp404396m>.
- (92) Eberle, P.; Tiwari, M. K.; Maitra, T.; Poulikakos, D.; Spangenberg, B.; Kurz, H.; Ralston, J.; Bilgram, J.; Roth, R.; Dosch, H.; Vinciguerra, A. J.; Stephens, B.; Blohm, M. L. Rational Nanostructuring of Surfaces for Extraordinary Icephobicity. *Nanoscale* **2014**, *6* (9), 4874–4881. <https://doi.org/10.1039/C3NR06644D>.
- (93) Jung, S.; Tiwari, M. K.; Poulikakos, D. Frost Halos from Supercooled Water Droplets. *Proc. Natl. Acad. Sci. U. S. A.* **2012**, *109* (40), 16073–16078. <https://doi.org/10.1073/pnas.1206121109>.
- (94) Vasileiou, T.; Gerber, J.; Prautzsch, J.; Schutzius, T. M.; Poulikakos, D. Superhydrophobicity Enhancement through Substrate Flexibility. *Proc. Natl. Acad. Sci.* **2016**, *113* (47), 201611631. <https://doi.org/10.1073/pnas.1611631113>.
- (95) Schutzius, T. M.; Jung, S.; Maitra, T.; Eberle, P.; Antonini, C.; Stamatopoulos, C.; Poulikakos, D. Physics of Icing and Rational Design of Surfaces with Extraordinary Icephobicity. *Langmuir* **2015**, *31* (17), 4807–4821. <https://doi.org/10.1021/la502586a>.
- (96) Loeber, L.; Muller, G.; Morel, J.; Sutton, O. Bitumen in Colloid Science: A

- Chemical, Structural and Rheological Approach. *Fuel* **1998**, 77 (13), 1443–1450. [https://doi.org/10.1016/S0016-2361\(98\)00054-4](https://doi.org/10.1016/S0016-2361(98)00054-4).
- (97) Hofko, B.; Maschauer, D.; Steiner, D.; Grothe, H.; Mirwald, J. Chemical Composition and Microstructure of Bitumen – a Matter of Terminology?; Springer, Cham, 2019; pp 145–149. https://doi.org/10.1007/978-3-030-00476-7_23.
- (98) Kané, M.; Djabourov, M.; Volle, J. L.; Lechaire, J. P.; Frebourg, G. Morphology of Paraffin Crystals in Waxy Crude Oils Cooled in Quiescent Conditions and under Flow. *Fuel* **2003**, 82 (2), 127–135. [https://doi.org/10.1016/S0016-2361\(02\)00222-3](https://doi.org/10.1016/S0016-2361(02)00222-3).
- (99) Zbik, M.; Horn, R. G.; Shaw, N. AFM Study of Paraffin Wax Surfaces. *Colloids Surfaces A Physicochem. Eng. Asp.* **2006**, 287 (1–3), 139–146. <https://doi.org/10.1016/j.colsurfa.2006.03.043>.
- (100) Isacsson, U.; Zeng, H. Relationships between Bitumen Chemistry and Low Temperature Behaviour of Asphalt. *Constr. Build. Mater.* **1997**, 11 (2), 83–91. [https://doi.org/10.1016/S0950-0618\(97\)00008-1](https://doi.org/10.1016/S0950-0618(97)00008-1).
- (101) Cavalli, M. C.; Zaumanis, M.; Mazza, E.; Partl, M. N.; Poulikakos, L. D. Effect of Ageing on the Mechanical and Chemical Properties of Binder from RAP Treated with Bio-Based Rejuvenators. *Compos. Part B Eng.* **2018**, 141 (May), 174–181. <https://doi.org/10.1016/j.compositesb.2017.12.060>.
- (102) Petersen, J. C. A Review of the Fundamentals of Asphalt Oxidation (E-C140). *Transp. Res. Rec. J. Transp. Res. Board* **2009**, E-C140 (October), 1–78.

<https://doi.org/10.17226/23002>.

- (103) Das, P. K.; Kringos, N.; Birgisson, B. Microscale Investigation of Thin Film Surface Ageing of Bitumen. *J. Microsc.* **2014**, *254* (2), 95–107. <https://doi.org/10.1111/jmi.12122>.
- (104) Masson, J. F.; Leblond, V.; Margeson, J.; Bundalo-Perc, S. Low-Temperature Bitumen Stiffness and Viscous Paraffinic Nano- and Micro-Domains by Cryogenic AFM and PDM. *J. Microsc.* **2007**, *227* (3), 191–202. <https://doi.org/10.1111/j.1365-2818.2007.01796.x>.
- (105) Mercé, M.; Saadaoui, H.; Dole, F.; Buisson, L.; Bentaleb, A.; Ruggi, D.; Schmitt, V.; Backov, R. Importance of Thermal Gradient in the Bitumen Bees Genesis. *J. Mater. Sci.* **2015**. <https://doi.org/10.1007/s10853-015-9202-y>.
- (106) Nahar, S.; Mohajeri, M.; Schmetts, A.; Scarpas, A.; van de Ven, M.; Schitter, G. First Observation of Blending-Zone Morphology at Interface of Reclaimed Asphalt Binder and Virgin Bitumen. *Transp. Res. Rec. J. Transp. Res. Board* **2013**, *2370* (December), 1–9. <https://doi.org/10.3141/2370-01>.
- (107) Lyne, Å. L.; Wallqvist, V.; Rutland, M. W.; Claesson, P.; Birgisson, B. Surface Wrinkling: The Phenomenon Causing Bees in Bitumen. *J. Mater. Sci.* **2013**, *48* (20), 6970–6976. <https://doi.org/10.1007/s10853-013-7505-4>.
- (108) Lesueur, D.; Gerard, J.; Claudy, P.; Letoffe, J.; Planche, J.; Martin, D. A Structure-related Model to Describe Asphalt Linear Viscoelasticity. *J. Rheol.*

- (N. Y. N. Y). **1996**, *40* (5), 813–836. <https://doi.org/10.1122/1.550764>.
- (109) Zhang, C.; Xu, T.; Shi, H.; Wang, L. Physicochemical and Pyrolysis Properties of SARA Fractions Separated from Asphalt Binder. *J. Therm. Anal. Calorim.* **2015**, *122* (1), 241–249. <https://doi.org/10.1007/s10973-015-4700-3>.
- (110) Speight, J. *The Desulfurization of Heavy Oils and Residua*; 1999. [https://doi.org/10.1016/0378-3820\(82\)90041-8](https://doi.org/10.1016/0378-3820(82)90041-8).
- (111) Shi, H.; Xu, T.; Zhou, P.; Jiang, R. Combustion Properties of Saturates, Aromatics, Resins, and Asphaltenes in Asphalt Binder. *Constr. Build. Mater.* **2017**, *136*, 515–523. <https://doi.org/10.1016/j.conbuildmat.2017.01.064>.
- (112) Claudy, P.; Letoffe, J. M.; King, G. N.; Planche, J. P.; Brule, B. Characterization of Paving Asphalts by Differential Scanning Calorimetry. *Fuel Sci. Technol. Int.* **1991**, *9* (1), 71–92. <https://doi.org/10.1080/08843759108942254>.
- (113) Masson, J. F.; Polomark, G. M.; Collins, P. Time-Dependent Microstructure of Bitumen and Its Fractions by Modulated Differential Scanning Calorimetry. *Energy and Fuels* **2002**, *16* (2), 470–476. <https://doi.org/10.1021/ef010233r>.
- (114) Masson, J. F.; Polomark, G. M.; Bundalo-Perc, S.; Collins, P. Melting and Glass Transitions in Paraffinic and Naphthenic Oils. *Thermochim. Acta* **2006**, *440* (2), 132–140. <https://doi.org/10.1016/j.tca.2005.11.001>.

- (115) Masson, J.-F. F.; Polomark, G. . M. Bitumen Microstructure by Modulated Differential Scanning Calorimetry. *Thermochim. Acta* **2001**, *374* (2), 105–114. [https://doi.org/10.1016/S0040-6031\(01\)00478-6](https://doi.org/10.1016/S0040-6031(01)00478-6).
- (116) Gong, M.; Yang, J.; Wei, J.; Pauli, T.; Yu, H. Quantitative Characterisation of Asphalt's Composition–Microstructure Relationship Based on Atomic Force Microscopy, Differential Scanning Calorimetry, and Fourier Transform Infrared Spectroscopy Tests. *Road Mater. Pavement Des.* **2017**, *18* (3), 507–532. <https://doi.org/10.1080/14680629.2016.1181560>.
- (117) Sjövall, P.; Pomerantz, A. E.; Lu, X.; Mullins, O. C. Time of Flight-Secondary Ion Mass Spectrometry (TOF-SIMS) Study of Diverse Asphaltenes. *Fuel* **2018**, *220* (February), 638–644. <https://doi.org/10.1016/j.fuel.2018.02.017>.
- (118) Lu, X.; Sjövall, P.; Soenen, H.; Andersson, M. Microstructures of Bitumen Observed by Environmental Scanning Electron Microscopy (ESEM) and Chemical Analysis Using Time-of-Flight Secondary Ion Mass Spectrometry (TOF-SIMS). *Fuel* **2018**, *229*, 198–208. <https://doi.org/10.1016/J.FUEL.2018.05.036>.
- (119) Lu, X.; Sjövall, P.; Soenen, H. Structural and Chemical Analysis of Bitumen Using Time-of-Flight Secondary Ion Mass Spectrometry (TOF-SIMS). *Fuel* **2017**, *199*, 206–218. <https://doi.org/10.1016/J.FUEL.2017.02.090>.
- (120) Fischer, H. R.; Cernescu, A. Relation of Chemical Composition to Asphalt Microstructure - Details and Properties of Micro-Structures in Bitumen as

- Seen by Thermal and Friction Force Microscopy and by Scanning near-Field Optical Microscopy. *Fuel* **2015**, *153*, 628–633. <https://doi.org/10.1016/j.fuel.2015.03.043>.
- (121) Dazzi, A.; Prater, C. B. AFM-IR: Technology and Applications in Nanoscale Infrared Spectroscopy and Chemical Imaging. *Chem. Rev.* **2017**, *117* (7), 5146–5173. <https://doi.org/10.1021/acs.chemrev.6b00448>.
- (122) Centrone, A. Infrared Imaging and Spectroscopy Beyond the Diffraction Limit. *Annu. Rev. Anal. Chem.* **2015**, *8* (1), 101–126. <https://doi.org/10.1146/annurev-anchem-071114-040435>.
- (123) Dazzi, A.; Prazeres, R.; Glotin, F.; Ortega, J. M. Analysis of Nano-Chemical Mapping Performed by an AFM-Based (“AFMIR”) Acousto-Optic Technique. *Ultramicroscopy* **2007**, *107* (12), 1194–1200. <https://doi.org/10.1016/j.ultramic.2007.01.018>.
- (124) Dazzi, A.; Prater, C. B.; Hu, Q.; Chase, D. B.; Rabolt, J. F.; Marcott, C. AFM – IR : Combining Atomic Force Microscopy and Infrared Spectroscopy for Nanoscale Chemical Characterization. *Appl. Spectrosc.* **2012**, *66* N62, 1365–1384. <https://doi.org/10.1366/12-06804>.
- (125) Dazzi, A.; Saunier, J.; Kjoller, K.; Yagoubi, N. Resonance Enhanced AFM-IR: A New Powerful Way to Characterize Blooming on Polymers Used in Medical Devices. *Int. J. Pharm.* **2015**, *484* (1–2), 109–114. <https://doi.org/10.1016/j.ijpharm.2015.02.046>.

- (126) Xing, C.; Liu, L.; Cui, Y.; Ding, D. Analysis of Base Bitumen Chemical Composition and Aging Behaviors via Atomic Force Microscopy-Based Infrared Spectroscopy. *Fuel* **2020**, *264* (December 2019), 116845. <https://doi.org/10.1016/j.fuel.2019.116845>.
- (127) De Moraes, M. B.; Pereira, R. B.; Simão, R. A.; Leite, L. F. M. High Temperature AFM Study of CAP 30/45 Pen Grade Bitumen. *J. Microsc.* **2010**, *239* (1), 46–53. <https://doi.org/10.1111/j.1365-2818.2009.03354.x>.
- (128) Das, P. K.; Kringos, N.; Wallqvist, V.; Birgisson, B. Micromechanical Investigation of Phase Separation in Bitumen by Combining Atomic Force Microscopy with Differential Scanning Calorimetry Results. *Road Mater. Pavement Des.* **2013**, *14* (SUPPL.1), 25–37. <https://doi.org/10.1080/14680629.2013.774744>.
- (129) Qin, Q.; Farrar, M. J.; Pauli, A. T.; Adams, J. J. Morphology, Thermal Analysis and Rheology of Sasobit Modified Warm Mix Asphalt Binders. *Fuel* **2014**, *115*, 416–425. <https://doi.org/10.1016/j.fuel.2013.07.033>.
- (130) Soenen, H.; Besamusca, J.; Fischer, H. R.; Poulidakos, L. D.; Planche, J.-P.; Das, P. K.; Kringos, N.; Grenfell, J. R. A.; Lu, X.; Chailleux, E. Laboratory Investigation of Bitumen Based on Round Robin DSC and AFM Tests. *Mater. Struct.* **2014**, *47* (7), 1205–1220. <https://doi.org/10.1617/s11527-013-0123-4>.
- (131) Biró, L. P. Atomic Force Microscopy Investigation of Carbon Nanotubes. In *Carbon Filaments and Nanotubes: Common Origins, Differing Applications?*; 2001;

- Vol. 46, pp 255–263. https://doi.org/10.1007/978-94-010-0777-1_18.
- (132) Chakraborty, I.; Yablon, D. G. Cantilever Energy Effects on Bimodal AFM: Phase and Amplitude Contrast of Multicomponent Samples. *Nanotechnology* **2013**, *24* (47). <https://doi.org/10.1088/0957-4484/24/47/475706>.
- (133) Aguiar-Moya, J. P.; Salazar-Delgado, J.; Bonilla-Mora, V.; Rodríguez-Castro, E.; Leiva-Villacorta, F.; Loría-Salazar, L. Morphological Analysis of Bitumen Phases Using Atomic Force Microscopy. *Road Mater. Pavement Des.* **2015**, *16*, 138–152. <https://doi.org/10.1080/14680629.2015.1029672>.
- (134) Das, P. K.; Jelagin, D.; Birgisson, B.; Kringos, N. Micro-Mechanical Investigation of Low Temperature Fatigue Cracking Behaviour of Bitumen. *7th RILEM Int. Conf. Crack. Pavements* **2012**, *4*, 1281–1290. https://doi.org/10.1007/978-94-007-4566-7_122.
- (135) ISO 11357-2: Plastics -- Differential scanning calorimetry (DSC) -- Part 2: Determination of glass transition temperature <https://www.iso.org/obp/ui/#iso:std:iso:11357:-2:ed-1:v1:en> (accessed Mar 29, 2021).
- (136) Hofko, B.; Porot, L.; Falchetto Cannone, A.; Poulidakos, L.; Huber, L.; Lu, X.; Mollenhauer, K.; Grothe, H. FTIR Spectral Analysis of Bituminous Binders: Reproducibility and Impact of Ageing Temperature. *Mater. Struct. Constr.* **2018**, *51* (2). <https://doi.org/10.1617/s11527-018-1170-7>.
- (137) Weigel, S.; Stephan, D. The Prediction of Bitumen Properties Based on FTIR and Multivariate Analysis Methods. *Fuel* **2017**, *208*, 655–661.

<https://doi.org/10.1016/j.fuel.2017.07.048>.

- (138) Lamontagne, J.; Dumas, P.; Mouillet, V.; Kister, J. Comparison by Fourier Transform Infrared (FTIR) Spectroscopy of Different Ageing Techniques: Application to Road Bitumens. *Fuel* **2001**, *80* (4), 483–488. [https://doi.org/10.1016/S0016-2361\(00\)00121-6](https://doi.org/10.1016/S0016-2361(00)00121-6).
- (139) Permanyer, A.; Douifi, L.; Lahcini, A.; Lamontagne, J.; Kister, J. FTIR and SUVF Spectroscopy Applied to Reservoir Compartmentalization: A Comparative Study with Gas Chromatography Fingerprints Results. *Fuel* **2002**, *81* (7), 861–866. [https://doi.org/10.1016/S0016-2361\(01\)00211-3](https://doi.org/10.1016/S0016-2361(01)00211-3).
- (140) Malin, F.; Norros, I.; Innamaa, S. Accident Risk of Road and Weather Conditions on Different Road Types. *Accid. Anal. Prev.* **2019**, *122* (February 2018), 181–188. <https://doi.org/10.1016/j.aap.2018.10.014>.
- (141) Usman, T.; Fu, L.; Miranda-Moreno, L. F. Quantifying Safety Benefit of Winter Road Maintenance: Accident Frequency Modeling. *Accid. Anal. Prev.* **2010**, *42* (6), 1878–1887. <https://doi.org/10.1016/j.aap.2010.05.008>.
- (142) Norrman, J.; Eriksson, M.; Lindqvist, S. Relationships between Road Slipperiness, Traffic Accident Risk and Winter Road Maintenance Activity. *Clim. Res.* **2000**, *15* (3), 185–193. <https://doi.org/10.3354/cr015185>.
- (143) Andersson, A. K.; Chapman, L. The Impact of Climate Change on Winter Road Maintenance and Traffic Accidents in West Midlands, UK. *Accid. Anal. Prev.* **2011**, *43* (1), 284–289. <https://doi.org/10.1016/j.aap.2010.08.025>.

-
- (144) Autelitano, F.; Rinaldi, M.; Giuliani, F. Winter Highway Maintenance Strategies: Are All the Sodium Chloride Salts the Same? *Constr. Build. Mater.* **2019**, *226*, 945–952. <https://doi.org/10.1016/j.conbuildmat.2019.07.292>.
- (145) Hassan, Y.; Abd El Halim, A. O.; Razaqpur, A. G.; Bekheet, W.; Farha, M. H. Effects of Runway Deicers on Pavement Materials and Mixes: Comparison with Road Salt. *J. Transp. Eng.* **2002**, *128* (4), 385–391. [https://doi.org/10.1061/\(ASCE\)0733-947X\(2002\)128:4\(385\)](https://doi.org/10.1061/(ASCE)0733-947X(2002)128:4(385)).
- (146) Shi, X.; Akin, M.; Pan, T.; Fay, L.; Liu, Y.; Yang, Z. Deicer Impacts on Pavement Materials: Introduction and Recent Developments. *Open Civ. Eng. J.* **2009**, *3* (1), 16–27. <https://doi.org/10.2174/1874149500903010016>.
- (147) Kakar, M. R.; Refaa, Z.; Worlitschek, J.; Stamatiou, A.; Partl, M. N.; Bueno, M. Effects of Aging on Asphalt Binders Modified with Microencapsulated Phase Change Material. *Compos. Part B Eng.* **2019**, *173* (June), 107007. <https://doi.org/10.1016/j.compositesb.2019.107007>.
- (148) Kakar, M. R.; Refaa, Z.; Bueno, M.; Worlitschek, J.; Stamatiou, A.; Partl, M. N. Investigating Bitumen's Direct Interaction with Tetradecane as Potential Phase Change Material for Low Temperature Applications. *Road Mater. Pavement Des.* **2019**, *0629*. <https://doi.org/10.1080/14680629.2019.1601127>.
- (149) Kakar, M. R.; Refaa, Z.; Worlitschek, J.; Stamatiou, A.; Partl, M. N.; Bueno, M. Thermal and Rheological Characterization of Bitumen Modified with Microencapsulated Phase Change Materials. *Constr. Build. Mater.* **2019**, *215*, 171–179. <https://doi.org/10.1016/j.conbuildmat.2019.04.171>.

- (150) Vali, G. Interpretation of Freezing Nucleation Experiments: Singular and Stochastic; Sites and Surfaces. *Atmos. Chem. Phys.* **2014**, *14* (11), 5271–5294. <https://doi.org/10.5194/acp-14-5271-2014>.
- (151) Suzuki, R. O.; Fujisaka, T.; Ito, K. O.; Meng, X.; Sui, H. T. Dimensional Analysis of Thermoelectric Modules Under Constant Heat Flux. *J. Electron. Mater.* **2015**, *44* (1), 348–355. <https://doi.org/10.1007/s11664-014-3314-z>.
- (152) Laird Thermal Systems
<https://www.lairdthermal.com/products/thermoelectric-cooler-modules/peltier-thermal-cycling-series/PC6-12-F1-4040-TA-W6> (accessed Nov 12, 2020).
- (153) Legates, D. R. Latent Heat. In *Encyclopedia of World Climatology*; Oliver, J. E., Ed.; Springer Netherlands: Dordrecht, 2005; pp 450–451. https://doi.org/10.1007/1-4020-3266-8_124.
- (154) Nath, S.; Ahmadi, S. F.; Boreyko, J. B. A Review of Condensation Frosting. *Nanoscale Microscale Thermophys. Eng.* **2017**, *21* (2), 81–101. <https://doi.org/10.1080/15567265.2016.1256007>.
- (155) Nath, S.; Boreyko, J. B. On Localized Vapor Pressure Gradients Governing Condensation and Frost Phenomena. *Langmuir* **2016**, *32* (33), 8350–8365. <https://doi.org/10.1021/acs.langmuir.6b01488>.
- (156) Nath, S.; Ahmadi, S. F.; Boreyko, J. B. How Ice Bridges the Gap. *Soft Matter* **2020**, *16* (5), 1156–1161. <https://doi.org/10.1039/c9sm01968e>.

- (157) Boreyko, J. B.; Collier, C. P. Delayed Frost Growth on Jumping-Drop Superhydrophobic Surfaces. *ACS Nano* **2013**, *7* (2), 1618–1627. <https://doi.org/10.1021/nn3055048>.
- (158) Graeber, G.; Dolder, V.; Schutzius, T. M.; Poulikakos, D. Cascade Freezing of Supercooled Water Droplet Collectives. *ACS Nano* **2018**, *12* (11), 11274–11281. <https://doi.org/10.1021/acsnano.8b05921>.
- (159) Chen, T.; Cong, Q.; Sun, C.; Jin, J.; Choy, K. L. Influence of Substrate Initial Temperature on Adhesion Strength of Ice on Aluminum Alloy. *Cold Reg. Sci. Technol.* **2018**, *148* (January), 142–147. <https://doi.org/10.1016/j.coldregions.2018.01.017>.
- (160) Rønneberg, S.; Xiao, S.; He, J.; Zhang, Z. Nanoscale Correlations of Ice Adhesion Strength and Water Contact Angle. *Coatings* **2020**, *10* (4), 379. <https://doi.org/10.3390/coatings10040379>.
- (161) Kulinich, S. A.; Farzaneh, M. How Wetting Hysteresis Influences Ice Adhesion Strength on Superhydrophobic Surfaces. *Langmuir* **2009**, *25* (16), 8854–8856. <https://doi.org/10.1021/la901439c>.
- (162) Work, A.; Lian, Y. A Critical Review of the Measurement of Ice Adhesion to Solid Substrates. *Prog. Aerosp. Sci.* **2018**, *98*, 1–26. <https://doi.org/10.1016/j.paerosci.2018.03.001>.
- (163) Matsumoto, K.; Kobayashi, T. Fundamental Study on Adhesion of Ice to Cooling Solid Surface. *Int. J. Refrig.* **2007**, *30* (5), 851–860. <https://doi.org/10.1016/j.ijrefrig.2006.11.009>.

- (164) Baker, H. R.; Bascom, W. D.; Singleterry, C. R. The Adhesion of Ice to Lubricated Surfaces. *J. Colloid Sci.* **1962**, *17* (5), 477–491. [https://doi.org/10.1016/0095-8522\(62\)90057-0](https://doi.org/10.1016/0095-8522(62)90057-0).
- (165) Wilson, P. W.; Lu, W.; Xu, H.; Kim, P.; Kreder, M. J.; Alvarenga, J.; Aizenberg, J. Inhibition of Ice Nucleation by Slippery Liquid-Infused Porous Surfaces (SLIPS). *Phys. Chem. Chem. Phys.* **2013**, *15* (2), 581–585. <https://doi.org/10.1039/c2cp43586a>.
- (166) Metya, A. K.; Singh, J. K. Ice Adhesion Mechanism on Lubricant-Impregnated Surfaces Using Molecular Dynamics Simulations. *Mol. Simul.* **2019**, *45* (4–5), 394–402. <https://doi.org/10.1080/08927022.2018.1513649>.
- (167) Petit, J.; Bonaccorso, E. General Frost Growth Mechanism on Solid Substrates with Different Stiffness. *Langmuir* **2014**, *30* (4), 1160–1168. <https://doi.org/10.1021/la404084m>.
- (168) Chung, J. Y.; Chaudhury, M. K. Soft and Hard Adhesion. *J. Adhes.* **2005**, *81* (10–11), 1119–1145. <https://doi.org/10.1080/00218460500310887>.
- (169) Chung, J. Y.; Kim, K. H.; Chaudhury, M. K.; Sarkar, J.; Sharma, A. Confinement-Induced Instability and Adhesive Failure between Dissimilar Thin Elastic Films. *Eur. Phys. J. E* **2006**, *20* (1), 47–53. <https://doi.org/10.1140/epje/i2005-10080-0>.
- (170) Chaudhury, M. K.; Kim, K. H. Shear-Induced Adhesive Failure of a Rigid Slab in Contact with a Thin Confined Film. *Eur. Phys. J. E* **2007**, *23* (2), 175–183. <https://doi.org/10.1140/epje/i2007-10171-x>.

- (171) Vasileiou, T.; Schutzius, T. M.; Poulikakos, D. Imparting Icephobicity with Substrate Flexibility. *Langmuir* **2017**, *33* (27), 6708–6718. <https://doi.org/10.1021/acs.langmuir.7b01412>.
- (172) Beemer, D. L.; Wang, W.; Kota, A. K. Durable Gels with Ultra-Low Adhesion to Ice. *J. Mater. Chem. A* **2016**, *4* (47), 18253–18258. <https://doi.org/10.1039/c6ta07262c>.
- (173) Golovin, K.; Dhyani, A.; Thouless, M. D.; Tuteja, A. Low-Interfacial Toughness Materials for Effective Large-Scale Deicing. *Science* (80-.). **2019**, *364* (6438), 371–375. <https://doi.org/10.1126/science.aav1266>.
- (174) Liu, J.; Zhu, C.; Liu, K.; Jiang, Y.; Song, Y.; Francisco, J. S.; Zeng, X. C.; Wang, J. Distinct Ice Patterns on Solid Surfaces with Various Wettabilities. *Proc. Natl. Acad. Sci. U. S. A.* **2017**, *114* (43), 11285–11290. <https://doi.org/10.1073/pnas.1712829114>.
- (175) Irajizad, P.; Al-Bayati, A.; Eslami, B.; Shafquat, T.; Nazari, M.; Jafari, P.; Kashyap, V.; Masoudi, A.; Araya, D.; Ghasemi, H. Stress-Localized Durable Icephobic Surfaces. *Mater. Horizons* **2019**, *6* (4), 758–766. <https://doi.org/10.1039/c8mh01291a>.
- (176) Sivakumar, G.; Jackson, J.; Ceylan, H.; Sundararajan, S. An Investigation on Ice Adhesion and Wear of Surfaces with Differential Stiffness. *Wear* **2021**, 203662. <https://doi.org/10.1016/j.wear.2021.203662>.
- (177) Dan, H. C.; He, L. H.; Zou, J. F.; Zhao, L. H.; Bai, S. Y. Laboratory Study on the Adhesive Properties of Ice to the Asphalt Pavement of Highway. *Cold*

- Reg. Sci. Technol.* **2014**, *104–105*, 7–13.
<https://doi.org/10.1016/j.coldregions.2014.04.002>.
- (178) Chen, H.; Wu, Y.; Xia, H.; Zhang, Z.; Yuan, T. Anti-Freezing Asphalt Concrete: Ice-Adhesion Performance. *J. Mater. Sci.* **2018**, *53* (7), 4781–4795.
<https://doi.org/10.1007/s10853-017-1866-z>.
- (179) Chen, H.; Wu, Y.; Xia, H.; Jing, B.; Zhang, Q. Review of Ice-Pavement Adhesion Study and Development of Hydrophobic Surface in Pavement Deicing. *Journal of Traffic and Transportation Engineering (English Ed.)*. Periodical Offices of Chang-an University June 1, 2018, pp 224–238.
<https://doi.org/10.1016/j.jtte.2018.03.002>.
- (180) Xia, H.; Zhao, X.; Wu, Y.; Yuan, T.; Song, L.; Yan, M.; Wang, F.; Chen, H. Preparation and Performance of Antifreeze Adhesive Materials for Asphalt Pavement. *Constr. Build. Mater.* **2020**, *258*.
<https://doi.org/10.1016/j.conbuildmat.2020.119554>.
- (181) Arabzadeh, A.; Ceylan, H.; Kim, S.; Gopalakrishnan, K.; Sassani, A.; Sundararajan, S.; Taylor, P. C. Superhydrophobic Coatings on Portland Cement Concrete Surfaces. *Constr. Build. Mater.* **2017**, *141* (March), 393–401.
<https://doi.org/10.1016/j.conbuildmat.2017.03.012>.
- (182) Penn, L. S.; Meyerson, A. *Ice-Pavement Bond Prevention: Fundamental Study*; Washington, DC, 1992.
- (183) MACOR® Machinable Glass Ceramic For Industrial Applications
<https://www.corning.com/worldwide/en/products/advanced->

- optics/product-materials/specialty-glass-and-glass-ceramics/glass-ceramics/macor.html (accessed Mar 15, 2021).
- (184) Gerber, J.; Lendenmann, T.; Eghlidi, H.; Schutzius, T. M.; Poulikakos, D. Wetting Transitions in Droplet Drying on Soft Materials. *Nat. Commun.* **2019**, *10* (1), 4776. <https://doi.org/10.1038/s41467-019-12093-w>.
- (185) Lee, J. B.; dos Santos, S.; Antonini, C. Water Touch-and-Bounce from a Soft Viscoelastic Substrate: Wetting, Dewetting, and Rebound on Bitumen. *Langmuir* **2016**, *32* (32), 8245–8254. <https://doi.org/10.1021/acs.langmuir.6b01796>.
- (186) Carré, A.; Gastel, J.-C.; Shanahan, M. E. R. Viscoelastic Effects in the Spreading of Liquids. *Nature* **1996**, *379* (6564), 432–434. <https://doi.org/10.1038/379432a0>.
- (187) Tarpoudi Baheri, F.; Schutzius, T. M.; Poulikakos, D.; Poulikakos, L. D. Bitumen Surface Microstructure Evolution in Subzero Environments. *J. Microsc.* **2020**, *279* (1), 3–15. <https://doi.org/10.1111/jmi.12890>.
- (188) Perez, A. P.; Wählin, J.; Klein-Paste, A. Effect of Surface Roughness and Chemistry on Ice Bonding to Asphalt Aggregates. *Cold Reg. Sci. Technol.* **2015**, *120*, 108–114. <https://doi.org/10.1016/j.coldregions.2015.08.015>.
- (189) Gan, X. Measurement and Characterization of Aggregate Surface Texture. **2017**, *100* (Icmeim), 421–426. <https://doi.org/10.2991/icmeim-17.2017.71>.
- (190) Schutzius, T. M.; Bayer, I. S.; Tiwari, M. K.; Megaridis, C. M. Novel

- Fluoropolymer Blends for the Fabrication of Sprayable Multifunctional Superhydrophobic Nanostructured Composites. *Ind. Eng. Chem. Res.* **2011**, *50* (19), 11117–11123. <https://doi.org/10.1021/ie200814r>.
- (191) Irajizad, P.; Nazifi, S.; Ghasemi, H. Icephobic Surfaces: Definition and Figures of Merit. *Adv. Colloid Interface Sci.* **2019**, *269*, 203–218. <https://doi.org/10.1016/j.cis.2019.04.005>.
- (192) Wang, C.; Fuller, T.; Zhang, W.; Wynne, K. J. Thickness Dependence of Ice Removal Stress for a Polydimethylsiloxane Nanocomposite: Sylgard 184. *Langmuir* **2014**, *30* (43), 12819–12826. <https://doi.org/10.1021/la5030444>.
- (193) Wang, C.; Gupta, M. C.; Yeong, Y. H.; Wynne, K. J. Factors Affecting the Adhesion of Ice to Polymer Substrates. *J. Appl. Polym. Sci.* **2018**, *135* (24), 45734. <https://doi.org/10.1002/app.45734>.
- (194) Kendall, K. The Adhesion and Surface Energy of Elastic Solids. *J. Phys. D. Appl. Phys.* **1971**, *4* (8), 320. <https://doi.org/10.1088/0022-3727/4/8/320>.
- (195) Mitridis, E.; Lambley, H.; Tröber, S.; Schutzius, T. M.; Poulidakos, D. Transparent Photothermal Metasurfaces Amplifying Superhydrophobicity by Absorbing Sunlight. *ACS Nano* **2020**, *14* (9), 11712–11721. <https://doi.org/10.1021/acsnano.0c04365>.
- (196) Shen, Y.; Tao, J.; Tao, H.; Chen, S.; Pan, L.; Wang, T. Superhydrophobic Ti6Al4V Surfaces with Regular Array Patterns for Anti-Icing Applications. *RSC Adv.* **2015**, *5* (41), 32813–32818. <https://doi.org/10.1039/c5ra01365h>.

-
- (197) Wang, N.; Tang, L.; Tong, W.; Xiong, D. Fabrication of Robust and Scalable Superhydrophobic Surfaces and Investigation of Their Anti-Icing Properties. *Mater. Des.* **2018**, *156*, 320–328. <https://doi.org/10.1016/j.matdes.2018.06.053>.
- (198) Ahammed, M.; Tighe, S. L. Early-Life, Long-Term, and Seasonal Variations in Skid Resistance in Flexible and Rigid Pavements. *Transp. Res. Rec.* **2009**, No. 2094, 112–120. <https://doi.org/10.3141/2094-12>.
- (199) Kogbara, R. B.; Masad, E. A.; Kassem, E.; Scarpas, A.; Anupam, K. A State-of-the-Art Review of Parameters Influencing Measurement and Modeling of Skid Resistance of Asphalt Pavements. *Constr. Build. Mater.* **2016**, *114*, 602–617. <https://doi.org/10.1016/j.conbuildmat.2016.04.002>.
- (200) Q8 Bitumens for the Construction Industry. *Kuwait Petroleum*. 2020, pp 7–8.
- (201) *Fundamentals of Heat and Mass Transfer*, 6 ed.; Frank P. Incropera, Ed.; John Wiley, 2007.
- (202) Guo, X.; Pethica, B. A.; Huang, J. S.; Prud'homme, R. K.; Adamson, D. H.; Fetters, L. J. Crystallization of Mixed Paraffin from Model Waxy Oils and the Influence of Micro-Crystalline Poly(Ethylene-Butene) Random Copolymers. *Energy and Fuels* **2004**, *18* (4), 930–937. <https://doi.org/10.1021/ef034098p>.
- (203) Kauzmann, W. The Nature of the Glassy State and the Behavior of Liquids at Low Temperatures. *Chem. Rev.* **1948**, *43* (2), 219–256. <https://doi.org/10.1021/cr60135a002>.

LIST OF PUBLICATIONS

Tarpoudi Baheri, F.; Schutzius, T. M.; Poulidakos, D.; Poulidakos, L. D. Bitumen Surface Microstructure Evolution in Subzero Environments. *Journal of Microscopy*, 279, 3–15 (2020). <https://doi.org/10.1111/jmi.12890>.

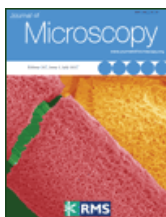
Rodríguez-Fernández, I.; **Tarpoudi Baheri, F.;** Cavalli, M. C.; Poulidakos, L. D.; Bueno, M. Microstructure Analysis and Mechanical Performance of Crumb Rubber Modified Asphalt Concrete Using the Dry Process. *Journal of Construction and Building Materials*, 259 (2020). <https://doi.org/10.1016/j.conbuildmat.2020.119662>.

Tarpoudi Baheri, F.; Rico Luengo, M.; Schutzius, T. M.; Poulidakos, D.; Poulidakos, L. D. The Effect of Additives on Water Vapor Condensation on Bituminous Surfaces. *Journal of Testing and Evaluation*, (2021). <https://doi.org/10.1520/JTE20210251>.

Tarpoudi Baheri, F.; Poulidakos, L. D.; Poulidakos, D.; Schutzius, T. M. Dropwise Condensation Freezing and Frosting on Bituminous Surfaces at Subzero Temperatures. *Journal of Construction and Building Materials*. 298, 123851 (2021). <https://doi.org/10.1016/j.conbuildmat.2021.123851>.

Ganter, D.; **Tarpoudi Baheri, F.;** Poulidakos, L. D.; Lupascu, D. C. Effect of Rejuvenators on the Microstructure of Aged Bitumen. *Manuscript in preparation*.

Tarpoudi Baheri, F.; Poulidakos, L. D.; Poulidakos, D.; Schutzius, T. M. Ice Adhesion Behavior of Heterogeneous Bituminous Surfaces. *Journal of Cold Regions Science and Technology*, 192, 103405 (2021). <https://doi.org/10.1016/j.coldregions.2021.103405>.



Thank you for your order!

Dear Mr. Farrokh Tarpoudi Baheri,

Thank you for placing your order through Copyright Clearance Center's RightsLink® service.

Order Summary

Licensee: Mr. Farrokh Tarpoudi Baheri
Order Date: Dec 3, 2021
Order Number: 5201170810447
Publication: Journal of Microscopy
Title: Bitumen surface microstructure evolution in subzero environments
Type of Use: Dissertation/Thesis
Order Total: 0.00 USD

View or print complete [details](#) of your order and the publisher's terms and conditions.

Sincerely,

Copyright Clearance Center

Tel: +1-855-239-3415 / +1-978-646-2777
customercare@copyright.com
<https://myaccount.copyright.com>



RightsLink®




Home


Help ▾


Email Support


Farrokh Tarpoudi Baheri ▾



Dropwise condensation freezing and frosting on bituminous surfaces at subzero temperatures

Author: F. Tarpoudi Baheri, L.D. Poulikakos, D. Poulikakos, T.M. Schutzius

Publication: Construction and Building Materials

Publisher: Elsevier

Date: 6 September 2021

© 2021 The Authors. Published by Elsevier Ltd.

Journal Author Rights

Please note that, as the author of this Elsevier article, you retain the right to include it in a thesis or dissertation, provided it is not published commercially. Permission is not required, but please ensure that you reference the journal as the original source. For more information on this and on your other retained rights, please visit: <https://www.elsevier.com/about/our-business/policies/copyright#Author-rights>

BACK

CLOSE WINDOW

© 2021 Copyright - All Rights Reserved | Copyright Clearance Center, Inc. | Privacy statement | Terms and Conditions

Comments? We would like to hear from you. E-mail us at customercare@copyright.com




Home


Help ▾


Email Support


Farrokh Tarpoudi Baheri ▾



Ice adhesion behavior of heterogeneous bituminous surfaces

Author: F. Tarpoudi Baheri, L.D. Poulikakos, D. Poulikakos, T.M. Schutzius

Publication: Cold Regions Science and Technology

Publisher: Elsevier

Date: December 2021

© 2021 The Authors. Published by Elsevier B.V.

Journal Author Rights

Please note that, as the author of this Elsevier article, you retain the right to include it in a thesis or dissertation, provided it is not published commercially. Permission is not required, but please ensure that you reference the journal as the original source. For more information on this and on your other retained rights, please visit: <https://www.elsevier.com/about/our-business/policies/copyright#Author-rights>

BACK

CLOSE WINDOW

© 2021 Copyright - All Rights Reserved | Copyright Clearance Center, Inc. | Privacy statement | Terms and Conditions

Comments? We would like to hear from you. E-mail us at customercare@copyright.com

SPRINGER NATURE

Thank you for your order!

Dear Mr. Farrokh Tarpoudi Baheri,

Thank you for placing your order through Copyright Clearance Center's RightsLink® service.

Order Summary

Licensee: Mr. Farrokh Tarpoudi Baheri
Order Date: Dec 3, 2021
Order Number: 5201201005413
Publication: Springer eBook
Title: The Effect of Additives on Water Vapor Condensation on Bituminous Surfaces
Type of Use: Thesis/Dissertation
Order Total: 0.00 USD

View or print complete [details](#) of your order and the publisher's terms and conditions.

Sincerely,

Copyright Clearance Center

Tel: +1-855-239-3415 / +1-978-646-2777
customercare@copyright.com
<https://myaccount.copyright.com>



RightsLink®